INTERNATIONAL JOURNAL OF AVIATION SCIENCE AND TECHNOLOGY
IJAST
www.ijast.org

International Journal of Aviation Science and Technology

Volume 3, Issue 2, December 2022

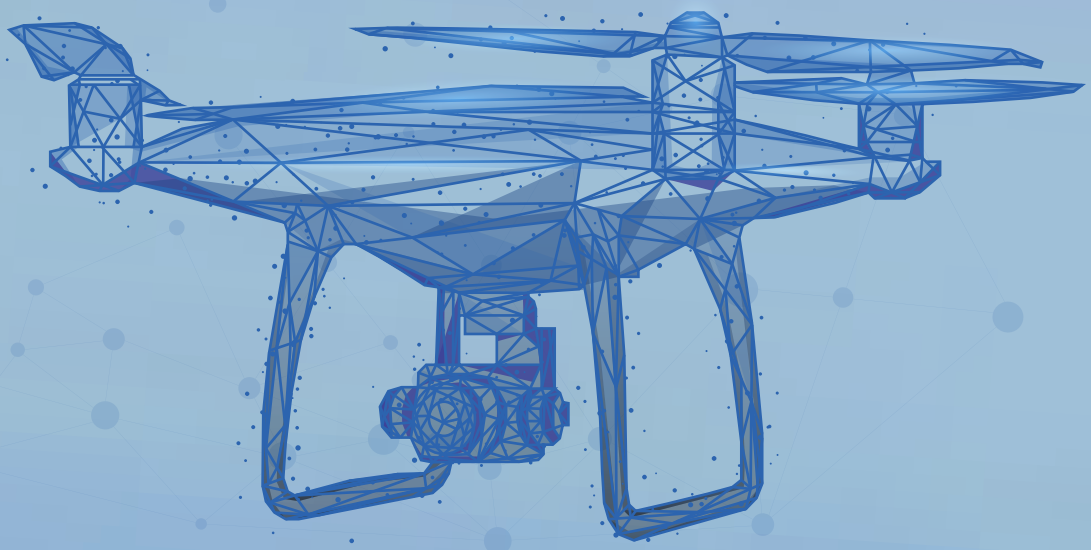

e-ISSN: 2687-525X
INTERNATIONAL SUSTAINABLE AVIATION AND ENERGY RESEARCH SOCIETY
SARES
www.sares.org

International Journal of Aviation Science and Technology

Publisher : SARES
International Sustainable Aviation and Energy Research Society
Licence holder : Prof. Dr. T. Hikmet Karakoç (President, SARES)
Address : Anadolu University TGBD TechnoPark Region No:210
26470 Eskisehir, Turkiye

e-ISSN : 2687-525X
DOI : 10.23890/IJAST
Submission : www.ijast.org
e-mail : ijast@sares.org
Copyright : SARES Society

IJAST is published with the contribution of "Research and Application Center of Civil Aviation, Eskisehir Technical University"

Index

	Title	Start Page	Finish Page
6	An investigation of the Control Quality of the Automatic Control System for Fixed-wing UAVs During Landing Process Trung Vuong Anh, Hong Son Tran, Dinh-dung Nguyen, Truong-thanh Nguyen, Trong-son Phan, Hong Tien Nguyen	61	69
7	Numerical Analysis of Variable Morphing Wing for Improved Aerodynamic Performance of a Predator MQ-1B Erdogan Kaygan	70	80
8	A Comprehensive Study On The Effects Of Noise Abatement Departure Procedures On Noise Contours Around Tan Son Nhat International Airport La Tuan Kiet, Tien Anh Tran	81	95
9	Aircraft Noise Compatibility of the Airports with Progress of Noise Reduction at Source Oleksandr Zaporozhets, Kateryna Kazhan, Kateryna Synylo, Sergii Karpenko	96	111
10	Improving the Efficiency of Angular Velocity Sensors on Aircraft Trung Vuong Anh, Hong Son Tran, Dinh-dung Nguyen, Truong-thanh Nguyen, Omar Alharasees, Utku Kale	112	123

International Journal of Aviation Science and Technology

Research Article

An investigation of the Control Quality of the Automatic Control System for Fixed-wing UAVs During Landing Process

Trung Vuong Anh[1], Hong Son Tran[2], Dinh-dung Nguyen[3]*, Truong-thanh Nguyen[4], Trong-son Phan[5], Hong Tien Nguyen[6]

[1] *Faculty of Aviation Technical, Air defense-Air Force Academy, 100000 Hanoi, Vietnam*
vuonganhtrung@gmail.com - 0000-0002-4602-3975

[2] *Faculty of Control Engineering, Le Quy Don Technical University, 100000 Hanoi, Vietnam,*
tranhongson@lqdtu.edu.vn - 0000-0002-7956-2377

[3] *Department. of Aircraft System Design, Faculty of Aerospace Engineering, Le Quy Don Technical University, 100000 Hanoi, Vietnam,*
dungnd@lqdtu.edu.vn - 0000-0002-8966-051X

[4] *Department of Military Science, Air Force Officer's College, 650000 Khanh Hoa, Vietnam,*
truongthanhna74@gmail.com - 0000-0001-7992-2291

[5] *Department of Aircraft-Engines, Air Force Officer's College, 650000 Khanh Hoa, Vietnam,*
trongson21@gmail.com - 0000-0003-3508-7583

[6] *Faculty of Aviation Technical, Air defense-Air Force Academy, 100000 Hanoi, Vietnam,*
smallcat24829@gmail.com - 0000-0003-2037-4520

Abstract

This study presents an investigation and evaluation of the control quality of the automatic control system for UAVs in the vertical plane under windy conditions. For the operational stages of UAVs in general, the landing stage is one of the high-probability stages that pose a threat to flight safety, especially at the time of landing. Therefore, to evaluate the control quality of the system, the authors investigated the parameters during UAV landing. The automatic control system uses a PID controller with optimal parameters selected by the Signal Constraint tool in Matlab Simulink. The predetermined wind model was used to verify at the most extreme times. The programs proposed in the paper are simulated on Matlab Simulink software.

Keywords

UAV
PID controller
Automatic control system
Landing approach

Time Scale of Article

Received 23 July 2022
Revised until 27 September 2022
Accepted 11 October 2022
Online date 29 December 2022

1. Introduction

Today, unmanned aerial vehicles (UAVs) have increased popularity in the market, ranging from pure recreation to scientific research, making them broader and more comprehensive applicability areas. Therefore, control algorithms must be improved to increase flight safety and reliability.

While during flight conditions, the UAV is required to perform precise maneuvers and agile, during the landing process, the UAV should closely abide by a reference trajectory to obtain an efficient landing. A complete operational UAV consists of three stages: launching, mission flight, and recycling. The launching and mission flight stages are relatively mature thanks to advanced technologies, whereas recycling is still challenging for researchers (Tan et al., 2019). Besides, the autonomous control system for the landing process is a complex problem that needs more studies and research regarding both theory and implementations (Kim et al., 2016).

*: Corresponding Author Dinh-dung Nguyen, ddnguyen@vrht.bme.hu
DOI: 10.23890/IJAST.vm03is02.0201

Several methods have been developed and designed for automatic landing systems of UAVs, such as ground-based system (Kong et al., 2014), (Yang et al., 2016), fuzzy logic (Brukarczyk et al., 2021), hierarchical control structure (Zhang and Wang, 2017), neuro-adaptive (Ambati and Padhi, 2017), backstepping technique (Lungu, 2019), nonlinear model predictive control (Mathisen et al., 2020), combination for low-level control architecture (Manjarrez, Davila and Lozano, 2018).

In the literature, various papers give interesting approaches to landing trajectory optimization, including fuzzy logic (Magnus, 2016), deep reinforcement learning (Bayerlein, Kerret and Gesbert, 2018), solving the system of differential motion of UAV to determine the desired landing orbit (Rohacs and Dung, 2019), artificial neural network (Moriarty, Sheehy and Doody, 2017). Yi Feng et al. developed a predictive model controller for UAVs in the landing process under varied turbulence, which guarantees a safe and accurate flight (Feng et al., 2018). In contrast, Sanches-Lopez et al. combined the Kalman filter with a vision for improving an autonomous landing algorithm (Sanchez-Lopez et al., 2013). T. Yang et Al. presented an infrared camera array guidance system to track and give a UAV's real-time position and speed during the landing process (Yang et al., 2016). Such a system used two infrared cameras and a laser lamp: a laser lamp was fixed on the nose to calculate the position. Two infrared cameras were located on the two sides of the runway to capture flying UAV images. Based on this information, the real-time position and speed of the UAV were calculated and sent to the UAV control center.

The landing control issue can be divided into two categories: control and guidance. At the low-level, attitude control is a precondition for the landing process, which can apply sliding mode control (Venkateswara Rao and Go, 2014) and backstepping techniques (Lungu, 2019). At the middle level, proportion integration differentiation (PID)-based controllers are designed to determine the desired attitude. At the same time, a proportional guidance law is designed for height tracking at the top level. Besides, guidance laws are designed based on attitude control, based on the linear model (Wang and Wen, 2010), nonlinear energy method (Jones, Akmeliawati and Tan, 2010), fuzzy logic modules (Brukarczyk et al., 2021), a linear quadratic tracker with integral (Koo, Kim and Suk, 2015), and nonlinear model predictive control (Mathisen et al., 2020). However, most of the abovementioned approaches require exact knowledge of system parameters and validation of the performance using numerical simulations.

In recent years, the research and manufacture of UAVs have also made significant progress. An onboard edge motion controller was synthesized for unmanned aerial vehicles (UAV) under some simple conditions (Quang, 2008), (Dang et al., 2016). For the problem of trajectory and tracking, P. Anh et al. proposed tracking algorithms for UAVs, such as a virtual line of sight algorithm, based on sliding mode (Thi, Nguyen and Phan, 2018). That study indicated that the navigation algorithm based on the sliding mode, the system is stable quickly and can be proposed to be used for all different modes. Taking into account the control signal limitation, Toan et al. presented a method to optimize the landing trajectory for autonomous fixed-wing UAVs by applying the Pontryagin maximal principle (Ngo et al., 2019). An investigation of the PI controller for autonomous fixed-wing UAV in the vertical plane with no wind conditions was presented (Ngo et al., 2020). Considering wind disturbance, Vu et al. developed a gradient speed adaptive controller with an explicit reference model (Dang et al., 2016). Thu et al. proposed a method to determine the parameters of the UAV to serve the landing process, including pitch angle, inclination angle, direction angle, distance, angle deviation, and the height of the UAV (Do, Do and Ngo, 2016). These parameters are used to control the UAV tracking the landing trajectory safely. However, these works are still relatively modest in terms of the quality and size of the problem. Conventional studies only deal with a relatively minor aspect with given hypothetical conditions and do not come close to the actual flying conditions of the UAV. To overcome this issue, an improvement of the automatic control system for fixed-wing UAVs was presented in the previous works (Tran et al., 2022). Although this improvement was sastified by the numerical simulation results, some limitations of that study still existed, including the UAV speed was set to be constant during landing process; the UAV motion was not considered in the landing approach; the UAV's altitude was slightly higher than the actual operation of the UAV-70.

Therefore, this study investigates the controller quality for fixed-wing UAVs under windy disturbances, making the research results more closely related to the actual conditions.

2. Methods

In this study, the motion of UAVs will be taken into the synthesizing the control rule for the autonomous control system. The following equation system describes the kinematic model of the UAV (Ngo et al., 2020):

Where, V_g– ground speed; V_a– air speed; m – mass of UAV; α - attack angle; θ - flight path angle; x – distance of the flight; y – heigh of the flight; C_D- drag coefficient; C_L- lift coefficient; ρ- air density.

$$
\begin{aligned}
&m\left(\frac{dV_g}{dt}\right) = T\cos\alpha - C_D.\alpha\frac{\rho.V_a^2}{2}.S - G\sin\theta \\
&mV_g\frac{d\theta}{dt} = T\sin\alpha + \left(C_L.\alpha + C_y^{\delta_e}.\delta_e\right).\frac{\rho.V_a^2}{2}.S - G\cos\theta \\
&J_z\left(\frac{d\omega_z}{dt}\right) = \left(m_z^{\delta_e}.\delta_e + m_z^{\alpha}\alpha\right).\frac{\rho.V_a^2}{2}.S.b_a \\
&\frac{dx_o}{dt} = V_g\cos\theta \\
&\frac{dy_o}{dt} = V_g\sin\theta \\
&\frac{d\vartheta}{dt} = \omega_z
\end{aligned} \tag{1}
$$

The motion of UAVs is considered in the landing process that measures from the beginning to a grounding point. After practicing with UAV-70 in the natural environment, we recommend that the length of the landing trajectory is around 1000m, and the heigh of the beginning point is around 60m. The grounding point is based on the UAV's structural properties, safety, and flight accuracy. Therefore, in this study, we assume that (i) the grounding point is 20m from the head of the runway, and (ii) the reference trajectory is a parabolic sharp. Figures 1 and 2 describe the UAV's reference trajectory and flight path angle during the landing process.

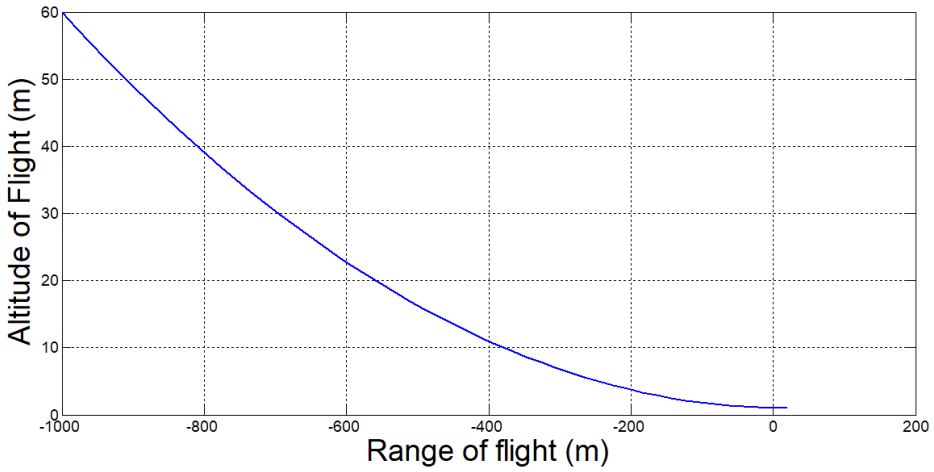

Fig. 1. UAV landing reference trajectory

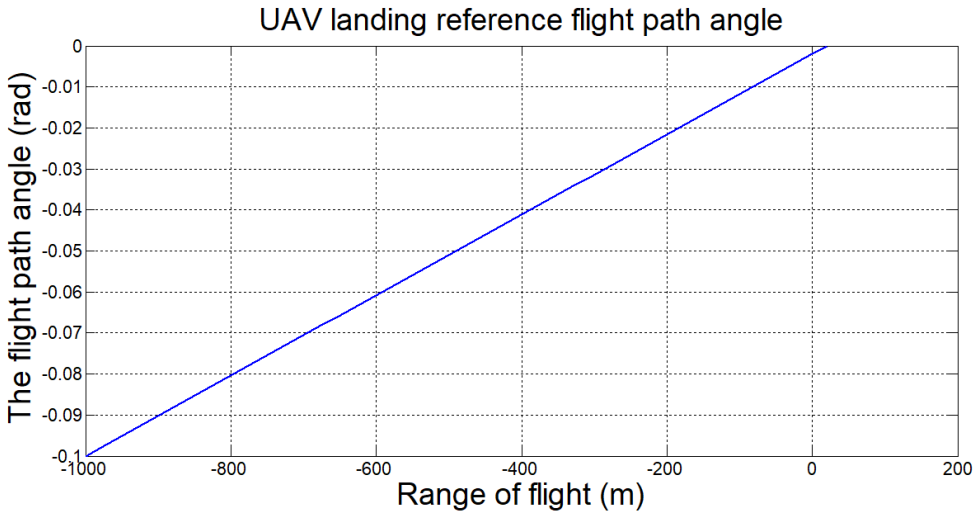

Fig. 2. UAV landing reference flight path angle

The following equation system is calculated based on the geometrical parameters, illustrating the reference trajectory of the UAV.

$$
\begin{cases}
h = \frac{59}{1040400}x^2 - \frac{59}{26010}x + \frac{2660}{2610} \\
\theta = \frac{1}{10200}x - \frac{1}{510}
\end{cases} \tag{2}
$$

The author proposes using the PID controller, a powerful method in this study. The parameters of the autonomous control system (K_p, K_i, K_d) were optimized by the tool "Signal Constraint" in the "Simulink Design Optimization" in the Matlab software.

Whereas, if both the heigh error and flight path angle are reached zero, the PID controller will be well done. Therefore, we propose the control law in the vertical plane, described in equation (3), by which the UAV will follow the reference trajectory.

$$\delta_e = K_p\Delta h + K_d\Delta\theta + K_i\int_0^t \Delta h dt + \delta_{e\_bb} \tag{3}$$

Where, $\Delta h = h_{cur} - h_{ref}$: heigh error (m)

h_{cur} : Current heigh (m);

h_{ref} : Reference heigh (m);
$\Delta\theta = \theta_{cur} - \theta_{ref}$: Flight path angle error (rad);
θ_{cur} : Current flight path angle (rad);
θ_{ref} : Reference flight path angle (rad);
K_p : Proportional coefficient (rad/m);
K_d : Derivative coefficient (-);
K_i : Integral coefficient (rad/m);
δ_{e_bb} : Starting elevator deflection angle (rad);

We synthesize a closed loop based on the rule (3) for vertical channel, usisng PID controller during landing process.

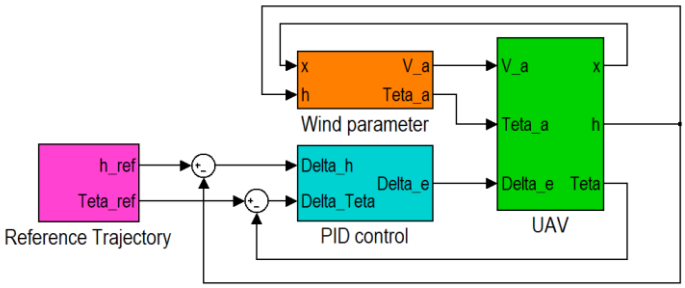

Fig. 3. The UAV control system in the vertical plane.

When the UAV is grounded, the following conditions must be met:

- Range of flight error from the head of the runway $|\Delta x| \leq 30m$;
- Altitude error at the touching point $0m \leq |\Delta h| \leq 0{,}3m$;
- Touching speed $V_{hc} \geq V_{min}$ (where $V_{min} = \sqrt{\frac{2G}{C_{yHC}\rho S}}$)
- Vertical speed $|V_y| \leq 1m/s$;
- Pitch angle at the grounding point $0 \leq \vartheta \leq 12°$;

3. Simulation Results and Discussion

The First Case

We used parameter of UAV-70 (Ngo *et al.*, 2020) in this study. UAV motion in case tailwind maximum parameters: $L = 14\ (m);\ W_0 = 6\ \left(\frac{m}{s}\right)$;

Initial state of UAV: $\begin{cases} h_0 = 60\ (m) \\ x_0 = -1000\ (m) \\ v_g = 40\ (m/s) \end{cases}$;

Final state of UAV: $\begin{cases} h_t = 1\ (m) \\ x_t = 20\ (m) \\ v_y = 0\ (m/s) \\ v_g = 32(m/s) \end{cases}$;

PID parameters: $\begin{cases} K_p = 0{,}0111 \\ K_d = -0{,}2514 \\ K_i = 0.0029 \end{cases}$

The simulation results are shown in Figures 4-5

The parameters of the UAV at the time of grounding point are given in table 1 as follows.

The Second Case

Simulation results for the case compare four different conditions at touching down.

To further test the effectiveness of the PID controller, the authors use four extreme wind models at the time of touching down of the UAV. It is assumed that the mode of the UAV motion velocity vector, $V_a(t)$, is known constant during the UAV landing approach. For the UAV landing time, the predicted position of the UAV is $P(x_t, h_t)$. The numerical simulation results are shown in figures 6-12.

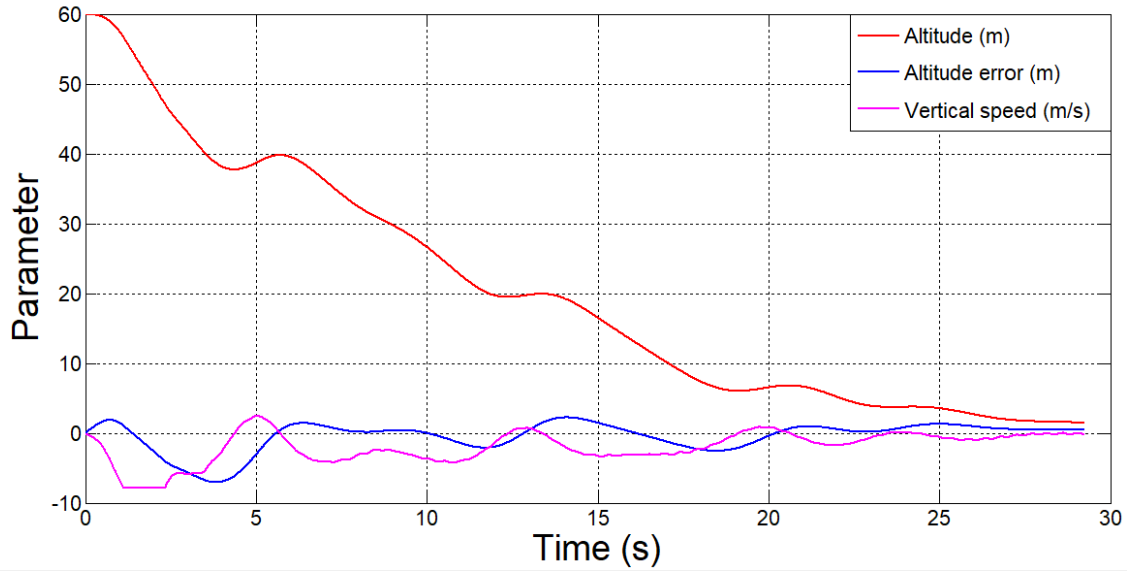

Fig. 4. The UAV's parameter-1

Table 1. Parameters of UAV at the time of grounding point.

Section No	Parameter	Value	Permissible value	Value from (Ngo *et al.*, 2020)
01	Altitude error	$\Delta h = 0.09$ m	$\lvert\Delta h\rvert \leq 0.3$	$\Delta h = 0.12$m
02	Range of flight error	$\Delta x = 0.2$ m	$\lvert\Delta x\rvert \leq 30$	$\Delta x = 0.3$m
03	Vertical speed	$\lvert V_y\rvert = 0.3$ m/s	$\lvert V_y\rvert \leq 1$	
04	Pitch angle	$\vartheta = 7^o$	$0 \leq \vartheta \leq 12^o$	$\vartheta = 10^o$

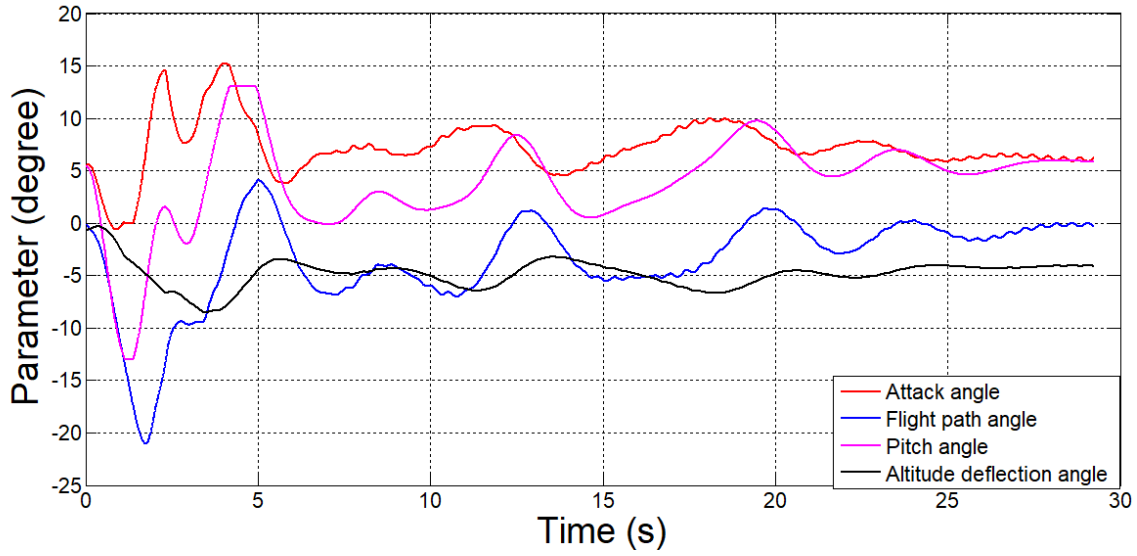

Fig. 5. The UAV's parameter-2

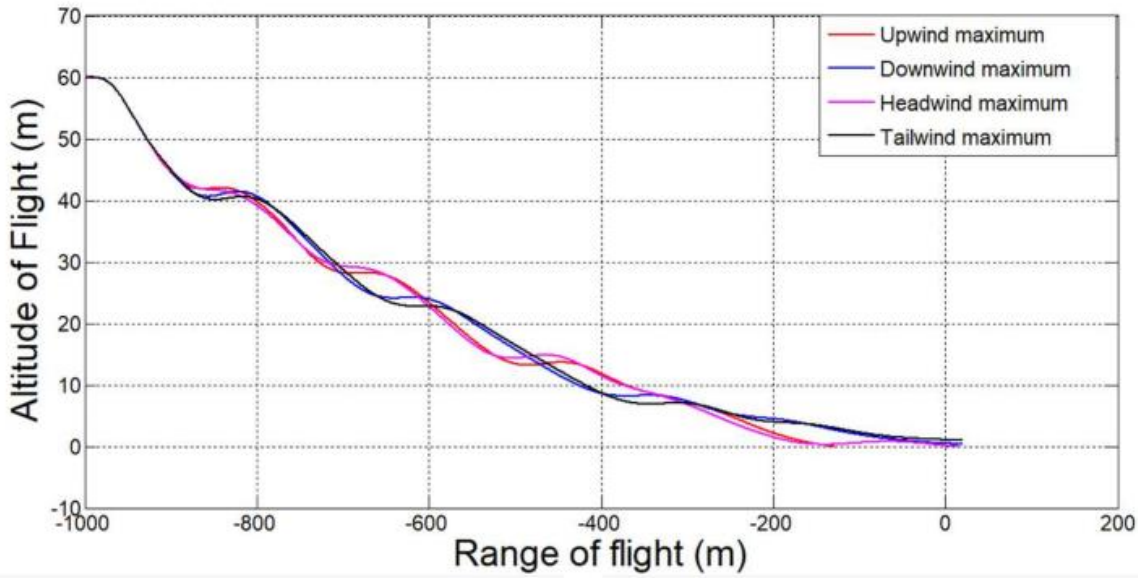

Fig. 6. The UAV's trajectory

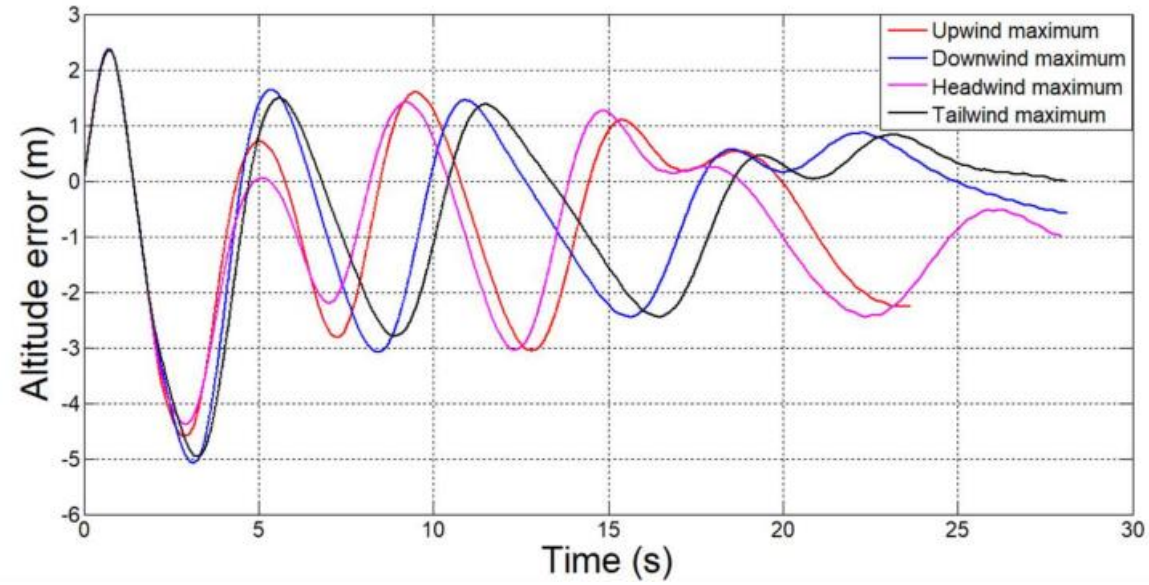

Fig. 7. The altitude error

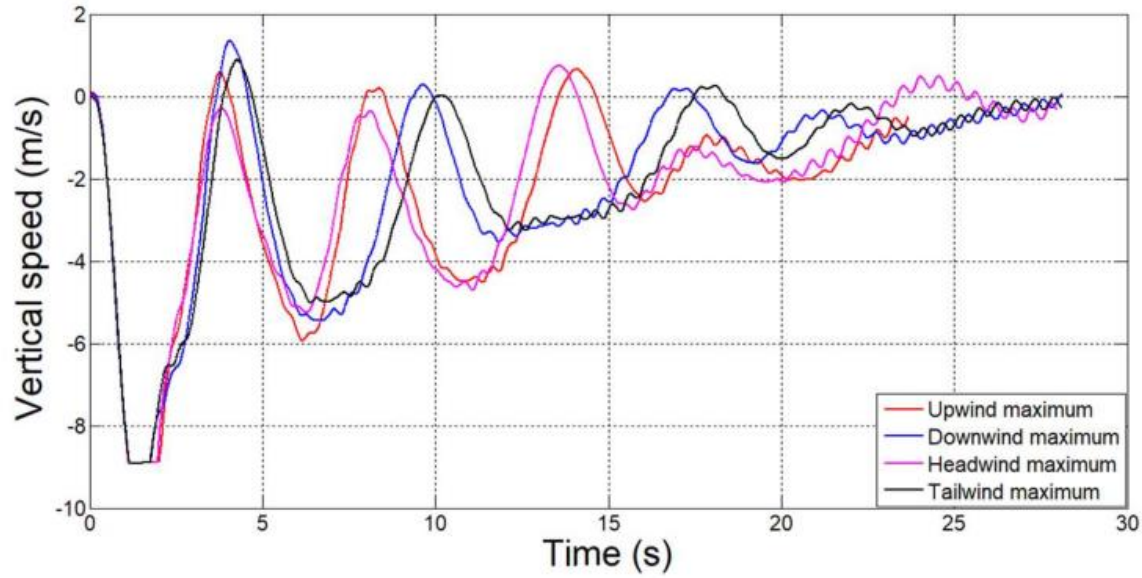

Fig. 8. The vertical speed

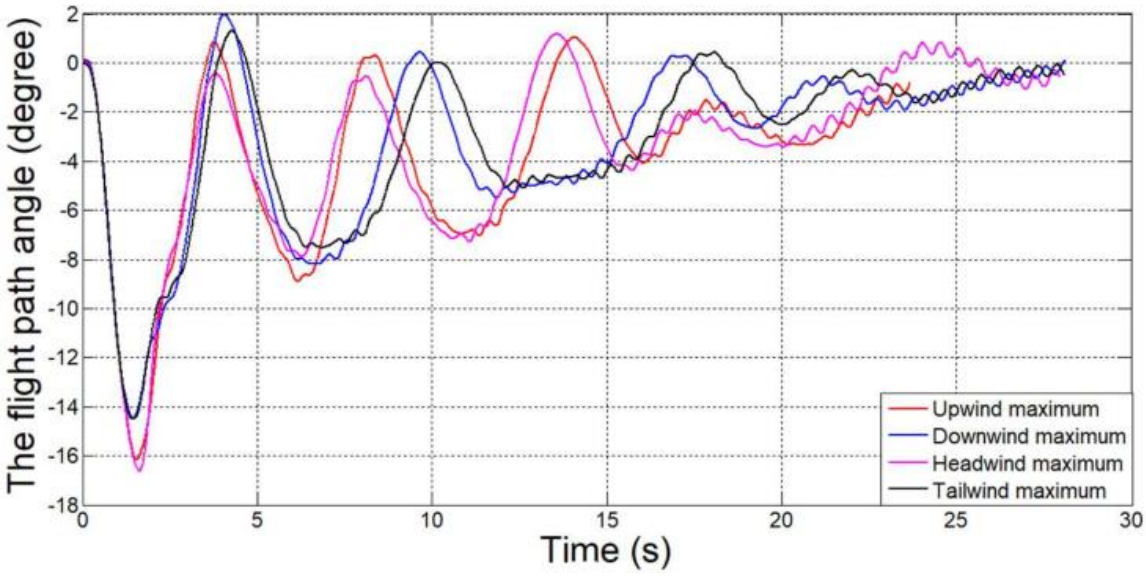

Fig. 9. The flight path angle

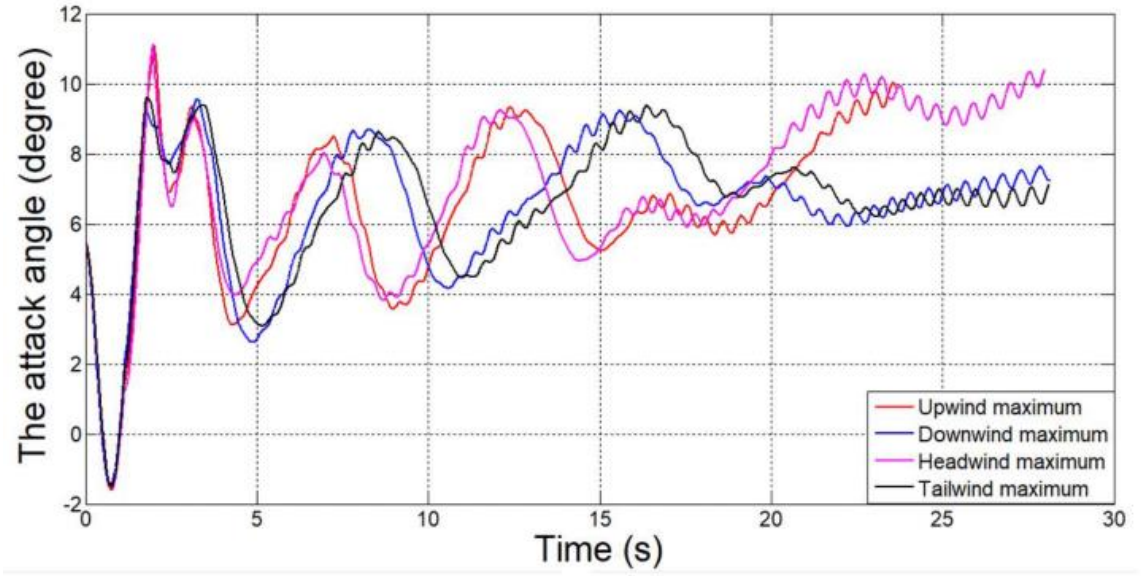

Fig. 10. The attack angle

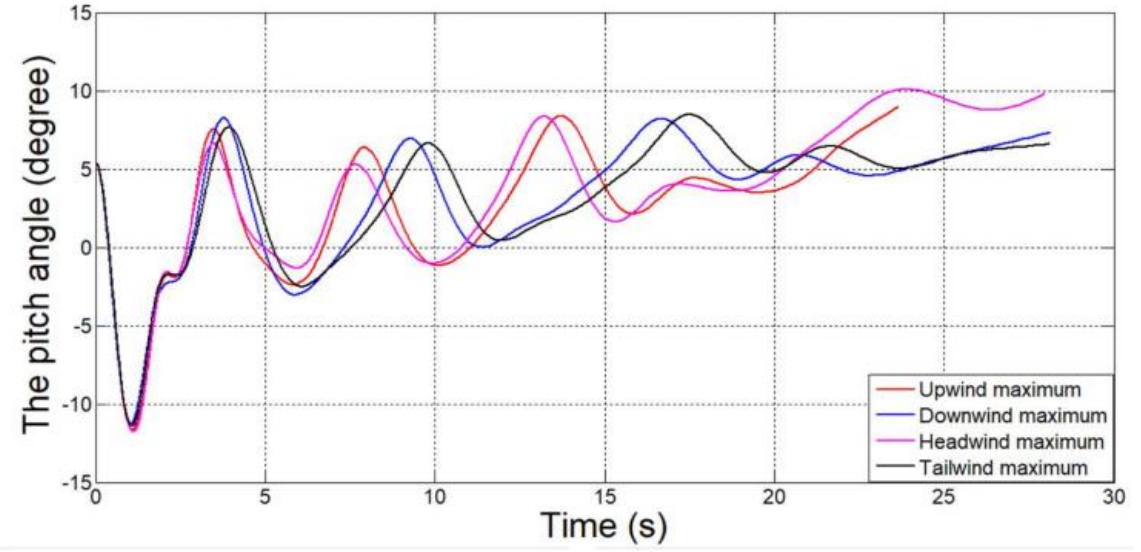

Fig. 11. The pitch angle

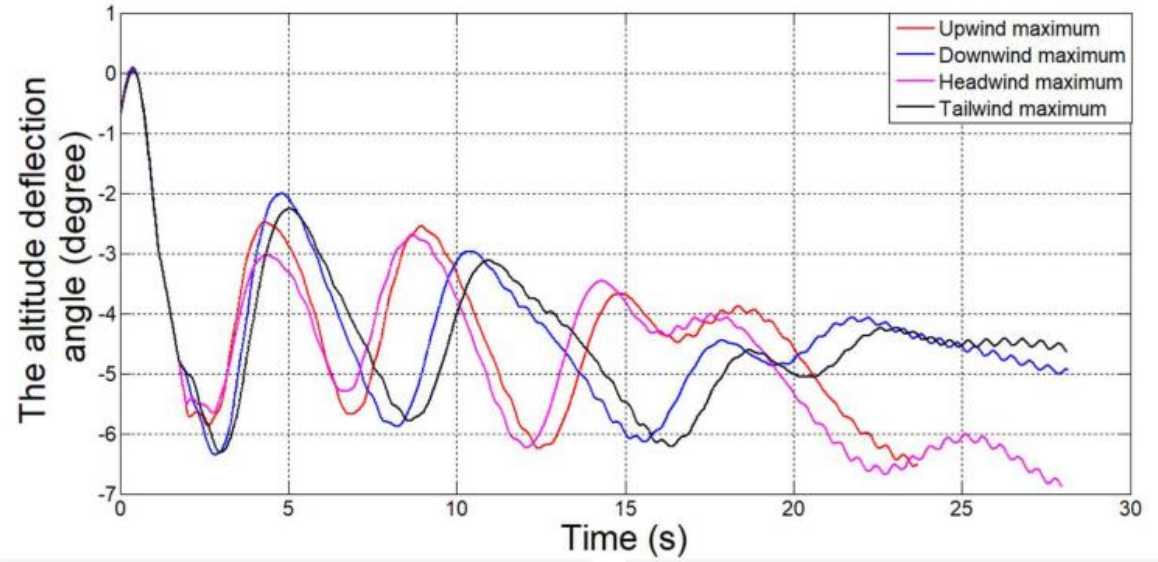

Fig. 12. The altitude deflection angle

4. Conclusions

In this study, the authors investigate and evaluate the control quality of the automatic control system for fixed-wing UAVs in the vertical plane with wind conditions. The automated control system used a PID controller with optimal parameters with a predetermined wind model. The comparison of the proposed approach with the system-used PI controller and previous work also are given in this paper, indicating that the quality of the proposed PID controller is much more effective than the results of the PI controller with wind conditions in the vertical plane. Although some parts of the previous study have been overcome, the proposed PID controller's errors during the landing stage still exist. While this paper investigated the automatic landing system of UAVs in the vertical plane, future research will expand this work to complete the problem of UAV landing in space, such as investigating this system within wind disturbance.

Abbreviations

UAV : Unmanned Aerial Vehicle
PID : Proportion Integral Derivation
PI : Proportion Integral

References

Ambati, P.R. and Padhi, R. (2017) 'Robust auto-landing of fixed-wing UAVs using neuro-adaptive design', *Control Engineering Practice*, 60, pp. 218–232. doi:10.1016/j.conengprac.2016.03.017.

Bayerlein, H., Kerret, P. De and Gesbert, D. (2018) 'Trajectory Optimization for Autonomous Flying Base Station via Reinforcement Learning', in *2018 IEEE 19th International Workshop on Signal Processing Advances in Wireless Communications (SPAWC)*, pp. 1–5. doi:10.1109/SPAWC.2018.8445768.

Brukarczyk, B. *et al.* (2021) 'Fixed Wing Aircraft Automatic Landing with the Use of a Dedicated Ground Sign System', *Aerospace*, 8(6). doi:10.3390/aerospace8060167.

Dang, C.V. *et al.* (2016) 'Application of adaptive controller improves flight safety for small UAVs in wind turbulence conditions', *Journal of Military Science and Technology* [Preprint].

Do, V.T., Do, Q.T. and Ngo, V.T. (2016) 'Identify drone landing data on image processing database', *Journal of Science and Engineering* [Preprint].

Feng, Y. *et al.* (2018) 'Autonomous Landing of a UAV on a Moving Platform Using Model Predictive Control', *Drones*, 2(4). doi:10.3390/drones2040034.

Jones, L.J.N., Akmeliawati, R. and Tan, C.P. (2010) 'Automatic aircraft landing control using Nonlinear Energy Method', in *2010 IEEE International Conference on Control Applications*, pp. 2142–2147. doi:10.1109/CCA.2010.5611294.

Kim, N. V. *et al.* (2016) 'Selecting a flight path of an UAV to the ship in preparation of deck landing', *Indian Journal of Science and Technology*, 9(46). doi:10.17485/ijst/2016/v9i46/107504.

Kong, W. *et al.* (2014) 'A ground-based optical system for autonomous landing of a fixed wing UAV', in *2014 IEEE/RSJ International Conference on Intelligent Robots and Systems*, pp. 4797–4804. doi:10.1109/IROS.2014.6943244.

Koo, S., Kim, S. and Suk, J. (2015) 'Model Predictive Control for UAV Automatic Landing on Moving Carrier Deck with Heave Motion', *IFAC-PapersOnLine*, 48(5), pp. 59–64. doi:10.1016/j.ifacol.2015.06.464.

Lungu, M. (2019) 'Auto-landing of fixed wing unmanned aerial vehicles using the backstepping control', *ISA Transactions*, 95, pp. 194–210. doi:10.1016/j.isatra.2019.05.019.

Magnus, V. (2016) *Automatic Takeoff and Landing of Unmanned Fixed Wing Aircrafts : A Systems Engineering Approach*. Available at: http://liu.diva-portal.org/smash/get/diva2:1055556/FULLTEXT01.pd.

Manjarrez, H., Davila, J. and Lozano, R. (2018) 'Low Level Control Architecture for Automatic Takeoff and Landing of Fixed Wing UAV', in *2018 Annual American Control Conference (ACC)*, pp. 6737–6742. doi:10.23919/ACC.2018.8430789.

Mathisen, S. *et al.* (2020) 'Precision Deep-Stall Landing of Fixed-Wing UAVs Using Nonlinear Model Predictive Control', *Journal of Intelligent & Robotic Systems*, 101(1), p. 24. doi:10.1007/s10846-020-01264-3.

Moriarty, P., Sheehy, R. and Doody, P. (2017) 'Neural networks to aid the autonomous landing of a UAV on a ship', in *2017 28th Irish Signals and Systems Conference (ISSC)*, pp. 1–4. doi:10.1109/ISSC.2017.7983613.

Ngo, V.T. *et al.* (2019) 'Optimizing the landing trajectory of the UAV in short runway conditions', *Journal of Military Science and Technology* [Preprint].

Ngo, V.T. *et al.* (2020) 'Using PI controller to track landing trajectory for small UAV', *Journal of Military Science and Technology* [Preprint].

Quang, V.H. (2008) *Synthesis of the on-board edge motion control system for* UAV.

Rohacs, J. and Dung, N.D. (2019) 'Robust planning the landing process of unmanned aerial vehicles', *International Journal of Sustainable Aviation*, 5(1), p. 1. doi:10.1504/ijsa.2019.10021483.

Sanchez-Lopez, J.L. *et al.* (2013) 'Toward visual autonomous ship board landing of a VTOL UAV', in *2013 International Conference on Unmanned Aircraft Systems (ICUAS)*, pp. 779–788. doi:10.1109/ICUAS.2013.6564760.

Tan, L. *et al.* (2019) 'Research on Optimal Landing Trajectory Planning Method between an UAV and a Moving Vessel', *Applied Sciences*, 9(18). doi:10.3390/app9183708.

Thi, P.A.P., Nguyen, V. and Phan, T.L. (2018) 'Path following algorithm for uav', *Journal of Military Science and Technology* [Preprint].

Tran, H.S. *et al.* (2022) 'Development of Automatic Landing Control Algorithm for Fixed-Wing UAVs in Longitudinal Channel in Windy Conditions', in Tien Khiem, N., Van Lien, T., and Xuan Hung, N. (eds) *Modern Mechanics and Applications. Lecture Notes in Mechanical Engineering*. Singapore: Springer Singapore, pp. 945–958. doi:10.1007/978-981-16-3239-6_74.

Venkateswara Rao, D.M.K.K. and Go, T.H. (2014) 'Automatic landing system design using sliding mode control', *Aerospace Science and Technology*, 32(1), pp. 180–187. doi:10.1016/j.ast.2013.10.001.

Wang, L.-C. and Wen, C.-Y. (2010) 'Adaptive trajectory tracking for UAV guidance with bayesian filtering', in *2010 5th IEEE Conference on Industrial Electronics and Applications*, pp. 2311–2316. doi:10.1109/ICIEA.2010.5515553.

Yang, T. *et al.* (2016) 'A Ground-Based Near Infrared Camera Array System for UAV Auto-Landing in GPS-Denied Environment', *Sensors*, 16(9). doi:10.3390/s16091393.

Zhang, D. and Wang, X. (2017) 'Autonomous Landing Control of Fixed-wing UAVs: from Theory to Field Experiment', *Journal of Intelligent & Robotic Systems*, 88(2), pp. 619–634. doi:10.1007/s10846-017-0512-y.

International Journal of Aviation Science and Technology

Research Article

Numerical Analysis of Variable Morphing Wing for Improved Aerodynamic Performance of a Predator MQ-1B

Erdogan Kaygan

[1] *Girne American University, Department of Aviation Management and Pilotage, Cyprus, Turkey*

erdogankaygan@gau.edu.tr - 0000-0003-3319-3657

Abstract

In this paper, aerodynamic performance benefits of morphing unmanned aerial vehicle's wing concepts are investigated. A Predator MQ-1B with variable wing structure was utilized for this study. The concept consists of variable twist (-10°< θ <10°, in steps of ±2.5°) and wing sweep (0°< θ <30°, in steps of +10°) to illustrate morphing wing's performance benefits. All computations were performed with Athena Vortex Lattice modelling with varying degrees of twist and sweep angle considered. The results obtained from this work show that if morphing wings adapted to the Predator MQ-1B, it will provide significant performance benefits and also offer a great opportunity to reduce fuel consumption.

Keywords

Aerodynamics
Morphing
Predator
Sweep
Twist

Time Scale of Article

Received 30 August 2022
Revised until 19 September 2022
Accepted 23 September 2022
Online date 29 December 2022

1. Introduction

Unmanned aerial vehicles (UAVs) are the most dynamic field of Aerospace technology which is an emerging technology with a stupendous potential to revolutionize combat and to enable new civilian applications (Austin, 2010; Gundlach, 2012). Although they have been so common in recent years, they have actually been in use for several years. Remotely piloted aircraft first appeared during world war I, but the early efforts were stymied by the primitive guidance technology available. NASA(Kudva, J. et al., 1997), DARPA (Kudva, 2004)and also most of researchers(Abdulrahim et al., 2005; Bourdin, Gatto and Friswell, 2006; Gomez and Garcia, 2011; Prisacariu, Boscoianu and Cîrciu, 2013; Kaygan and Gatto, 2016; Prisacariu, Boşcoianu and Cîrciu, 2017) have been conducted performance studies regarding unpiloted morphing aerial vehicles. (Abdulrahim et al., 2005) designed twist morphing wings and flight tests demonstrate the actuation causes sufficient deformation of the wing to result in significant control authority. Similarly, (Bourdin, Gatto and Friswell, 2006; Gomez and Garcia, 2011; Prisacariu, Boscoianu and Cîrciu, 2013; Kaygan and Gatto, 2016) developed twist morphing wings for roll control and also for performance benefits of an aircraft. According to all studies, approximately 20% performance benefits achieved and similar to the fixed wing – aileron roll control was achieved using twist wing configurations. Morphing aircraft is a unique design concept that has been proposed as a solution to the performance constraints of conventional aircraft. The motivation behind wing morphing comes from the observation of the birds where they alter their wings' configuration to achieve suitable aerodynamic profile for several flight regimes. Though this concept seems new-fangled, applications were developed several years ago. Wing-warping techniques were utilized by the Wright Brothers to control the first powered, heavier-than-air aircraft through suspended cables (Culick, 2003). However, in

*: Corresponding Author Erdogan Kaygan, erdogankaygan@gau.edu.tr
DOI: 10.23890/IJAST.vm03is02.0202

today's aviation world, this technique is no longer available and has been replaced by traditional control surfaces such as aileron for roll, elevator for pitch, and rudder for yaw control (McRuer and Graham, 2004). Although these surfaces widely accepted as a conventional control surface, it is a fact that they increase drag dramatically due to generation of flow separation over the wing profile. Accordingly, this is the reason why aerospace industry re-calling morphing application to meet the ever-increasing demands for more efficient, robust, and cost-effective designs. Furthermore, most UAVs have mission proles that require them to cycle between loitering, cruising, climb and fast descents. Comparing Morphing UAV with commercial airlines (See Fig. 1), traditional aircrafts have difficulties to adapt greatly different dynamic flight regimes (Galantai, 2010). The current and past researches summarized by several researchers (Jha and Kudva, 2004; Weisshaar and Challenge, 2006; Min, Kien and Richard, 2010; Barbarino et al., 2011). Adaptive wing concepts are advantageous because aerial vehicle operate in a wide range of flight conditions (e.g., take-off, climb, cruise with various payloads, descent, and landing), each of which have conflicting requirements and performance metrics. For example, in order to have low fuel consumed cruising, an aircraft wing should be as small as possible with sensible camber whilst, when landing, a large area and high camber are desirable for a low enough speed. This need has been addressed with traditional high-lift systems, which are morphing systems in their own right. Although these conventional systems perform well, they have detrimental effects on aerodynamic performance of an aircraft as they rely on hinged control surfaces which can produce significant flow separation when actuated fully. Technological advancements in recent years have fueled research and development into new mechanisms that allow new configurations to meet each requirement. With the recent development of advanced materials and wider mechanism integration, engineers have managed to develop special materials such as aero-elastic skins that are capable of permitting significant structural modification through elastic deformations (Ying Shan et al., 2008; Barbarino et al., 2014). As is well known concept that morphing skin signifies a major problem for morphing technologies (Gandhi and Anusonti-Inthra, 2008; Thill et al., 2008; Olympio et al., 2010). Instead, very few of the concepts for morphing skin deal with the conflicting problems are requiring a smooth and continuous surface that contains adequate structural compliancy while adequately carrying the aerodynamic loads. Many researchers have already mentioned about the benefits and drawbacks of morphing aircraft in details (Min, Kien and Richard, 2010; Barbarino et al., 2011; Weisshaar, 2013). Moreover, significant number of studies completed using wing/winglet twist, span, sweep and chamber change (Abdulrahim et al., 2005; Bourdin, Gatto and Friswell, 2007; Falcao, Gomes and Suleman, 2011; Kaygan and Gatto, 2014, 2015, 2016; King, Woods and Friswell, 2015; Kaygan, E., Gatto, 2018; Ulusoy et al., 2019; Kaygan, 2020). It seems that the majority of researchers have concentrate on twist morphing application to eliminate discrete control surface and also to improve aerodynamic performance of an aircraft in all flight regimes. One example of the recent development and application of morphing in high lift devices is the Airbus AlbatrossONE(AIRBUS, 2020). It's a small -scaled, remote controlled airplane implemented with semi-aeroelastic hinger wingtips. These moving wingtips help to combat the effects of turbulence, increase the rate of roll as compared to conventional fixed-wing tips. They also help to reduce drag, that would consequently lower the CO2 emissions. Looking to the future though, the need for more efficient aircraft is expected to remain prevalent, forcing designers to look, once again, at these morphing techniques as a means of improving aircraft operations. Although varied and diverse (Jha and Kudva, 2004), at present, the goal of producing a viable alternative to existing aircraft control methodologies remains elusive. The motivation of this study is to analyze aerodynamic performance of a Predator MQ-1B (Fig. 2) with variable wing concept. The concept consists of variable twist ($-10° < \phi < +10°$, in steps of $\pm 2.5°$) and wing sweep ($0° < \Lambda < 30°$, in steps of $+10°$) to illustrate morphing wing's performance benefits. Hence, the rest of this paper will express the numerical analysis of selected twist and sweep cases.

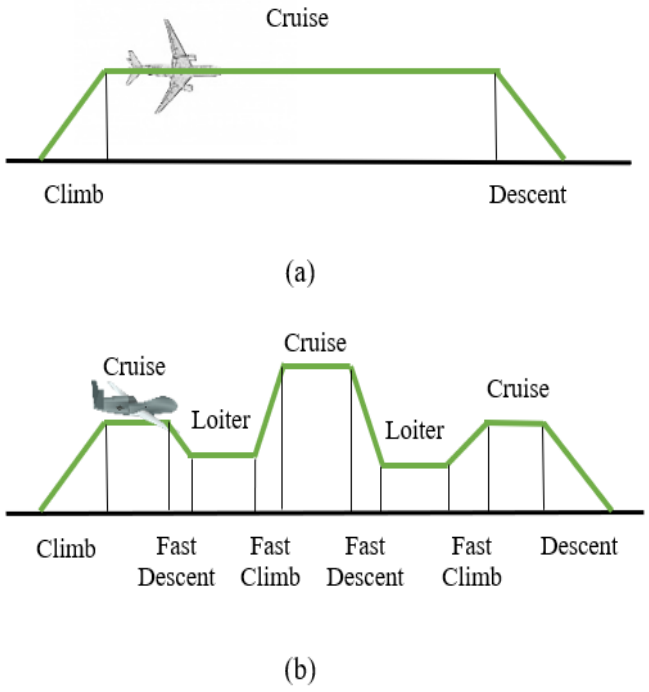

Fig. 1. Comparison of mission profiles between; (a) a commercial airliner and (b) surveillance UAV.

2 Numerical Method and Analysis

2.1. Aircraft flight envelope (gust included)

The MQ-1 Predator wing model chosen for this study (Fig. 4). The MQ-1 Predator is a UAV manufactured by General Atomics for the U.S. Air Force. It is a medium-altitude, long-endurance, and large fixed-wing tactical aircraft (Force., 2009). The main wing configuration covered a NACA2414 airfoil section (due to low camber, moderate thick and possible use in glider application), and 1.25° leading edge sweep angle, 16.8m wing span, 1.130m root chord, 0.4m tip chord, with aspect and tip ratios of 21.96 and 2.82 respectively. In order to investigate morphing wing performance for dissimilar flight regimes, prearranged values of wing sweep ($0° < \Lambda < 30°$, in steps of +10° as shown in Fig. 6) and twist ($10° < \phi < 10°$, in steps of ±2.5° as shown in Fig. 5) are investigated.

Fig. 2. Picture of MQ-1B Predator (Predator, 2015)

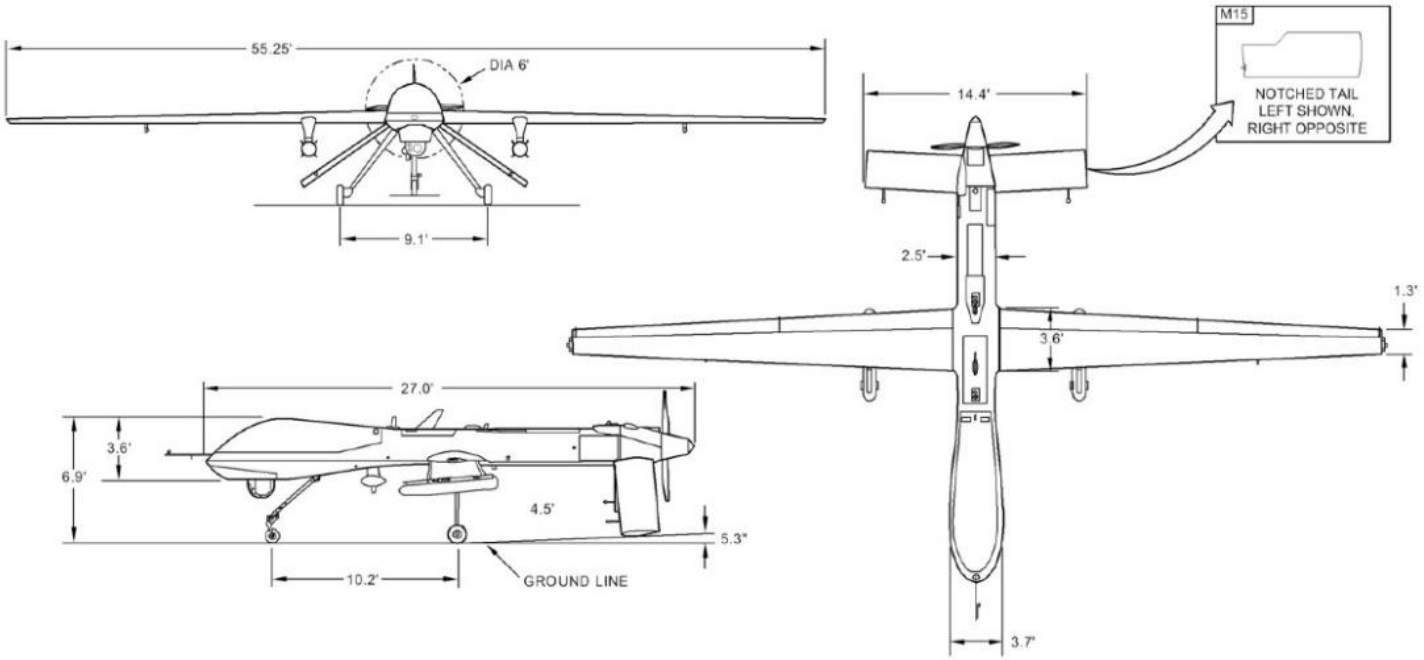

Fig. 3. Design dimensions of MQ-1B Predator UAV(Force., 2009)

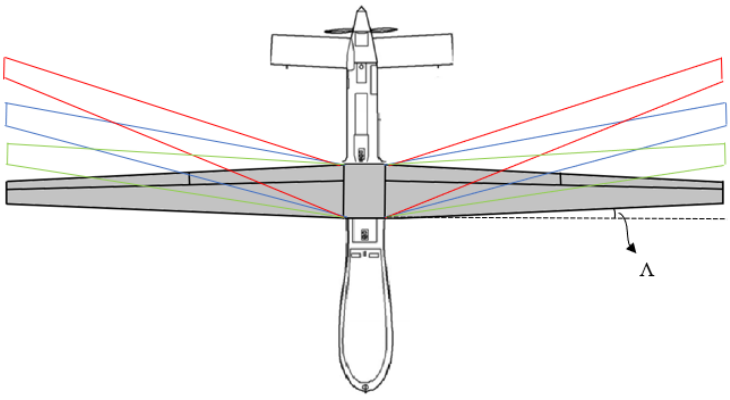

Fig. 4. Sweep wing variations for MQ-1B Predator UAV.

2.2. Aerodynamic and Computational Method

The aerodynamic modelling and numerical computations were carried out using Athena Vortex Lattice (AVL) software. Athena Vortex Lattice is a software used to analyze rigid aircraft's aerodynamics and flight dynamics with any configuration. It uses a slender-body model for the fuselages and nacelles and an expanded vortex lattice model for lifting surfaces. It is possible to specify general nonlinear flying states. The entire linearization of the aerodynamic model for any flight state and the specified mass attributes are combined in the dynamic flight analysis. The software mainly utilizes the extended vortex lattice method in obtaining aerodynamic components. For all simulations, a finite number of panels are used to cover the entire wing, as seen in Fig. 7. A series of horseshoe vortices are superimposed such that every panel has a horseshoe vortex represented by a group of letters. The entire wing is covered in a lattice of horseshoe-shaped vortices, each with a different vortex strength. The normal velocity induced by all horseshoe vortices at every control point is determined using the Biot-Savart Law.

One of the selected panel models is shown in Fig. 5. One of the selected panel models is shown in Fig. 5. For each panel, the same processes are followed to obtain the total vortex strength. The set of simultaneous algebraic equations that form when the flow-tangency condition is applied to all control points can be solved to ascertain the unknown vortex strengths. The velocity at the control point of the panel is calculated by solving the formulas shown in Eq 1. and are the magnitude vectors of and respectively (Eq 2). The influenced matrix is created to solve the required vortex filament strength by multiplying the vortex strength vector and the free stream velocities as illustrated in Eq 3. (Where A is a non-linear function of a matrix depending on the wing shape, b is a vector that can be changed by varying the angle of attack and is the given freestream velocity) (Saffman, 1992).

$$\mathbf{w} = \frac{\mathbf{I}}{4\pi}\frac{r_1 \times r_2}{|r_1 \times r_2|}\left[r_0 \cdot \left(\frac{r_1}{R_1} - \frac{r_2}{R_2}\right)\right] \quad (1)$$

$$R_1 = \sqrt{(x+h)^2 + (y+k)^2}\ R_2 = \sqrt{(x-h)^2 + (y-k)^2} \quad (2)$$

$$\mathbf{A\,I} = U_\infty . \mathbf{b} \quad (3)$$

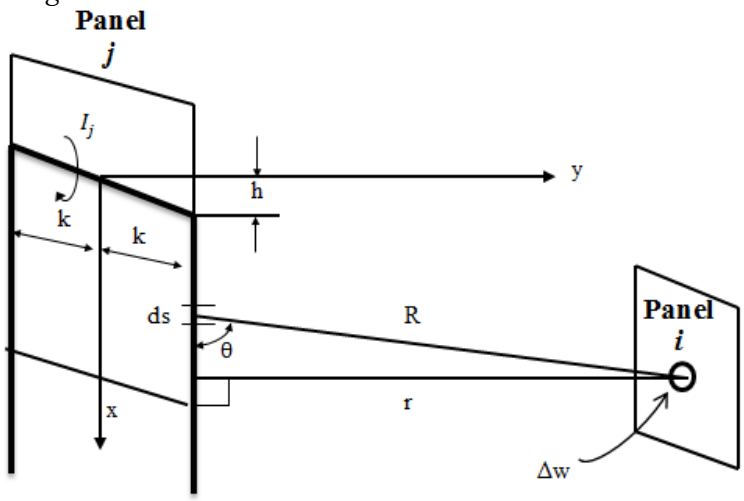

Fig. 5. Selected panel in three component vortex lines for Vortex Filament Strength

In order to compute the shape changing configuration such as the twist and sweep angle, the relevant aerodynamic panel grids are deflected. This modelling method provides efficient and adequate solutions for the quick determination of the aerodynamic performance of the model being analysed. The vortex strength of the plane is determined by summing the multiplied vortex strength and rotation rates, as well as the velocities through following:

$$I = uI_u + vI_v + wI_w + pI_p + qI_q + rI_r + \delta_e I_{\delta_e} \quad (4)$$

After solving the vortex strength of each panel, the Kutta-Joukowsky Law (Saffman, 1992) is applied to obtain the force and moments on each panel over all of the bound vortex segments (Eq 5).

$$dF = \rho U_\infty \times I\,dl \quad (5)$$

The lift force is obtained thereafter by integrating the panel lift distribution. The lift coefficient for a wing can then be calculated using Eq 6.

$$C_L = \frac{L}{\frac{1}{2}pV^2S} \quad (6)$$

Once the wing loading of the structure had been calculated, the variation between the flow angle and freestream velocity for each panel can be obtained. To determine drag force, each panel's lift vector is rotated backwards relative to the freestream direction and integrated as follows:

$$dF = \rho U_\infty \times \mathrm{I}\,dl \sin(\alpha) \quad (7)$$

with the drag coefficient being calculated as;

$$C_D = \frac{D}{\frac{1}{2}pV^2S} \quad (8)$$

(Where dF is a force acting on an infinitesimal vortex segment, ρ is an air density, I is a displacement vector along an infinitesimal vortex segment, dl is a displacement vector along an infinitesimal vortex segment, U_∞ and V are the given freestream velocity) For all simulations, the free-stream velocity was set to 40m/s and all results were calculated without the influence of compressibility. In order to be computationally efficient, a grid refinement study was performed on the baseline configuration prior to widespread use of the developed model. Based on grid efficiency results, all subsequent computations were based on 20 horseshoe vortices along the wing chord, and 64 along the semi-span of the baseline wing (totally 1280 panels).

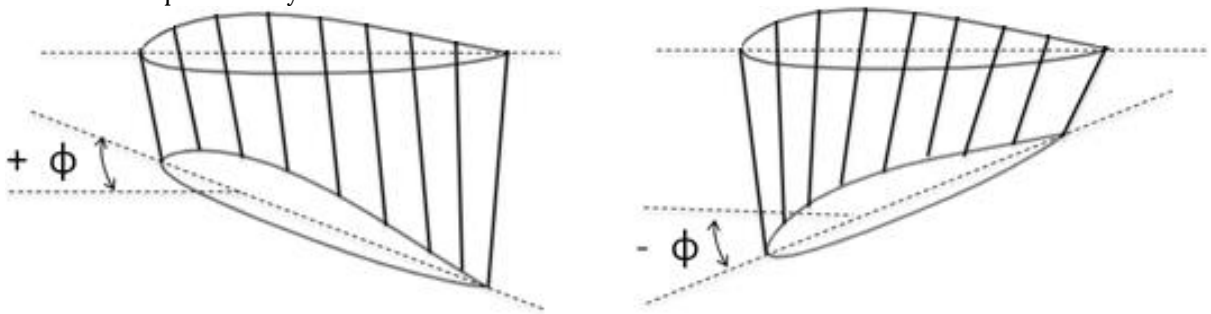

Fig. 6. Schematic view of an active wing: Positive twist angle (washin) and negative twist angle (washout).

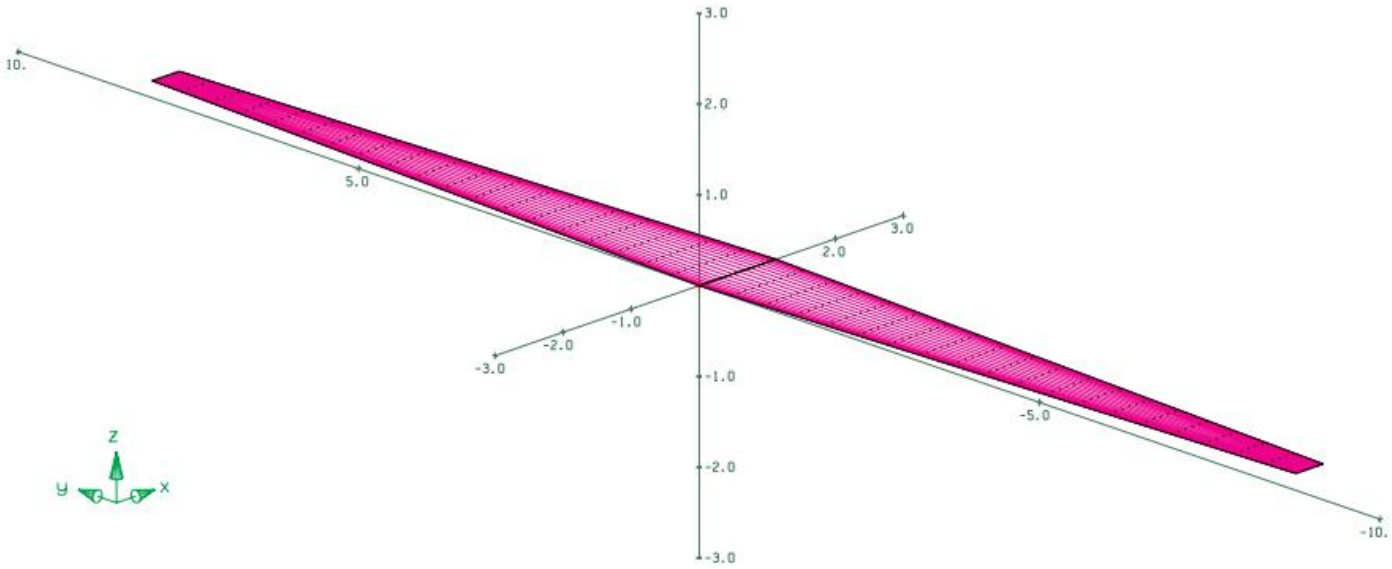

Fig. 7. Athena vortex lattice model morphing wing

3. Results and Discussion

3.1. Effects of Wing Twist and Sweep on Lift and Drag Characteristics of an Aircraft

Fig. 8 shows lift coefficient results for variable twist and sweep cases of an aircraft. It can be seen that increasing or decreasing twist angle of the variable wing producing a corresponding increase and decrease in lift coefficient. Maximum lift obtained at maximum twist angle deflection (ϕ =+10°) for all variety of α. This would be expected as increasing positive twist angle cause to increase effective angle of attack of a morphing wing which tends to improve lift production. Considering sweep angle change with twist angle deflection, at α=0°, is approximately linear with respect to sweep angle for each twist angle change. As increasing sweep angle to 30°, there will be a reduction in lift coefficient results except for ϕ =-10°, because sweeping a wing backwards tend to take longer for both airflows to travel over the airfoil, resulting in less lift production (Galantai, 2010). Similarly, at α=4°, with respect to, changing wing sweep angle does have a detrimental effect on lift production with for the most part. Looking through to Fig. 8 (c) and (d), the actuation of the wing twist gives a marked increase in as increasing angle of attack to higher than 4°. Considering flow change at ϕ =+10° from ϕ =-10° contributes positive lift effects approximately 60% (at Λ=0°). On the other hand, these effects are opposite for sweep angle. Increasing sweep angle reduce lift production as agreement with (Babigian and Hayashibara, 2009). Moreover, for all sweep cases, it can

be seen that reducing twist angle from +10° to -10° tends to reduce lift coefficient results as well. This would be expected due to both net reductions in effective angle of attack as the wingtip moves out of the wing plane and contribution to overall lift production reduces (Phillips, 2004). Similar results were found in (Smith et al., 2012) where experimental results present greater for higher positive twist angles Results for drag coefficient (Fig. 9) also show significant changes with wing twist angle change. Initially, at all range of angle of attack, presented results illustrate that wing twisting help to decrease the formation of the wingtip vortices and can be count as a method to alter the load distribution of the wing. Maximum drag coefficient for these conditions were obtained at a maximum twist angle of ϕ = +10° compared to other twist wing configurations. As increasing angle of attack to maximum, results illustrate clear indication for drag reduction in negative twist angles (37.5% and 17.6% at ϕ =-10° comparing to ϕ =+10° and ϕ =0° respectively). Proof of this can be seen in the significant number of studies available in the recent works indicating increased downwash angle tends to increase drag coefficient results dramatically (Kaygan and Gatto, 2014; Kaygan and Ulusoy, 2018; Smith et al., 2012). Furthermore, comparing results with angles of attack of 8°, 4°, and 0°, similar results also be found which showed marked increases at the extremities of twist angles (positive twist) and angles of attack tested as the wing tip becomes more aerodynamically loaded. Due to increased sensitivity to the onset tip flow separation on wing after α=4°, a dramatic drag increase was seen in most of the positive twist cases presented. A similar trend was observed both computationally and experimentally (Smith et al., 2012) where there is a link between an increment in with positive twist variation to a maximum. Considering sweep angle change, drag coefficient seems to be reduced as well. That is the reason why most of the commercial aircrafts have sweep

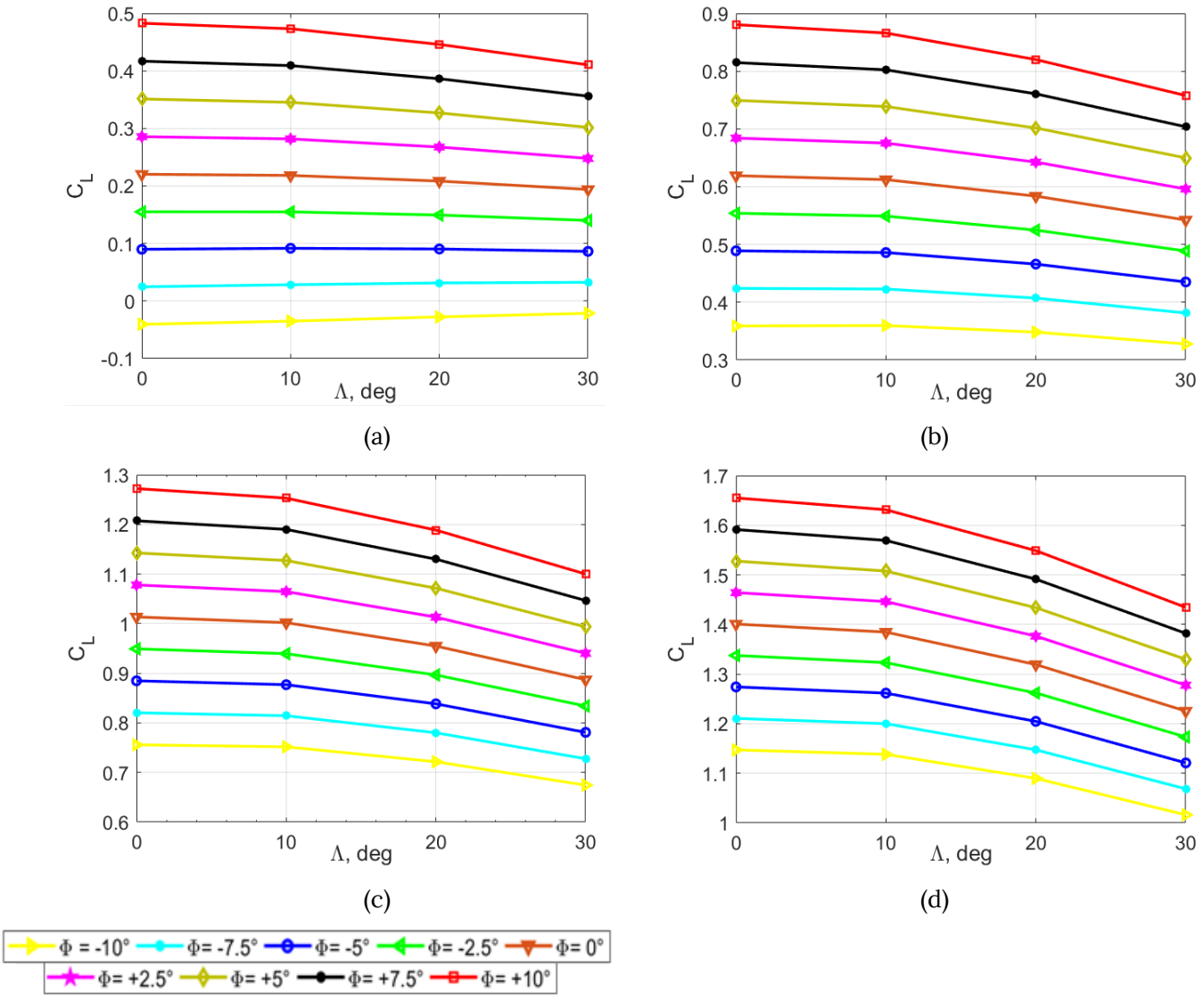

Fig. 8. Effects of changing twist and sweep angle on the lift coefficient (C_L): (a) α=0°, (b) α=4°, (c) α=8°, and (d) α=12°.

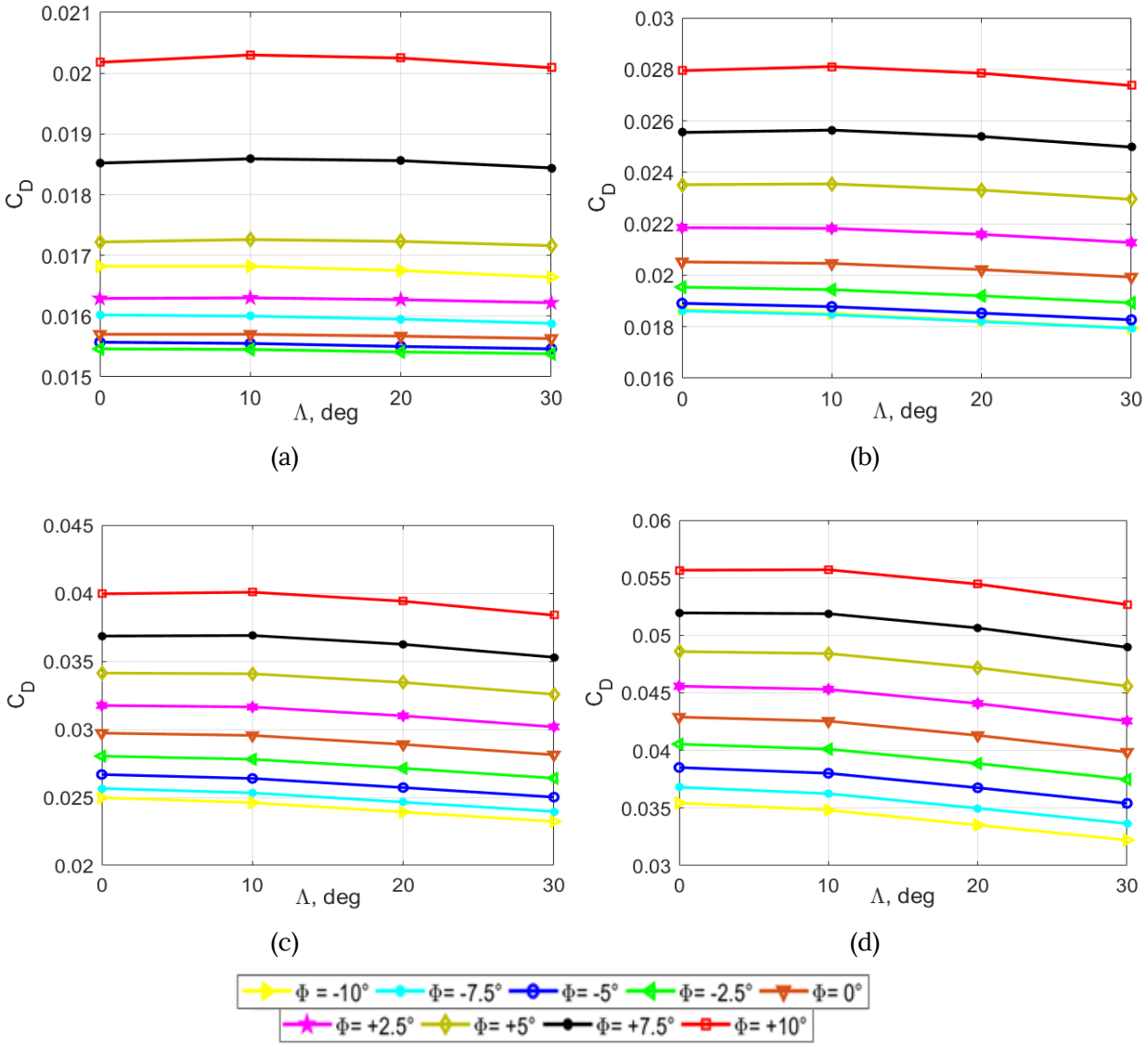

Fig. 9. Effects of changing twist and sweep angle on the drag coefficient (C_D): (a) α=0°, (b) α=4°,(c) α=8°, and (d) α=12°.

back wing configuration to reduce fuel consumptions. Maximum drag reduction was found at 30° of sweep, ϕ =-10° at highest angle of attack (40% comparing to ϕ =+10° and Λ =0°).

3.2. Effects of Wing Twist and Sweep on Aerodynamic Performance of an Aircraft

To summarize the aerodynamic model, Fig. 10 plots Lift to Drag ratio (C_L/C_D) versus sweep angles for various of twist angles. As in general flight philosophy, the lift-to-drag ratio of the aircraft initially rise to the maximum, and then reduce as the angle of attack increases. It can be clearly seen Fig. 10 that when the angle of attack comes 3.3. Discussion to 8°, the best maximum lift-to-drag ratio occurs at ϕ =-2.5° and Λ =0°. Comparing these results with configuration of ϕ =+10° and Λ =0° and configuration of ϕ =+10° and Λ =30°, 7% and 6.6% increment were found respectively. Apparently, considering high angles of attack(α=12°), the negative twist deflection is favorable to improve the lift-to- drag ratio characteristics, while the positive deflection has the contradictory effect. When small angles of attacks are concerned (α =0°), it was observed that the wings with positive twist angle contributed more to the aerodynamic performance of the aircraft. The general trend seems to be continued similarly for α =4°, although there is a slight difference in positive twist angles (maximum ratio was obtained at ϕ =+7.5°). In addition to all, sweep angle change also has an effect on the aircraft's performance. As sweep angle increases, there is a reduction in performance for the most cases are simulated, except for Λ =10°, ϕ =-5°, and α=8°.

3.3. Optimized Morphing Wing Twist and Sweep angle

The recommended winglet configurations were selected in base of the augmentations in the aerodynamic performance of an UAV. Five flight profiles (take-off, climb, cruise, descent, and landing) were proposed to utilize as agreement with (Guerrero et al., 2020) and

according to results: During the movement of an aircraft on the ground, it is recommended to use wing sweep angle as high as possible to reduce wingspan of a wing, hence ϕ= 0° and Λ=30° wing configuration can be used. When aircraft move to take-off stage (1), ϕ= +10° and Λ =0° wing configuration can be used. In this stage, aircraft needs more lift force to easily take off from runway. Moreover, ϕ= +10° and Λ =30° wing model is also be used which performs higher lift slope with low drag profile. In stage (2) at the beginning of the climb phase airplane can set the wing position to ϕ= -5° and Λ =10°. This was taken due to highest lift to drag ratio at high angle of attack. In stage (3), at cruise level where the most of fuel is spending, ϕ= -5° and Λ =10° wing configurations can be used. Alternatively, ϕ= -2.5° and Λ =0° can also be used due to low drag value and higher lift to drag ration. If small angle of attack is considered for cruise, ϕ= -2.5° and Λ =0° would be the best option to reduce fuel consumptions. These configurations sometimes can be changed due to weather conditions, weights and other requirements. Furthermore, increasing twist angle to higher can increase the root bending moments further which may cause adverse effect for aircraft structure. Descents are an essential component of an approach to landing. At this phase (4), lower angle of attack values is concerned. According to the results, ϕ= -2.5° and Λ =0° or ϕ= +7.5° and Λ =0° could be used due to lower drag and highest lift to drag ratio. For other small climb and descent segments or sudden altitude changes, as like stage (2) and stage (4) could be use respectively. After landing, ϕ= 0° and Λ=30° wing configuration can be used. This allows aircraft to reduce wingspan (size) as much as possible to fit regular gates.

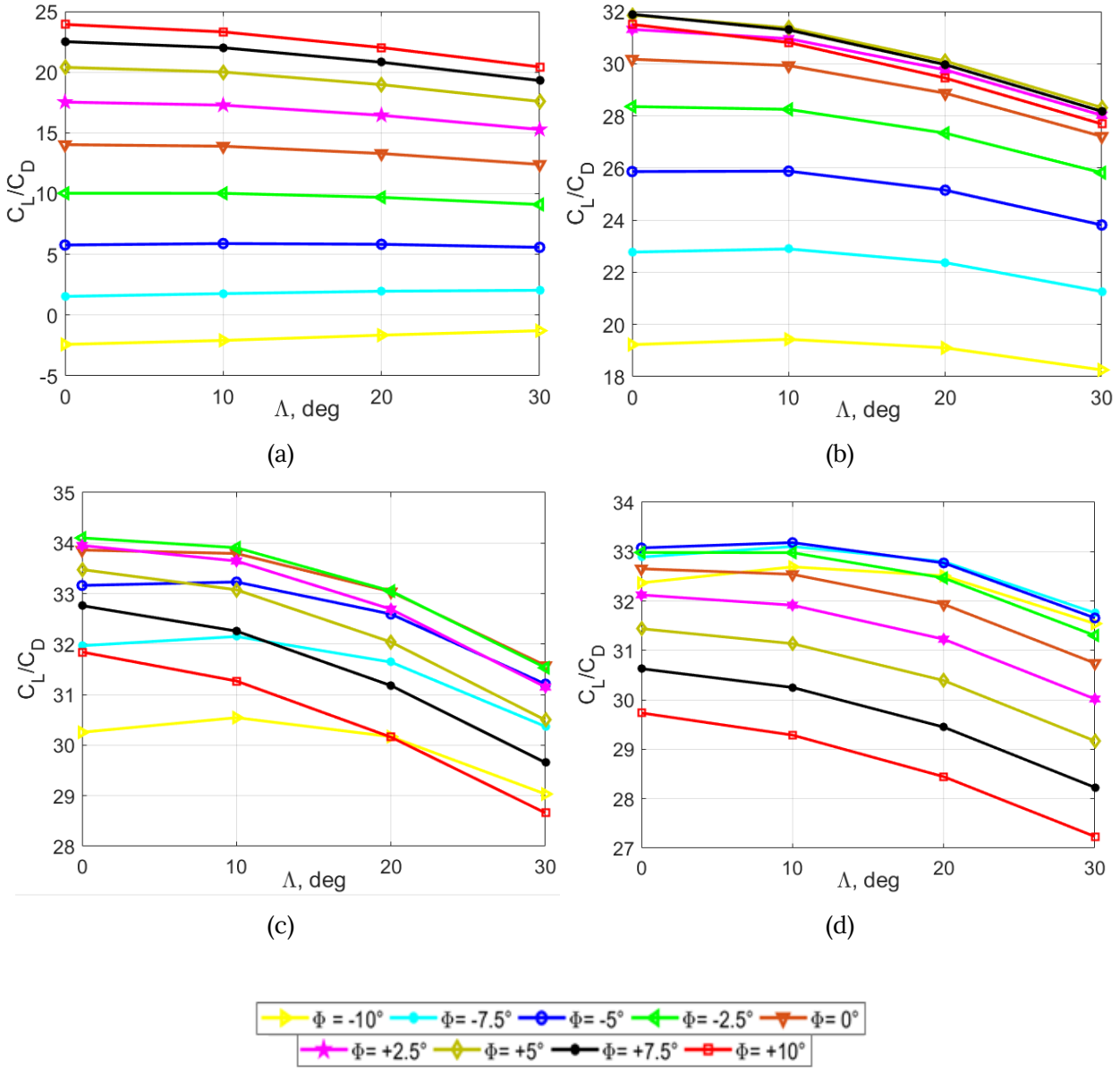

Fig. 10. Effects of changing twist and sweep angle on the lift to drag ratio (C_L/C_D): (a) α=0°, (b) α=4°,(c) α=8°, and (d) α=12°.

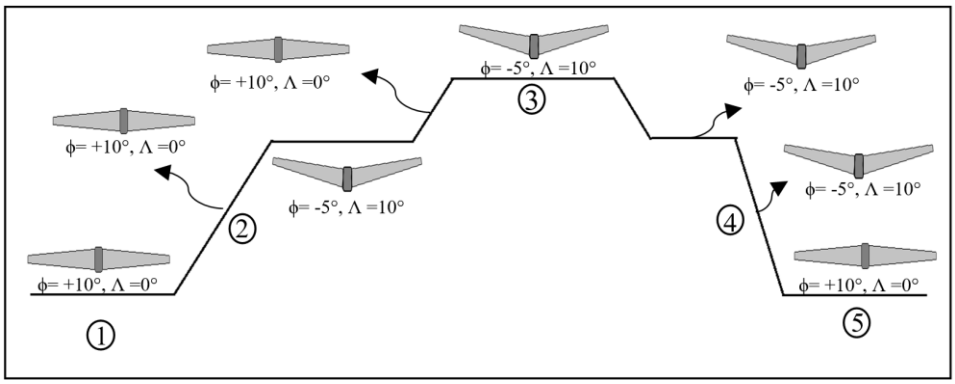

Fig. 11. Optimised Flight Profile

4. Conclusions

The aerodynamic analysis of the variable morphing wing for the Predator MQ-1B was investigated in this paper. From the results, it appears that the overall positive twist configurations have positive effects on lift production and can be applied for flight segments where much more lift is required. In contrast, increasing the negative twist angle to maximum showing lower drag results. Considering the lift/drag ratio, which combines these features, comments can be made about fuel consumption, which is one of the most significant problems related to airlines and general aviation. According to the results, it becomes possible to reduce the fuel cost by adding little sweep angle and also applying negative twist configuration. Overall, the concept demonstrates the possibility of shape changing wing with providing optimum performance benefits. For the future work, the idea of variable wing can be adapted to the UAV and then perform flight tests in order to better understand their effectiveness.

Nomenclature

A	: Wing Area
b	: Wing Span
$\boldsymbol{C_D}$	: Drag coefficient
$\boldsymbol{C_L}$	: Lift coefficient
$\boldsymbol{C_L/C_D}$	: Lift to Drag ratio
c	: Wing chord
i	: Selected wing panel
$\boldsymbol{I_i}$	: Total vortex strength
P	: Density
$\boldsymbol{U_\infty}$	: Freestream velocity
α	: Angle of Attack
ϕ	: Twist Angle
Λ	: Sweep Angle

References

Abdulrahim, M. et al. (2005) 'Flight Testing A Micro Air Vehicle Using Morphing For Aeroservoelastic Control', Journal of Aircraft, 42, No 1(January-February), pp. 1–17. doi:10.2514/6.2004-1674.

AIRBUS (2020) AlbatrossOne: A revolutionary approach to aircraft wing design. Available at: https://www.airbus.com/innovation/future-concepts/biomimicry/albatross one .html (Accessed: 9 July 2021).

Austin, R. (2010) Unmanned Aircraft Systems – UAVs design, development and deployment. Aerospace series, Wiley and Sons Ltd publication.

Barbarino, S. et al. (2011) 'A Review of Morphing Aircraft', Journal of Intelligent Material Systems and Structures, 22(9), pp. 823–877. doi:10.1177/1045389X11414084.

Barbarino, S. et al. (2014) 'A review on shape memory alloys with applications to morphing aircraft', Smart Materials and Structures, 23(6), pp. 063001--. doi:10.1088/0964-1726/23/6/063001.

Bourdin, P., Gatto, A.. and Friswell, M. (2006) 'The Application of Variable Cant Angle Winglets for Morphing Aircraft Control', in 24th Applied Aerodynamics Conference. American Institute of Aeronautics and Astronautics, Inc, pp. 1–13.

Bourdin, P., Gatto, A. and Friswell, M.I. (2007) 'Potential of Articulated Split Wingtips for Morphing-Based Control of a Flying Wing', in 25th AIAA Applied Aerodynamics Conference, pp. 1–16.

Culick, F.E.C. (2003) 'The Wright Brothers : First Aeronautical Engineers', 41(6), pp. 8–11.

Falcao, L., Gomes, A. a and Suleman, A. (2011) 'Design and Analysis of an Adaptive Wingtip', in 52nd AIAA/ASME/ASCE/AHS/ASC Structures, Structural Dynamics and Materials Conference. Denver, Colorado: AIAA.

Force., D. of A. (2009) 'Airfield Planning and Design

Criteria for Unmanned Aircraft Systems (UAS)', 4, pp. 1–51.

Galantai, V.P. (2010) 'Design and Analysis of Morphing Wing for Unmanned Aerial Vehicles', University of Toronto, Canada

Gandhi, F. and Anusonti-Inthra, P. (2008) 'Skin design studies for variable camber morphing airfoils', Smart Materials and Structures, 17(1), p. 015025. doi:10.1088/0964-1726/17/01/015025.

Gomez, J.C. and Garcia, E. (2011) 'Morphing unmanned aerial vehicles', Smart Materials and Structures, 20(10), p. 103001. doi:10.1088/0964-1726/20/10/103001.

Guerrero, J.E., Sanguineti, M., and Wittkowski, K. (2020) 'Variable cant angle winglets for improvement of aircraft flight performance.' Meccanica 55, 1917–1947.

Gundlach, J. (2012) 'Overview of Unmanned Aircraft Systems', Designing Unmanned Aircraft Systems, 2(4), pp. 1–23. doi:10.2514/5.9781600868443.0001.0023.

Jha, A.K. and Kudva, J.N. (2004) 'Morphing Aircraft Concepts, Classifications, and Challanges'. Edited by E.H. Anderson, 5388, pp. 213–224. doi:10.1117/12.544212.

Kaygan, A., Gatto, E. (2018) 'Structural Analysis of an Active Morphing Wing for Enhancing Unmanned Aerial Vehicle Performance', International Journal of Aerospace and Mechanical Engineering, 12(10), pp. 948–955.

Kaygan, E. and Gatto, A. (2014) 'Investigation of Adaptable Winglets for Improved UAV Control and Performance', International journal of Mechanical, Aerospace, Industrial and Mechatronics Engineering, 8(7), pp. 1281–1286.

Kaygan, E. and Gatto, A. (2015) 'Computational Analysis of Adaptable Winglets for Improved Morphing Aircraft Performance', International Journal of Aerospace and Mechanical Engineering, 9(7), pp. 1127–1133.

Kaygan, E. and Gatto, A. (2016) 'Development of an Active Morphing Wing With Adaptive Skin for Enhanced Aircraft Control and Performance', in Greener Aviation 2016. BRUSSELS, BELGIUM.

Kaygan E., Ulusoy C. (2018), 'Effectiveness of Twist Morphing Wing on Aerodynamic Performance and Control of an Aircraft', Journal of Aviation, 2 (2), 77-87. DOI: 10.30518/jav.482507

Kaygan E. (2020), 'Aerodynamic Analysis of Morphing Winglets for Improved Commercial Aircraft Performance', J. Aviat.4 (1), 31-44.

King, B., Woods, S. and Friswell, M.I, (2015) 'The Adaptive Aspect Ratio Morphing Wing: Design Concept and Low Fidelity Skin Optimization', pp. 1–4.

Kudva, J. N., Martin, C. A., Scherer, L. B., Jardine, A. P., McGowan, A. R., Lake, R. C., Sendeckyj, G. P., and Sanders, B.P. (1997) 'Overview of DARPA/AFRL/NASA Smart Wing Program', in Jacobs, J.H. (ed.). Bellingham, WA: SPIE Proceedings, pp. 230–236.

Kudva, J.N. (2004) 'Overview of the DARPA Smart Wing Project', Journal of Intelligent Materials Systems and Structures, 15(4), pp. 261–267. doi:10.1177/1045389X04042796.

McRuer, D. and Graham, D. (2004) 'Flight Control Century: Triumphs of the Systems Approach', Journal of Guidance, Control, and Dynamics, 27(2), pp. 161–173. doi:10.2514/1.4586.

Min, Z., Kien, V.K. and Richard, L.J.Y. (2010) 'Aircraft morphing wing concepts with radical geometry change', IES Journal Part A: Civil and Structural Engineering, 3(3), pp. 188–195. doi:10.1080/19373261003607972.

Olympio, K.R. et al. (2010) 'Design of a Flexible Skin for a Shear Morphing Wing', Journal of Intelligent Material Systems and Structures, 21(17), pp. 1755–1770. doi:10.1177/1045389X10382586.

Phillips, W.F. (2004) 'Lifting-Line Analysis for Twisted Wings and Washout-Optimized Wings. ' Journal of Aircraft vol. 41, no. 1 128-136.

Predator, M.-1 (2015) MQ-1 Predator Air Force Photos. Available at: https://www.af.mil/News/Photos/igphoto/2000597903/mediaid/4705/ (Accessed: 16 June 2021).

Prisacariu, V., Boscoianu, M. and Cîrciu, I. (2013) 'Morphing wing concept for small UAV', Applied Mechanics and Materials, 332(July), pp. 44–49. doi:10.4028/www.scientific.net/AMM.332.44.

Prisacariu, V., Boşcoianu, M. and Cîrciu, I. (2017) 'The effect analysis of the morphing concept on the small swept flying wings', MATEC Web of Conferences, 121, pp. 1–8. doi:10.1051/matecconf/201712101011.

Babigian R., Hayashibara,S. (2009), 'Computational Study of the Vortex Wake Generated by a Three-Dimensional Wing with Dihedral, Taper, and Sweep', 27th AIAA Applied Aerodynamics Conference, no. June, pp. 1–13.

Saffman, P. G.(1992) 'Vortex Dynamics' Cambridge. England, U.K.: Cambridge Univ. Press.

Smith, D. D., Lowenberg,M. H., Jones, D. P., Friswell, M. I. and Park, S. (2012) 'Computational and Experimental Analysis of the Active Morphing Wing Concept',

2012, pp. 1–9.

Thill, C. et al. (2008) 'Morphing skins', (3216), pp. 1–23.

Weisshaar, T. a. (2013) 'Morphing Aircraft Systems: Historical Perspectives and Future Challenges', Journal of Aircraft, 50(2), pp. 337–353. doi:10.2514/1.C031456.

Weisshaar, T.A. and Challenge, T.H.E.M. (2006) 'Morphing Aircraft Technology – New Shapes for Aircraft Design'.

Ying Shan et al. (2008) 'Variable Stiffness Structures Utilizing Fluidic Flexible Matrix Composites', Journal of Intelligent Material Systems and Structures, 20(4), pp. 443–456. doi:10.1177/1045389X08095270.

International Journal of Aviation Science and Technology

Research Article

A Comprehensive Study On The Effects Of Noise Abatement Departure Procedures On Noise Contours Around Tan Son Nhat International Airport

La Tuan Kiet[1]*, Tien Anh Tran[2]

[1] Ho Chi Minh City University of Technology, Department of Aerospace Engineering, Vietnam
kiet.latuann@gmail.com - 0000-0001-5680-2780

[2] Ho Chi Minh City University of Technology, Department of Aerospace Engineering, Vietnam
tienanh@hcmut.edu.vn - 0000-0001-6090-0965

Abstract

In recent years, accompanied by economic growth, air transportation in Vietnam has rapidly risen with the introduction of many new airlines. This situation has led to an increase in aircraft movement frequency flying in and out of the airports and raised concerns about the effects of increased noise exposure levels on public health and the natural environment in the vicinity of the airports. Vietnam authority has also issued several documents to regulate the establishment of the noise contour maps to evaluate the current noise exposure levels around airports in Vietnam and recognized the noise problem in aviation as a significant issue. One of four measures to reduce the noise around airports introduced in the Balanced Approach to Noise Management of the International Civil Aviation Organization is noise abatement operational procedures. This research is one of the first attempts to provide a comprehensive study on predicting the noise levels and establishing noise contour maps around Tan Son Nhat International airport with the assumption that aircraft take-off following the noise abatement departure procedures 1 and 2 using MATLAB software. The computed noise contours for both procedures show that the day-evening-night equivalent noise levels range from 45 dB(A) to 60 dB(A) around the airport, with the difference in noise levels between the two procedures primarily occurring at the end of the runway due to the difference in stepped departures. These results provide a reference for the authorities to study further in applying suitable noise reduction plans in the vicinity of airports.

Keywords

Airport noise contours,
Noise abatement departure procedures,
Noise contours,
Noise contours map,
Noise map

Time Scale of Article

Received 5 May 2022
Revised until 25 May 2022
Accepted 4 November 2022
Online date 29 December 2022

1. Introduction

Noise exposure levels generated by aircraft movements around airports are recognized as a critical issue that has far-reaching effects on the health of those living near airports. Many developed countries have established noise contour maps combined with noise monitoring systems in the vicinity of the airports as an effective way to assess the noise exposure levels generated by flight operations. However, in the rest of the world, especially in many developing countries, evaluating the effects of noise and proposing measures to reduce the area affected by high noise exposure levels is still challenging due to restricted data assessed and technical limitations. Various international studies related to noise issues around airports have been conducted in recent years, such as: (Paulo, 2012) provide a method to compute the noise level and plot

*: Corresponding Author La Tuan Kiet, kiet.latuann@gmail.com
DOI: 10.23890/IJAST.vm03is02.0203

the noise contours around airports using measured data conducted in the street instead of using specific software. With this method, the noise levels generated by aircraft operations can be computed, and the noise contours can be plotted without the need to measure 24 hours in each noise calculation point. (Pertiwe et al., 2018) developed the noise mapping for the case study Adi Soemarmo airport in Boyolali, Indonesia --the second largest airport in Central Java Province, Indonesia-- using MATLAB software. The results showed that the Weighted Equivalent Continuous Perceived Noise Levels (WECPNL) were in the range of 65 dB(A) to 87 dB(A) based on the data during the busiest schedule in September 2016, with 22 departures and 22 approaches. (Halil et al., 2020) assessed the aircraft noise emission around the International Eskisehir Hasan Polatkan airport using multiple techniques with two main stages. In the first stage of their study, the day-evening-night noise levels were simulated using IMMI software. The result showed that the noise level around the airport did not exceed the maximum allowable limit based on local law. The noise field measurement was conducted during the second stage to assess the noise level generated by the most operated aircraft Cessna 172-S in the concerned airport using TESTO 812 type-2 sound level meter. The result showed that the noise level created by this type of aircraft exceeded the lowest exposure limit, and then some measures aimed to prevent the noise level were examined. Numerous domestic and foreign researchers have conducted various studies on assessing noise problems around some major airports in Vietnam in both analytical and experimental methods. Some of these studies can be listed as following: (Ha et al., 2010) joined the project investigating and evaluating air and noise pollution, thereby establishing a noise map around Tan Son Nhat International airport and supposing solutions to reduce the effects. (Lan et al., 2019) conducted much research related to the effects of aircraft noise on the health of the community living around Noi Bai International airport. (Loc et al., 2019) compared the noise contours calculated using noise-power-distance data provided by EUROCONTROL and the measurement-based noise-power-distance data for Noi Bai and Da Nang International airports. (Lien et al., 2019) presented the response of the community living around the Tan Son Nhat airport to aircraft noise changes by comparing two surveys conducted 11 years apart in Ho Chi Minh city. (Tuan et al., 2021) described comprehensively the structure of the noise monitoring and control system expected to be deployed in the Tan Son Nhat International airport. Most of these research has shown that the aircraft noise has considerably affected the quality of living for the communities living around these airports. The previous research conducted in 2020 showed that the day continuous equivalent noise levels created by aircraft taking off from Tan Son Nhat International airport during the day-time from 0700 to 1900 range from 60 to 70 dB(A) within the departure zone area. The noise levels at some noise-sensitive points, such as at the university, hospital, workplace, and so forth, were obtained using an analytical method and verified through some noise field measurements using the Larson Davis noise measurement device. The method to determine noise levels used in this research is an inheritance and development from the previous research and will be described in section 2. The computed noise results at some noise-sensitive areas in the departure zone of the airport demonstrated exceeding the permissible noise levels given by Vietnamese Law (Kiet, 2019). To prevent the effects of aircraft noise and narrow the affected area of communities living in the vicinity of the airport, this is necessary to consider studying to apply some measures recommended by ICAO and stated in the Balanced Approach to Noise Management. Four measures to reduce the noise introduced by ICAO include: Reduction of noise at source, Noise abatement operational procedures, Operating restrictions, and Land-use planning and management. Based on the current situation at the Tan Son Nhat International airport, the airport is located inside a high-density of population, and the noise exposure levels generated by flight operations were demonstrated that exceed noise limits. This paper chose the noise abatement departure procedure to study as a part of an intensive effort to reduce the noise exposure levels generated by aircraft operations to the sensitive population living around the airport. It can be seen as the next step in predicting and evaluating noise levels created by flight operations with the assumption that aircraft fly out of the airport applying the noise abatement departure procedures – one of the recommended measures to reduce the noise problem in the vicinity of airports- on the noise contour maps around Tan Son Nhat International airport. In this study, the noise abatement departure procedures are assumed to be applied; therefore, it can be seen as a future scenario. Flightpath analysis must be conducted to obtain the noise levels generated by the specific NADP 1 and NADP 2 flight paths.

2. Method

The level and extent of noise levels created by aircraft movements following NADP 1 and NADP 2 are computed in terms of noise contours. It is done by collecting the data of the target airport, statistically analyzing the number of movements, the type of aircraft operating at the airport, and representative flight path analysis for each aircraft type with specific flight procedures. In this research, ICAO's flight path segmentation modeling mentioned in Document 9911

(ICAO, 2009) is used to compute the noise levels around Tan Son Nhat International airport. After that, the flight mechanics equations from SAE-AIR-1845 are used to determine the flight profile when the aircraft departs assumed following NADP 1 and NADP 2. Finally, the Noise Power Distance table from EUROCONTROL is used to interpolate or extrapolate the noise levels propagated from the aircraft to the ground. The process of establishing the noise contour maps for two different flight paths using noise abatement procedures is described in the following figure.

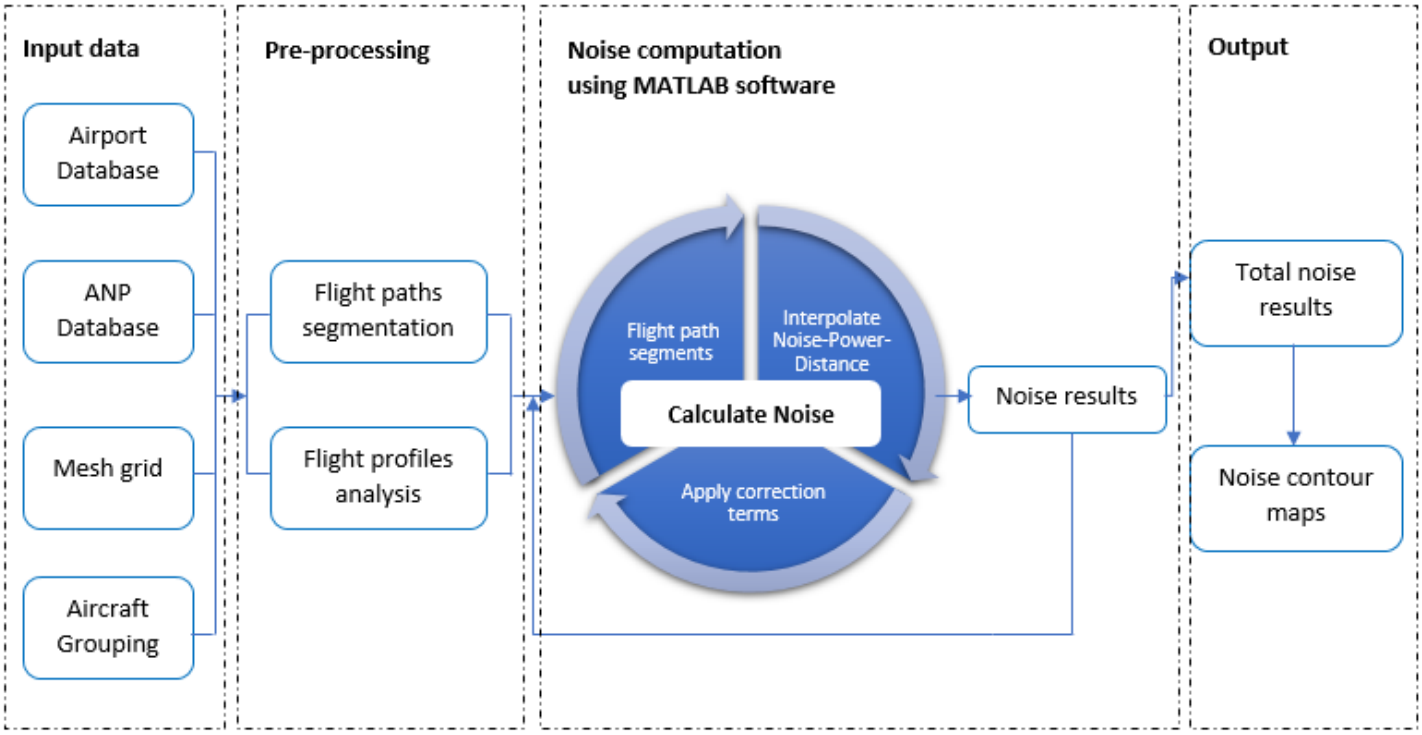

Fig. 1. The general process to compute the noise contours around Tan Son Nhat International airport

As shown in Figure 1, the general process to obtain the noise contours generated by aircraft movements following NADP 1 and NADP 2 is divided into four main steps: Input data, Pre-processing, Noise computation, and Output. To complete the first step, this is necessary to collect information about the Tan Son Nhat International airport. This step was done by gathering the airport data by assessing the Aeronautical Information Publication (AIP) issued by the Civil Aviation Authority of Vietnam (CAAV) at the time of research. The Aircraft Noise Performance database is one of the essential data needed to compute the noise contours. This database is controlled by EUROCONTROL and can be freely accessed through the website. The database contains the noise levels related to the slant distance between the noise source and the noise receiver point and the aircraft's engine thrust in different metrics widely applied to evaluate the effects of aircraft noise levels in most countries globally. It also provides information about the performance of many aircraft operating at most busy airports recently. The noise computation domain surrounding the Tan Son Nhat International airport is limited with the assumption that the aircraft do not change its heading to the start of roll stage within the entire computation domain. The process of generating the mesh grid to cover the computation domain is described in section 2.3. In the pre-processing step, the flight path segmentation modeling described in Document 29 of the ECAC is used to analyze the flight path of each representative aircraft when they are assumed to depart following the NADP 1 and NADP 2. These specific noise abatements take-off procedures are guided in Document 8168 of ICAO, pointing out a sequence of procedural steps that the aircraft must follow to satisfy the noise reduction purpose in the departure zone of the airport. These mentioned steps are done by computing some critical parameters such as rate of climb, altitude, and calibrated airspeed using flight mechanics equations found in the Aerospace Information Report 1845 published by the Society of Automobile Engineers (SAE). After obtaining the flight paths and flight profiles for the specific noise abatement departure procedure, the flight path of each representative aircraft is segmented into small segments, such as the velocity of two adjacent

segments not being more significant than 10.3 m/s (20 kt). Due to the aircraft is assumed not to change its heading in the whole computation domain, the aircraft bank angle would be zero. Only three main parameters, including the aircraft's velocity, engine thrust, and height at each sub-segments start-point and end-point, are determined. The unique parameters representing the whole segment will be found based on the geometry relationship between the flight path segment and the noise grid. A code was designed using MATLAB software to compute the noise exposure levels created by each segment of each representative aircraft to the noise grid and then compute for a single flight path. This procedure is repeated to obtain the noise exposure levels generated by the rest of the flight paths of the representative aircraft. Finally, the noise contours will be obtained using the natural neighbor's interpolation technique described in section 2.3. The day continuous noise level (L_{day}) and the day-evening-night continuous noise level (L_{den}) is computed by adding the contribution of all aircraft operating during the time of research which is weighted to account for the difference in the background noise during the day, evening and night time.

2.1 Airport data collecting

Located inside the high density of the noise-sensitive area with a distance of only 6.5 km North West from Ho Chi Minh City center, Tan Son Nhat International Airport - the case study of this research, is one of the largest and busiest airports in Southern Vietnam, serving more than millions of passengers annually in normal operating conditions. The airport uses two parallel runways, including RWY 25L/07R and RWY 25R/07L. The dimensions of these runways are 3828 m x 45 m and 3050 m x 45 m, respectively (AIP Vietnam, 2021). In the scope of this research, all flight operations collected in March 2020 took place in the runways 25R and 25L, with RWY 25L primarily used for take-offs and RWY 25R primarily used for landings. Theoretically, the noise levels computation can be separated into two runways. However, due to the two runways used at Tan Son Nhat International airport being close to each other (365 m), it is assumed that both take-off and landing operations of aircraft taking place on the single runway 25L (CAAV, 2019), then all noise computations are conducted using the dimension and direction of the RWY 25L

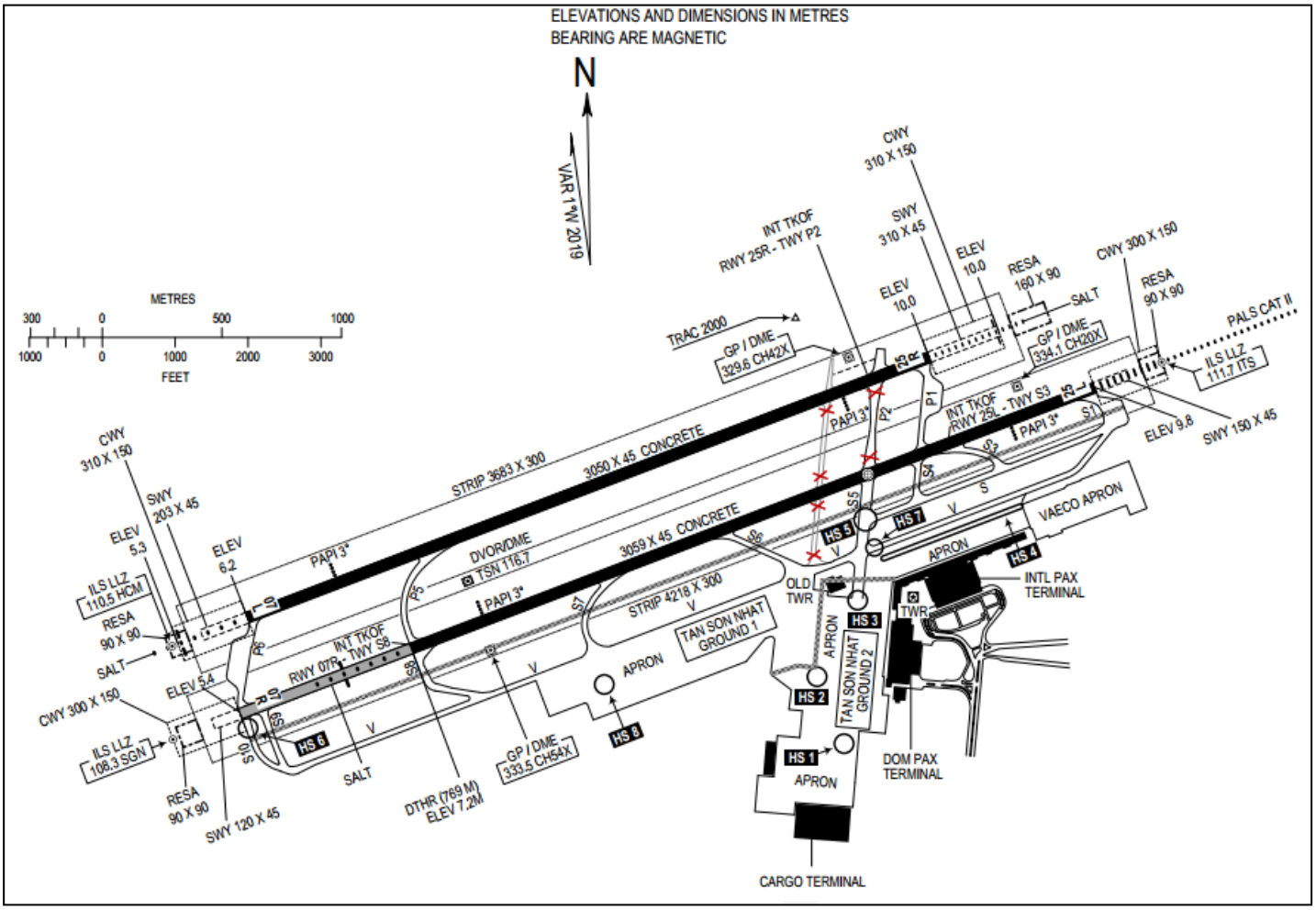

Fig. 2. ICAO Aerodrome Chart of Tan Son Nhat International Airport (AIP Vietnam)

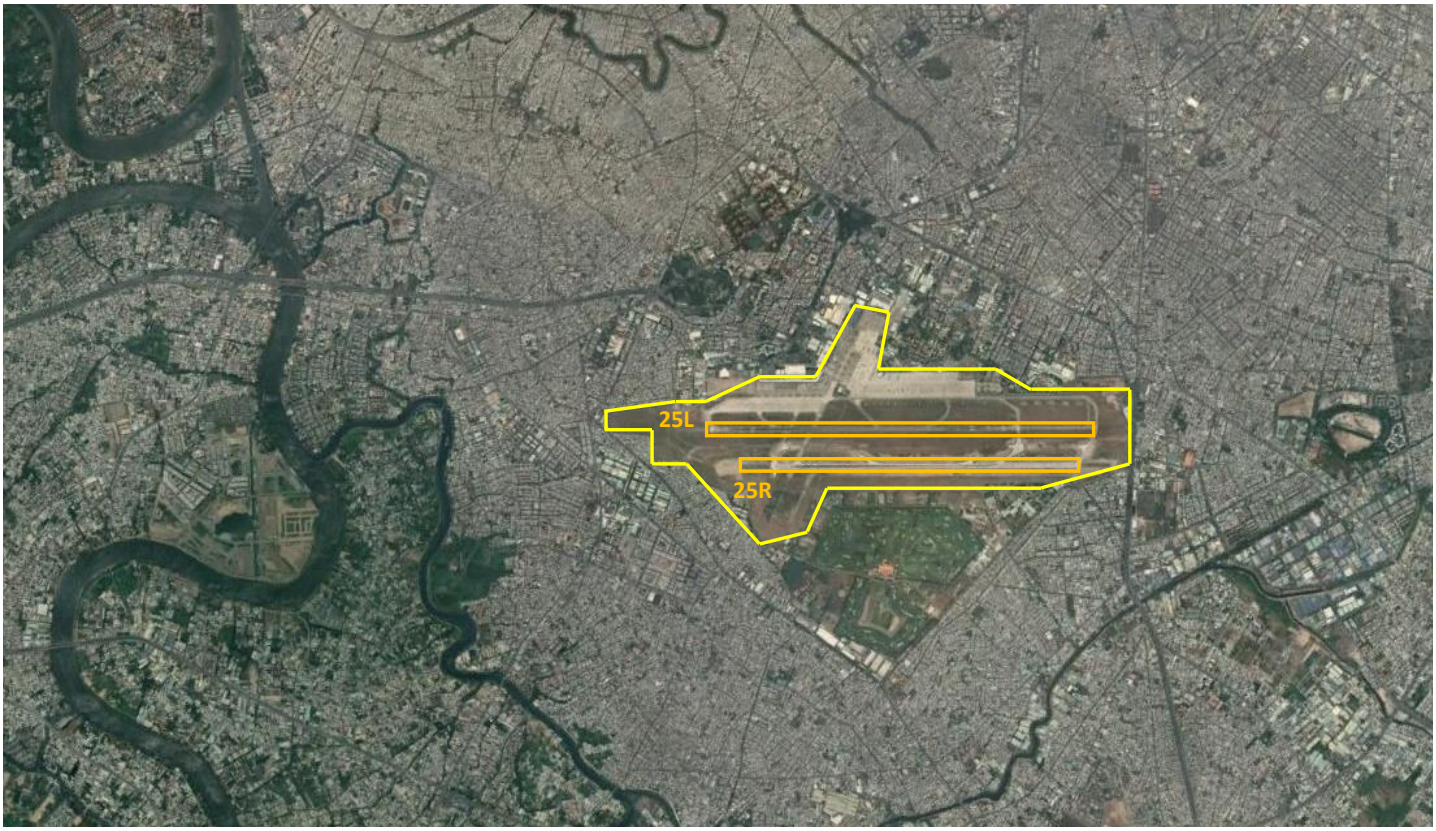

Fig. 3. Tan Son Nhat International Airport

2.2 Aircraft Noise Performance Database

The Aircraft Noise Performance (ANP) database is an essential and necessary database for calculating aircraft noise contours. The ANP database is maintained and managed by the United State Department of Transport, EUROCONTROL, and the European Aviation Safety Agency (EASA). This database provides aircraft performance and noise characteristics for more than 150 civil aircraft types as the airframe/engine combinations, used to determine the maximum and exposure-based noise metrics. This database is consistent with the noise contours calculation methodology described in the Aerospace Information Report (AIR) 1845 of the Society of Automobile Engineers (SAE), Document 9911 of the ICAO, and Document 29 of the ECAC. The details about this ANP database can be found in Appendix G, Volume 2, Document 29 of the ECAC. The Noise-Power-Distance (NPD) table is a part of the Aircraft Noise Performance database. The table provides the noise levels in different metrics as a function of the slant distance from the noise source to the ground and the engine thrust. These values were collected based on field noise measurements conducted some days in the United States. The noise exposure levels generated by each sub-segment of the single flight path can be obtained by interpolating or extrapolating this table with the engine thrust and slant distance computed using the flight mechanics equation and geometry relationship.

2.3 Noise mesh grid generation

The range of the noise computation domain is limited to ± 7260 m (25000 ft) on the horizontal axis and ± 3658 m (12000 ft) on the vertical axis, with the origin (0,0) located at the start-of-roll point on runway 25L. The unstructured grid using Delaunay triangulation covers the computation domain generated using GMSH software. The principle of using the unstructured grid is to divide the continuous noise computation domain into discrete points where each point is the intersection of the Delaunay triangulation's edges.

The noise exposure levels generated by aircraft movement will be computed at each discrete point. There are 1678 nodes in total, each node equivalent to each noise receiver point. An interpolation technique is used to interpolate the noise levels for the entire computation domain. Numerous research has been conducted in the field of interpolation techniques (Yen et al., 2020; Tan et al., 2014; Hugo et al., 2009). In the scope of this research, these techniques are not described in detail. The natural neighbor interpolation technique was chosen to interpolate the noise levels when some research proved that this technique has certain advantages and gives better results than most other interpolation techniques for surface modeling (Yen et al., 2020).

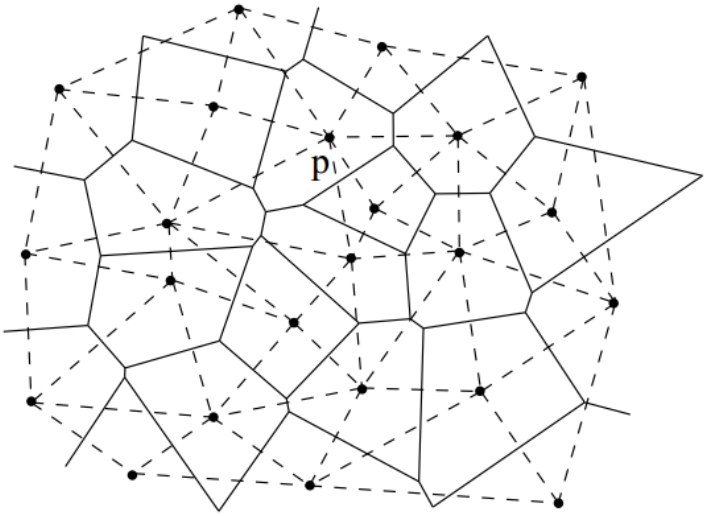

Fig. 4. Voronoi diagram and Delaunay triangular (Hugo Ledoux & Christopher Gold, 2005)

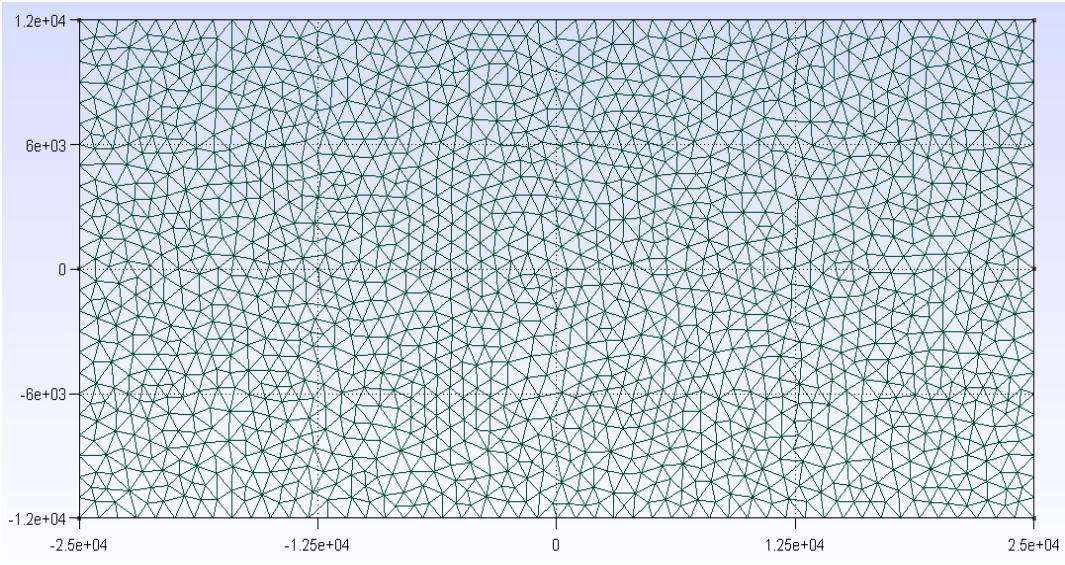

Fig. 5. The mesh grid of noise computing domain

2.4 Aircraft grouping

In March 2020, aircraft data operating at Tan Son Nhat International Airport consisting of aircraft type and operating frequency were collected and statistically analyzed using Flightradar24 web-based application. There have been 5063 flight operations for take-off and landing pairs of 15 aircraft types with 84 specific engine-airframe combinations. Theoretically, noise levels could be calculated for specific aircraft types with engine-airframe combinations. Nevertheless, this approach will take a significant amount of time and resources. An alternate method is to group individual aircraft types having similar noise and performance characteristics so that a single aircraft category can represent them (ECAC, 2016). The aircraft types operating at Tan Son Nhat International Airport were grouped based on the criteria recommended in Document 29 of the ECAC:

Table 1. Parameters for aircraft grouping

Criteria	Description
Maximum take-off mass	light, medium, heavy aircraft
Type of engine	turbojet, turbofan, and turboprop
Number of engines	two, three, or four engines
By-pass ratio	low, medium, high
Installation of the engines	rear-fuselage-mounted engines and wing-mounted engines
Type of operation	departures and arrivals
ICAO noise certificate	based on noise certification according to ICAO Annex 16, Volume 1

Table 2. Aircraft groups and aircraft representatives.

Aircraft Type	Group Name	Aircraft Representative
Airbus A319/320/321, Boeing 737/757	C	Airbus A321-232
Airbus A320/A321 Neo/Neo X*	C*	Airbus A321-232
Boeing 787, Airbus A350, Airbus A330	D	Airbus A350-941
Airbus A340, Boeing 747, Boeing 777	E	Boeing 747-400

Table 3. Aircraft representative and its default weights.

Aircraft Type	Representative Aircraft	Default Weights (kg)
Airbus A320 Family, Boeing 737/757	Airbus A321-232	77000
Boeing 787, Airbus A350, Airbus A330	Airbus A350-941	234000
Airbus A340, Boeing 747, Boeing 777	Boeing 747-400	304000

Table 4. The number of aircraft movements for take off-landing in March 2020.

Group	Day (0700-1900)	Evening (1900-2200)	Night (2200-0700)
Airbus A321-232	2813	564	470
Airbus A350-941	438	202	281
Boeing 747-400	160	52	83
Total	3411	818	834

Table 5. Standard Noise Abatement Departure Procedures

ICAO A or NADP 1	ICAO B or NADP 2
Take off Max TO Power	Take off at Max TO Power
Climb at constant speed to 457.2 m (1500 ft) AFE	Climb to 304.8 m (1000 ft) AFE and pitch-over to accelerate at full power to clean configuration
Reduce thrust to Climb Power	At clean configuration, cutback to climb power
Climb at constant speed to 914.4 m (3000 ft)	Climb at constant speed to 914.4 m (3000 ft)

Based on the above criteria, the aircraft operated at Tan Son Nhat International airport in March 2020 are classified. After grouping the whole aircraft with similar noise characteristics into groups, an aircraft representative with the highest movement frequency during the research time will be selected to represent.

The aircraft group C* has a relatively similar geometry characteristic to the aircraft group C. However, these aircraft were separated into a new group to account for the difference between the new generation engine NEO/NEO X and the old one CEO of Airbus A320 Family aircraft. These types of engines, NEO and NEO X, are significantly improved and reduced in noise compared to conventional engines CEO used on Airbus A320 family aircraft. Moreover, the ANP database does not provide specific noise and performance information for Airbus A320 family aircraft using NEO and NEO X engines. An alternative way is to use the information of Airbus A321-232 aircraft using CFM engines for those using NEO and NEO X engines and add the following amount of take-off adjustment as described below:

$$N_{dep\_C} = 0.43 \cdot N_{dep\_C*} \quad (1)$$

Where N_{dep_C} and $N_{dep\_C^*}$ is the number of aircraft group C and C* movements, respectively. The aircraft groups are reduced to three groups. The nominal weights of each representative aircraft used for flight profile computing are selected based on the Aircraft Noise Performance database in Table 3.

Table 4 above shows the number of take-off movements for each aircraft group per aircraft representative operating at Tan Son Nhat International airport during the time of a day:

2.5 Flight path analysis and flight profile calculation

The International Civil Aviation Organization has assisted in developing and standardizing the low noise operational procedures for both take-off and landing in terms of the stepped departure and stepped approach procedures to achieve the noise reduction purpose in the vicinity of the airports. In the scope of this research, the noise abatement departure procedures are mainly focused on analyzing to compute the noise levels. The flight path of each representative aircraft was analyzed and calculated with the assumption that aircraft take-off following the NADP 1 and NADP 2. The detailed noise abatement departure procedural steps are described in Table 5, including some target points that the aircraft must be respected to reduce the noise levels in the vicinity of the airport.

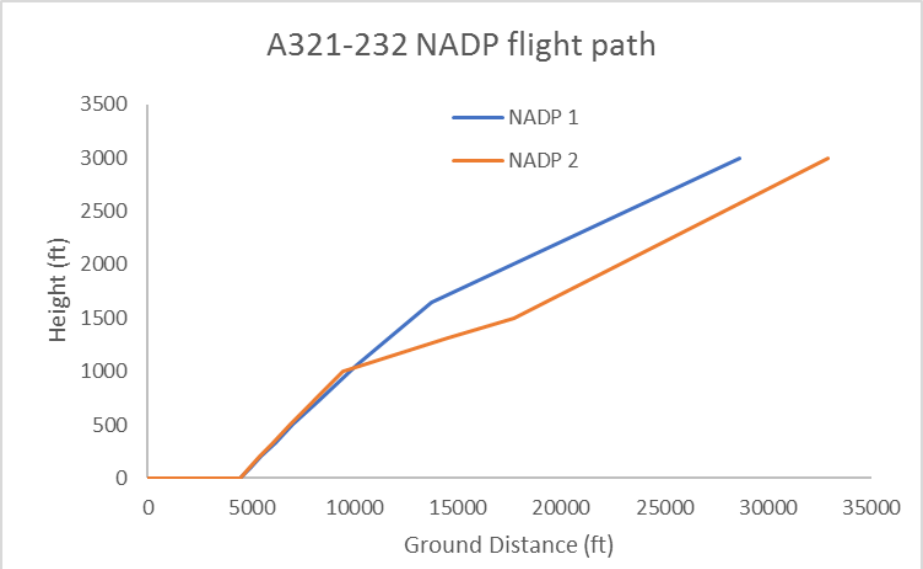

Fig. 6. The computed NADP 1 and NADP 2 flight path of Airbus 321-232

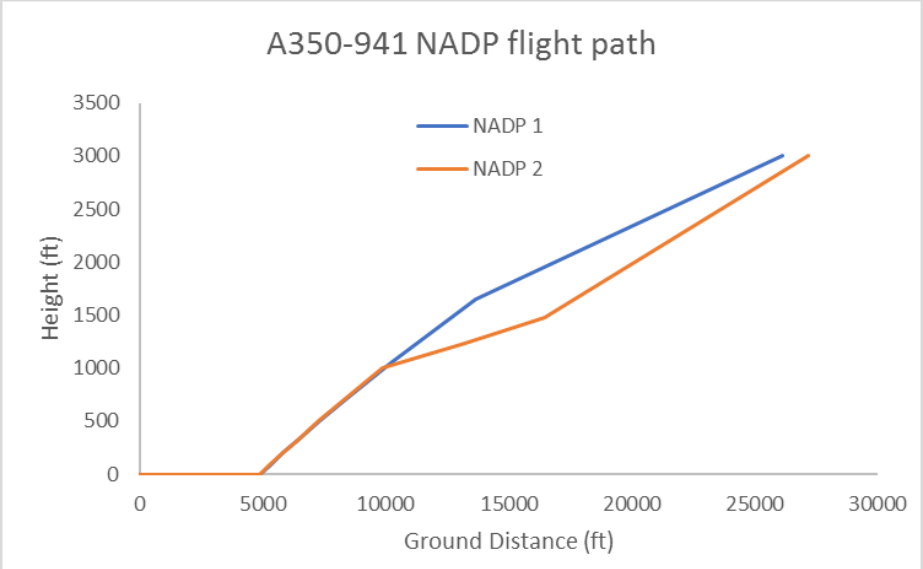

Fig. 7. The computed NADP 1 and NADP 2 flight path of Airbus 350-941

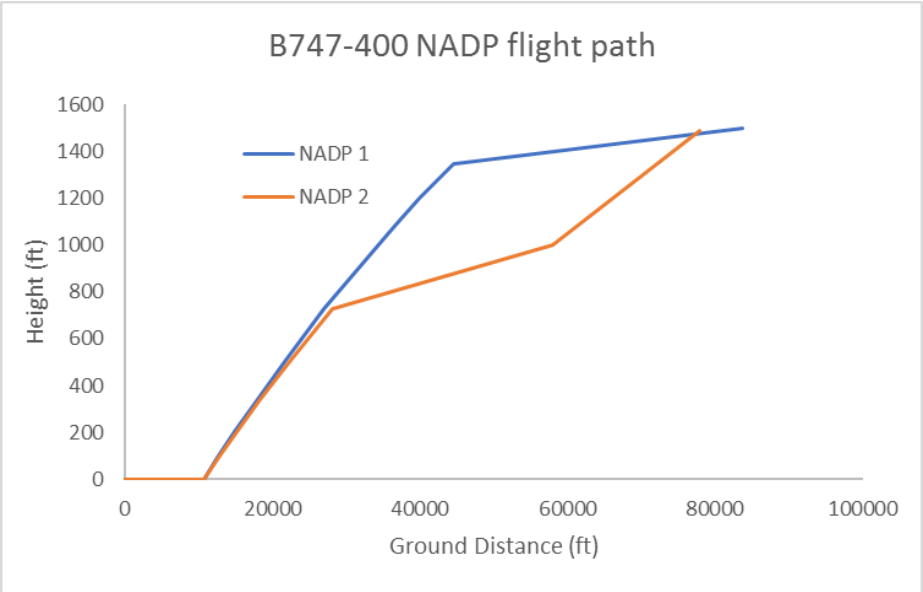

Fig. 8. The computed NADP 1 and NADP 2 flight path of Boeing 747-400

The flight mechanics equations were used to compute the performance of the representative aircraft operating at Tan Son Nhat International airport during the time of research to achieve the flight paths of aircraft flying with noise reduction procedures or so-called NADP 1 and NADP 2 flight paths. These steps were done using the flight mechanics equations for noise computation purposes supposed in the SAE-AIR-1845. These equations are used for computing the engine thrust, take-off ground roll, landing ground roll, speeds, and height of each stage of the flight path. It contains some constants coefficients that can be collected from the ANP database.

The following figures show the computed NADP 1 and NADP 2 flight paths for each representative aircraft, including Airbus A321-232, Airbus A350-941, and Boeing 747-400

After obtaining the flight path and flight profile at each target point in the noise abatement procedural step, the flight path of each representative aircraft is divided into sub-segments, such as the velocity at two adjacent segments not exceeding 10.3 m/s (20 kt). Then the flight profile will be recalculated for the start and the end of each sub-segment. The essential parameters consist of engine thrust, aircraft's velocity, height of each sub-segment, and the nearest distance, so-called the slant distance- the nearest distance between the sub-segment and the noise receiver point or the noise grid was also calculated through the geometry relationship. Depending upon the location of the noise grid and the sub-segment, these mentioned parameters are precisely determined with the method described in

The flight mechanics equations were used to compute the performance of the representative aircraft operating at Tan Son Nhat International airport during the time of research to achieve the flight paths of aircraft flying with noise reduction procedures or so-called NADP 1 and NADP 2 flight paths. These steps were done using the flight mechanics equations for noise computation purposes supposed in the SAE-AIR-1845. These equations are used for computing the engine thrust, take-off ground roll, landing ground roll, speeds, and height of each stage of the flight path. It contains some constants coefficients that can be collected from the ANP database. The following figures show the computed NADP 1 and NADP 2 flight paths for each representative aircraft, including Airbus A321-232, Airbus A350-941, and Boeing 747-400.

Document 9911 given by ICAO. Figure 9 below presents the geometry relationship between the sub-segment and the noise grid in terms of some parameters. In the departure stage, there are two separate steps that the aircraft must follow, including the take-off ground roll stage, where aircraft accelerate from the start of roll point in the RWY 25L to the take-off velocity, and the airborne stage begins at the time the aircraft lifting off. Considering a sub-segment, this can be three different possible locations of the noise grid related to the sub-segment, including behind, alongside, and ahead.

Figure 9 shows an example of the relationship between a sub-segment defined from start-point 1 to end-point 2 and a noise receiver point or noise grid. In this case, the noise grid is alongside the sub-segment, then some

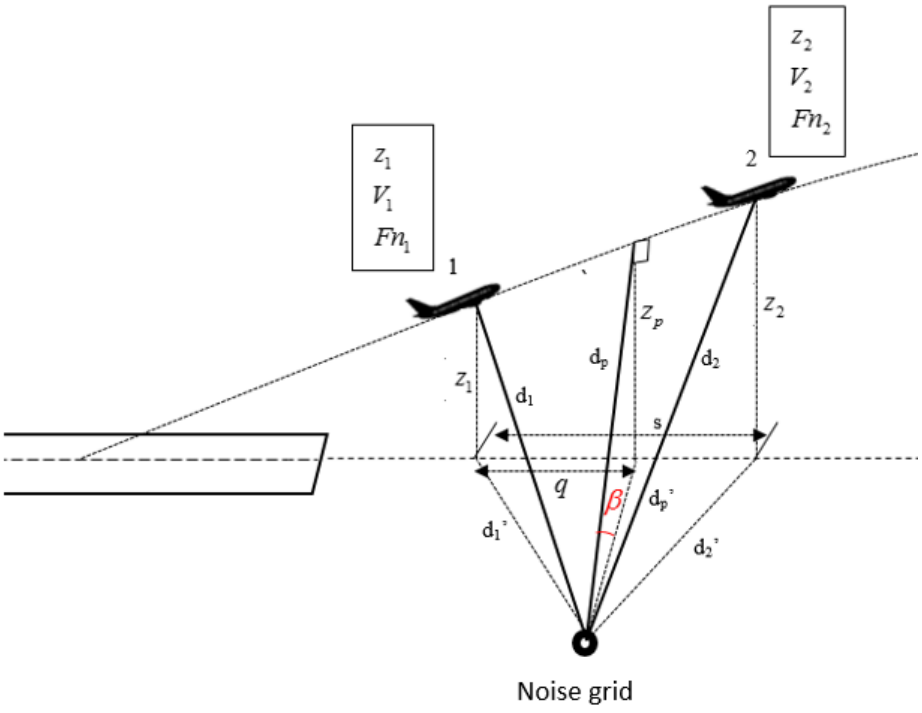

Fig. 9. The geometry relationship between sub-segment and noise grid

parameters must be determined to compute the noise exposure level received at the noise grid. These parameters include the slant distance d_P (which is laid on the sub-segment when the noise grid is alongside the segment or laid on the extended line of the segment when the noise grid is ahead or behind the segment), the height at the intersection between the slant distance and the segment z_P, the length of the segment in the ground track s, the length q from the start-point 1 and the nearest distance from the noise grid to the ground track $d_P{}'$ and the angle β between the slant distance d_P and $d_P{}'$.

2.6 Noise calculation

For evaluating aircraft noise levels around the airports, two metrics are used in this research complied with the guidance of the Civil Aviation Authority of Vietnam, including A-weighted single sound exposure level (SEL or L_E) and A-weighted equivalent continuous day-evening-night sound level (L_{den}). The NPD table is used the slant distance and the engine thrust obtained as described in the section 2.2 to extract the noise exposure level generated by each sub-segment to the ground. Due to the NPD table providing the noise levels for a particular combination of slant distance and engine thrust, the computed values are rarely available in the NPD table. Therefore, the interpolation or extrapolation formula must be used to obtain the noise exposure level for the computed values. These steps are done through the following formula:

The noise level at engine power P1 and distance d is given by

$$L_{P1,d} = L_{P1,d1} + \frac{(L_{P1,d2} - L_{P1,d1}) \cdot [log_{10}(d) - log_{10}(d_1)]}{[log_{10}(d_2) - log_{10}(d_1)]} \quad (2)$$

The noise level at engine power P2 and distance d is given by

$$L_{P2,d} = L_{P2,d1} + \frac{(L_{P2,d2} - L_{P2,d1}) \cdot [log_{10}(d) - log_{10}(d_1)]}{[log_{10}(d_2) - log_{10}(d_1)]} \quad (3)$$

And finally, the interpolated or extrapolated noise level at engine power P and distance d is given by

$$L_{P,d} = L_{P1,d} + \frac{(L_{P2,d} - L_{P1,d}) \cdot [log_{10}(d) - log_{10}(d_1)]}{(P_2 - P_1)} \quad (4)$$

Where the $P1, P2$ are the engine thrusts which its noise data included in the NPD table, $d1, d2$ are the slant distances which its noise data included in the NPD table. As mentioned in section 2.2, the NPD table is established by noise field measurement with strict conditions. These reference conditions can be found in Document 9911 of the ICAO, and the flight path the aircraft must be followed to conduct noise measurement on the ground is called the NPD flight path. The principle of noise calculation in this Section considers each sub-segment part of an NPD flight path, then uses the NPD table with two input values consisting of slant distance and engine thrust to obtain the NPD noise exposure level. The noise level contributed by each sub-segment to each noise receiver point after being interpolated or extrapolated from the NPD table will be adjusted to account for the difference between the actual flight path and the NPD flight path. The contribution from one flight path segment to noise exposure level can be expressed as:

$$L_{E,seg} = L_{E,NPD}(P,d) + \Delta_V + \Delta_I(\phi) - \Lambda(\beta,l) + \Delta_F \quad (5)$$

where $L_{E,NPD}(P,d)$ is the noise exposure level at engine thrust P and slant distance d obtained in the NPD table; $\Delta_V, \Delta_I(\phi), \Lambda(\beta,l), \Delta_F$ are called "correction terms" to account for the effect of duration, installation, lateral attenuation, and segment correction, respectively. The formulas to compute these correction terms can be found in Document 9911 published by ICAO.

Calculation of single event noise exposure level LE or SEL

The $L_{E,seg}$ computed in the previous section is the noise exposure level created by a single sub-segment to the noise grid. The single event noise exposure levels generated by a representative aircraft flying in a specific flight path or a particular set of continuous sub-segments were calculated by summing all the noise exposure levels of each sub-segment using the following formula:

$$L_E = 10 \cdot log\left(\sum_i^j 10^{\frac{L_{E,i}}{10}}\right) \quad (6)$$

where $L_{E,i}$ is the noise exposure level caused by sub-segment i^{th}

Calculation of day-evening-night cummulative noise level L_{den}

It is necessary to account for all aircraft movements during the day, evening, and night intervals to evaluate comprehensively the noise level generated by aircraft operating, as listed in Table 4. The cumulative noise levels or the equivalent continuous noise levels for the day, evening, and night intervals describes the cumulative noise exposure from all events over 24 hours a day and are calculated as follows:

$$L_{eq} = 10 \cdot log\left[\frac{1}{T}\left(n_C \cdot 10^{\frac{L_{AE,C}}{10}} + n_D \cdot 10^{\frac{L_{AE,D}}{10}} + n_E \cdot 10^{\frac{L_{AE,E}}{10}}\right)\right] \quad (7)$$

Where n_C, n_D, n_E are the number of aircraft movements of each group respectively; L_{eq} will become L_{day}, $L_{evening}$, and L_{night} with T being the time interval such as day-time (12 hrs), evening-time (3 hrs), and night-time (9 hrs), respectively. The day-evening-night equivalent noise level L_{den} is then calculated based on L_{day}, $L_{evening}$, and L_{night} by the following equation:

$$L_{den} = 10 \cdot log\left[\frac{1}{24}\left(12 \cdot 10^{\frac{L_{day}}{10}} + 3 \cdot 10^{\frac{(L_{evening}+5)}{10}} + 9 \cdot 10^{\frac{(L_{night}+10)}{10}}\right)\right] \quad (8)$$

The evening and night time are weighted 5 dB and 10 dB respectively to account for background noise reduction during these periods. Therefore the noise levels created by aircraft movement will be felt more apparent than during the day-time when the background noise is relatively higher. Finally, the noise contour maps for day-evening-night equivalent continuous noise levels were established by interpolating the value of all noise receiver points inside the computing domain around Tan Son Nhat International airport.

3. Results and Discussion

Figures 10 to 12 below show the noise contours for single event noise exposure levels generated by each representative aircraft Airbus 321-232, Airbus 350-941, and Boeing 747-400 flying out of the Tan Son Nhat International airport following the noise abatement departure procedures NADP 1 and NADP 2, respectively.

The computed noise contours using (Eq 5) and (Eq 6) described in the previous section result in noise exposure levels ranging from 85 dB(A) to 65 dB(A) around the Tan Son Nhat International airport for NADP 1 and NADP 2. The difference between the noise contours shape of representative aircraft is due to the difference in the performance of each aircraft in the specific phase of departure, such as take-off ground roll and initial climb. With the variation in the number of movements during the day-time, evening-time, and night-time, the cumulative noise continuous level must be computed to comprehensively evaluate the extent and effect of noise generated by aircraft movements to the ground. This cumulative noise is computed in terms of day-evening-night noise exposure levels using (Eq 7) and (Eq 8), as shown in the figures below

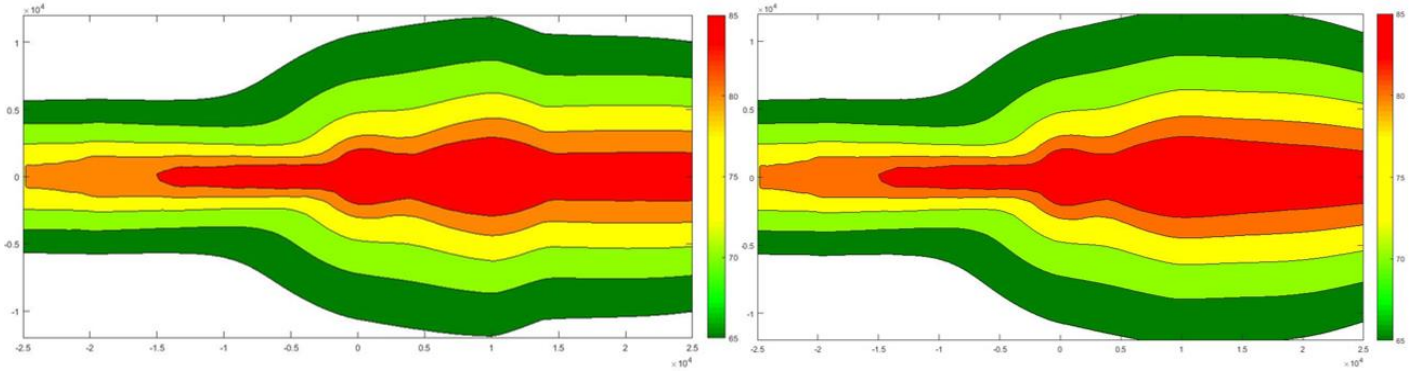

Fig. 10. Noise contours for Airbus 321-232 movements following NADP 1 (left) and NADP 2 (right)

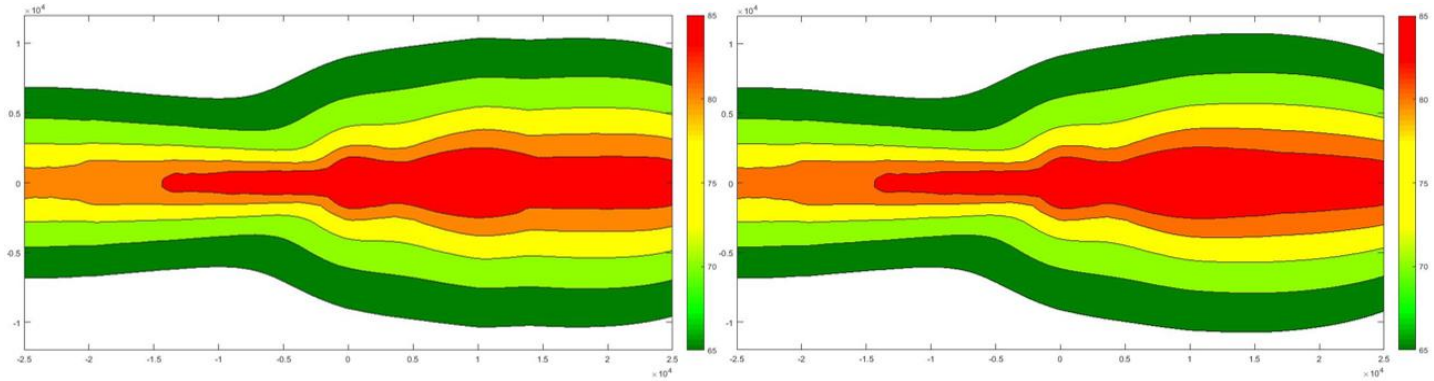

Fig. 11. Noise contours for Airbus 350-941 movements following NADP 1 (left) and NADP 2 (right)

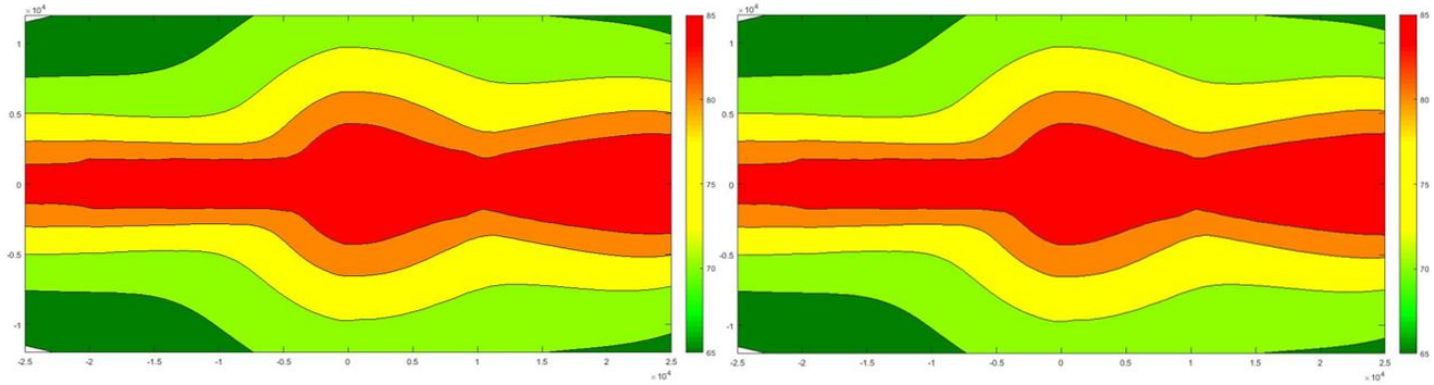

Fig. 12. Noise contours for Boeing 747-400 movements following NADP 1 (left) and NADP 2 (right)

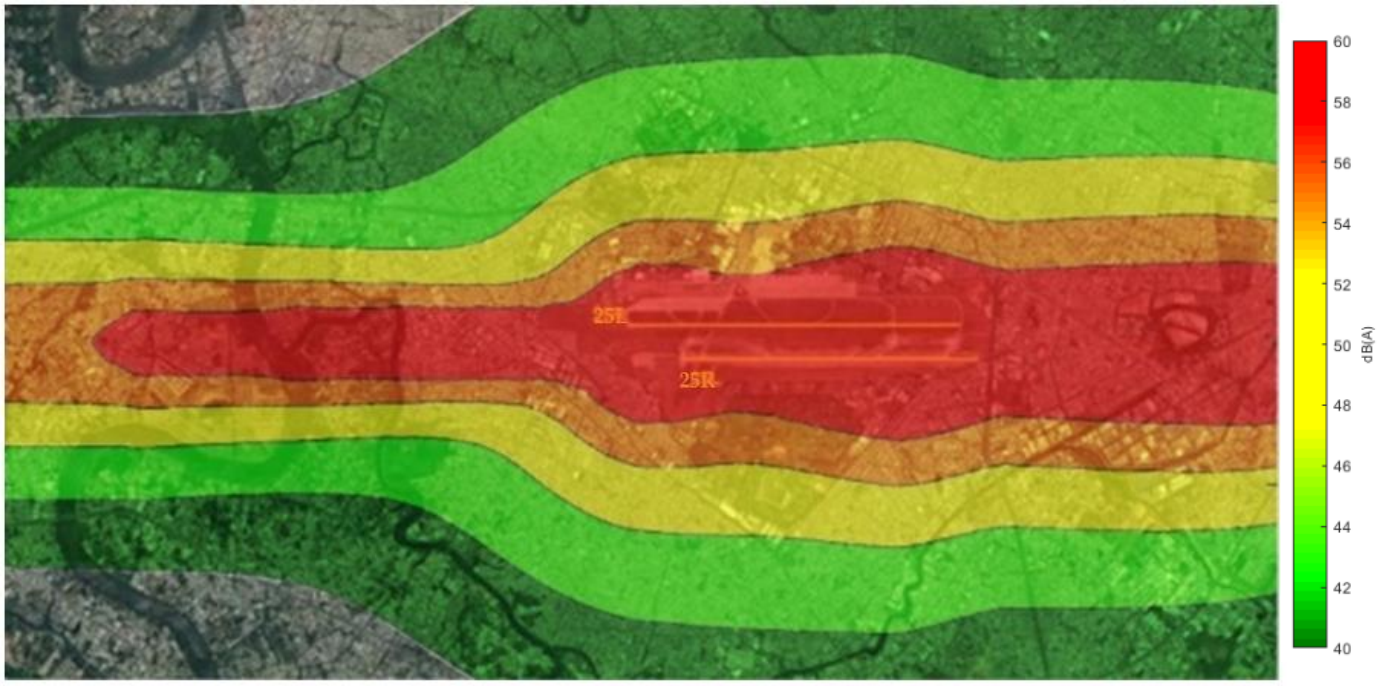

Fig. 13. The L_{den} noise contours map for aircraft movements following NADP 1 (cumulative noise exposure from all events over 24 hours).

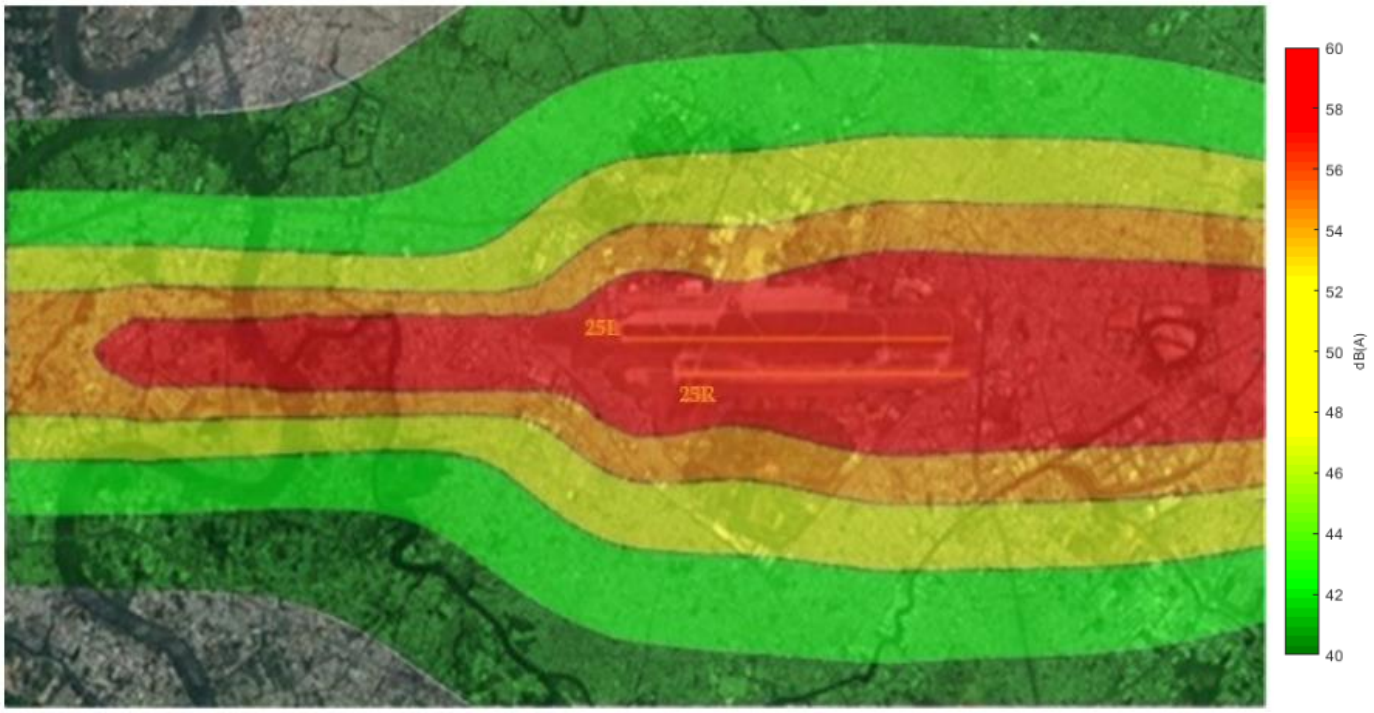

Fig. 14. The L_{den} noise contours map for aircraft movements following NADP 2 (cumulative noise exposure from all events over 24 hours).

The highest simulated day-evening-night equivalent noise levels in the noise contours for both procedures are 60 dB(A) which occurs in the region nearest the ground track – parallel to the runway and directly beneath the flight path – and gradually decreases in the area far from the airport. These results are consistent with the natural characteristics of noise generated by aircraft movements when the noise levels are related to the slant distance between noise sources and noise receivers and aircraft engine thrust. The following figure expresses noise contour lines for aircraft movements following flight procedures NADP 1 and NADP 2 around Tan Son Nhat International airport in the exact figure.

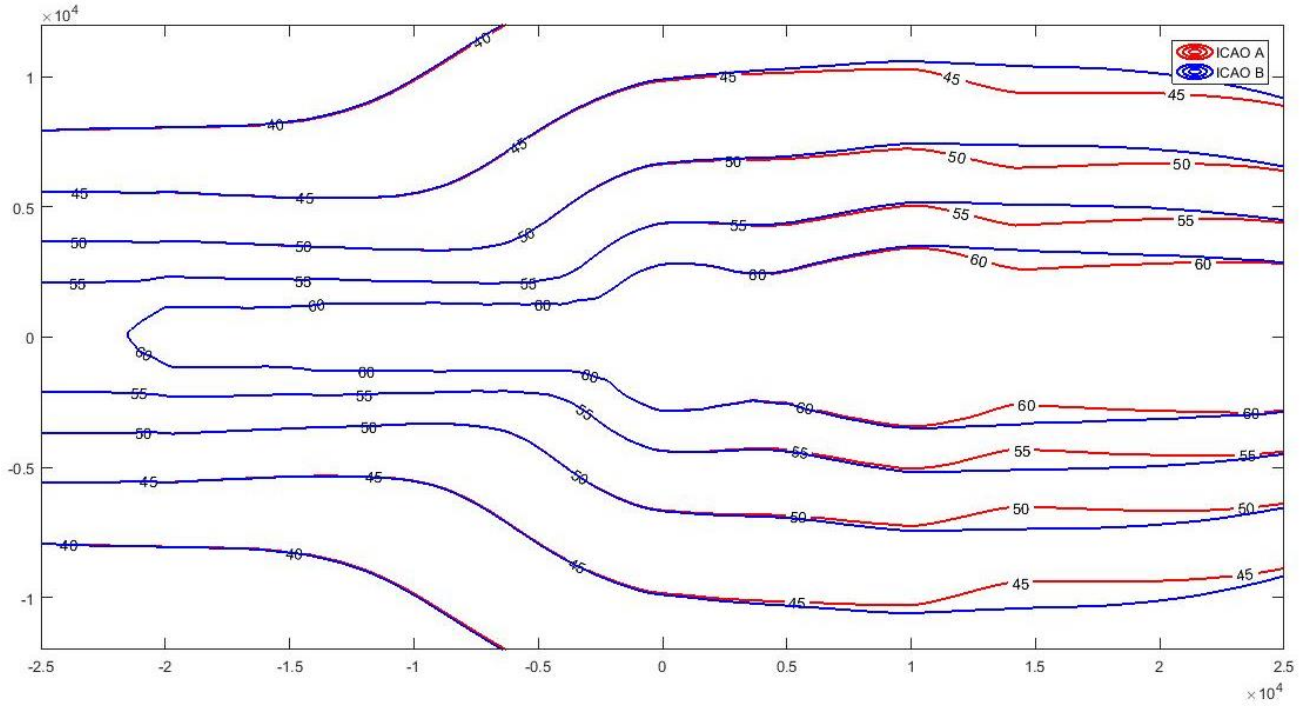

Fig. 15. The L_{den} noise contours line for aircraft movement following NADP 1 and NADP 2 (or ICAO A and ICAO B).

4. Conclusions

This research has successfully simulated the noise contour maps assuming that aircraft depart from the Tan Son Nhat International airport following the noise abatement departure procedure 1 and 2. The results show that noise levels range from 40 dB(A) to 60 dB(A), with the significant difference between the two procedures occurring at the end of the runway when the aircraft begins to lift off and conduct the initial climb phase. That is because those aircraft following the NADP 1 must climb as fast as possible to 914.4 m (3000 ft), and thus, the contour lines of the departure area will be slightly narrower than the NADP 2 when the aircraft fly far away from the runway. The results have presented that if the noise abatement departure procedures are applied in daily aircraft operation, the day-evening-night exposure levels around the airport generated by aircraft taking off around the Tan Son Nhat International will range from 40 dB(A) to 60 dB(A), which is an acceptable level that does not risk harming human health demonstrated by numerous research studies. The established noise maps are the basis for effectively assessing the noise levels at Tan Son Nhat International airport for the authority, thereby providing solutions for rational land use planning in the affected area by high noise levels. Moreover, it also aids the authorities in issuing regulations on noise level limits and aiming to develop noise contour maps for all major airports in Vietnam. As a matter of fact, adopting noise-reduced take-off procedures is a small part of the effort to prevent noise pollution around airports, and it also requires meticulous study to ensure that safety is prioritized. Each noise reduction procedure has its advantages and disadvantages; therefore, to select the appropriate noise abatement procedure to apply for the specific airport, it is necessary to thoroughly consider the situation and the extent of the noise-sensitive area around the airport. These steps can only be completed in partnership between researchers, aviation authorities, and airlines. In further studies, it is necessary to study the combination of different noise reduction measures that suit the actual conditions at the airport as suggested by ICAO in order to get better noise reduction effects. The results of this study can also be integrated into the geographic information system (GIS) to assess the number of affected populations in the high noise levels areas at the departure zone of the Tan Son Nhat airport.

Nomenclature

ADS-B : Automatic Dependent Surveillance-Broadcast
AIP : Aeronautical Information Publication
AIR : Aerospace Information Report
ANP : Aircraft Noise Performance
ECAC : European Civil Aviation Conference
GIS : Geographic Information System
ICAO : International Civil Aviation Organization
NADP : Noise Abatement Departure Procedure
NDP : Noise-Power-Distance
RWY : Runway
SAE : Society of Automobile Engineers

References

Civil Aviation Authority of Vietnam, 2019. Guidance manual for the monitoring and evaluation of aircraft noise around airports in Vietnam. Ministry of Transport & Civil Aviation Authority of Vietnam.

Civil Aviation Authority of Vietnam, Aeronautical Information Publications (AIP), 2021, available at: https://vnaic.vn/ (assessed on 12 Dec 2021).

EUROCONTROL, The Aircraft Noise and Performance (ANP) Database, 2021, available at: https://www.aircraftnoisemodel.org/data/table (assessed on 15 Nov 2021).

European Aviation Safety Agency, available at: https://www.easa.europa.eu/eaer/appendix (assessed on 15 Nov 2021).

European Civil Aviation Conference, 2005. Methodology for computing noise contours around civil airports.

European Civil Aviation Conference, 2005. Report on standard method of computing noise contours around civil airports.

Federal Aviation Administration, 1985. Aviation noise effects.

Federal Aviation Administration, 2017. Aviation Environmental Design Tool (AEDT) – Technical Manual Version 2d.

Ha, C.H, Dang, N.P, Son, M.T & Dung, P.H, 2009. Investigation, survey, assessment of the current situation of air pollution, noise; building noise map and minimize solutions for Tan Son Nhat international airport. Ministry of Transport of Vietnam.

Halil, Y.A, Mehmet, Z.G & Onder, T, 2020. Assessment of Aircraft Noise Emissions at International Eskisehir Hasan Polatkan Airport with Multiple Approach Model. Journal of Aerospace Technology and Management, vm13.

International Civil Aviation Organization, 2008. Recommended method for computing noise contours around airports.

International Civil Aviation Organization, 2011. Environment protect.

International Standard Organization, 2009. Acoustics - Unattended monitoring of aircraft sound in the vicinity of airports.

Kiet, L.T, 2020, Process of computing and constructing noise contours maps around Tan Son Nhat International Airport, Unpublished Bachelor's thesis, Ho Chi Minh City University of Technology, Vietnam.

Lan, N. T., Takashi, Y., Ichiro, Y. & Makoto, M, 2016, Noise contours around Noi Bai International Airport - change in aircraft noise exposure before and after the opening of the new terminal building. Inter-Noise 2016, Hamburg, pp.822-832.

Lan, N.T, Yano, T, Huy, Q.N & Nishimura, T, 2011. Community response to aircraft noise in Ho Chi Minh City and Hanoi. Applied Acoustics, vm72(is11), pp.814-822.

Ledoux, H & Gold, C, 2005, An efficient natural neighbour interpolation algorithm for geoscientific modelling, Developments in Spatial Data Handling, Springer, Zurich, Switzerland, pp.97-108.

Lien, T.B, Lan, N.T & Morihara, T, 2019, Assessment of health effects of aircraft noise on residents living around Noi Bai International Airport, Inter-noise 2019, Madrid, pp.4973-4982.

Lien, T.B, Lan, N.T & Morihara, T, 2021. How Does a Community Respond to Changes in Aircraft Noise? A Comparison of Two Surveys Conducted 11 Years Apart in Ho Chi Minh City. International Journal of Environment Research and Public Health, vm18(is08), pp.4307.

Loc, B. T., Lan, N. T. & Lien, T.B, 2019, Comparing noise contours calculated using existing and measurement-based NPD data for two major airports in Vietnam, Inter-Noise 2019, Madrid, pp.4963-4972.

Pablo, G.M, 2012. Noise contour calculation from measured data, Unpublished Master's thesis, Technical University of Lisbon, Portugal.

Pertiwi, A, Haryono S.H, Diny, S & Wiwik, B, 2018. Development of Airport Noise Mapping using Matlab Software (Case Study: Adi Soemarmo Airport – Boyolali, Indonesia), The 2nd International Conference on Energy, Environmental and Information System (ICENIS 2017).

Sibson, R, (1981). A brief description of nearest neighbor interpolation, interpolating multivariate data. New York: John Wiley & Sons.

Society of Automotive Engineers, 1975. Standard values of atmospheric absorption as a function of temperature and humidity. SAE International.

Society of Automotive Engineers, 1986. Procedure for the calculation of aircraft noise in the vicinity of airports. Michigan. SAE International.

Tan Son Nhat International Airport, 2021, available at: https://tansonnhatairport.vn (accessed on September 24, 2021).

Tan, Q. & Xu, X, 2014. Comparative analysis of spatial

interpolation methods: an experimental study. Sensors & Transducers Journal, vm18, pp.155-163.

Tuan, L.D, Anh, T.T & Hai, N, 2019. On the airport environmental noise monitoring and control system. Science & Technology Development Journal – Engineering and Technology, vm03(is02), pp.69-180.

Yen, P.Q & Nga, N.T.T, 2020. Experiment, evaluate methods of interpolation of terain surface for different types of terrain. Journal of Mining and Earth Sciences, vm61(is02), pp.116-125.

International Journal of Aviation Science and Technology

Research Article

Aircraft Noise Compatibility of the Airports with Progress of Noise Reduction at Source

Oleksandr Zaporozhets[1]*, Kateryna Kazhan[2], Kateryna Synylo[3], Sergii Karpenko[4]

[1]National Aviation University, Kyiv, Ukraine
zap@nau.edu.ua- 0000-0002-7580-0921
[2]National Aviation University, Kyiv, Ukraine
kazhan@gmail.com- 0000-0002-5668-9965
[3]National Aviation University, Kyiv, Ukraine
synylo@nau.edu.ua- 0000-0003-1333-0351
[4]National Aviation University, Kyiv, Ukraine
karpenko_serg@ukr.net- 0000-0003-2114-2377

Abstract

Creation of noise exposure maps and airport noise compatibility programs are the basic steps in aircraft noise exposure and impact management in/around the airports, both of them are fundamental for aircraft noise zoning procedures. Noise reduction at source is also a strategic element of this management, and efficient implementation of quieter aircraft designs in operation provides closer distances of the boundaries of noise zones prohibited for residences to runway axis. These new conditions oblige the decision-makers, responsible for noise management, to be stricter with procedures for noise zones definition and to include in consideration a number of new acoustic sources inside the aerodrome besides the aircraft in flight operation, which may influence the overall exposure and impact of noise on population living or/and acting around the airport. In other words, current noise exposure maps and airport noise compatibility programs must include these dominant noise sources at specific locations of the airport also, not only the flight noise sources, as it was enough before. Today such essential noise sources for consideration in airport noise management are the aircraft in maintenance and overhaul and the aircraft during the taxing between the runway and stands on apron first of all, especially if their locations are quite far from aircraft flight operation routes and close to the residential areas around the aerodrome. The noise maps are required to be calculated currently, as for aircraft operation, so as for their maintenance and overhaul, but the measurements are evident also for their confidence and accuracy purposes.

Keywords

Aircraft Noise,
Zonning,
Reduction at Source,
Compatibility,
Measurements,
Calculations

Time Scale of Article

Received 5 May 2022
Revised until 19 August 2022
Accepted 18 September 2022
Online date 29 December 2022

1. Introduction

There are many environmental problems at airports today resulting directly from poor or still non-existent planning for compatible land use. In best cases the national regulation for environment protection requires airports the creation of Noise Exposure Maps (NEMs) and Airport Noise Compatibility Programs and/or Planning (ANCP). For example, in the USA the ANCP was launched by the Aviation Safety and Noise Abatement Act of 1979 (H.R.3547c, 1979) and is currently required by

*: Corresponding Author Oleksandr Zaporozhets zap@nau.edu.ua
DOI: 10.23890/IJAST.vm03is02.0204

US FAA Part 150 (Part 150, 1984) as an obligatory element of the overall airport management. Part 150 is the primary federal regulation directing planning for aviation noise (AN) compatibility on and around the airports. ANCP identifies measures the airport operator has taken or proposes to take to reduce, and/or prevent the introduction of, incompatible land uses in the airport vicinity. Two principle preventions for airports are taken in mind - direct environment protection from the dominant impacting factors and the operational capacity support of the airport at the maximum level.

Noncompatible land use means the use of land that is identified as normally not compatible with the outdoor noise environment. Sanitary norms are the ground for limiting the noise in accordance with activity provided inside the area (at a point) of consideration. Part 150 established the yearly day-night average sound level (DNL or L_{DN}) to be used for AN assessment and defined under Appendix A the appropriate limits for human activities in the vicinity of airports being compatible with them. In general case the ANCP should be addressed on following main activities from the airport with essential contribution of calculated NEMs for assessment of the effect: to reduce existing and forecasted AN levels over existing noise-sensitive land uses; to reduce new noise-sensitive developments near the airport; to mitigate adverse impacts in accordance with federal guidelines (sanitary norms should be used for assessment); to provide mitigation measures that are sensitive to the needs of the community and its stability; and to be consistent with local land use planning and development policies. Feasibility and economic efficiency should be also taken in mind - not only the environmental issues.

Compatibility and consistency of airport activities are defined by AN limits for population health protection in dependence to their activity inside specific AN zones (ANZ) and for defining ANZ boundaries. The boundaries of the ANZ are defined due to calculated NEM, usually in accordance with internationally approved approach/guideline. For AN such an approach is prescribed in the SAE Standard AIR 1845 (SAE AIR1845A, 2012) and in the guideline ICAO Doc 9911 (ICAO Doc 9911, 2018) or its ECAC analogues Doc 29 (ECAC Doc 29, 2016). Calculated L_{DN} = 65 dBA is still identified as the threshold of significant AN exposure as well as incompatible with residential land use. Inside every predefined zone the noise-sensitive land use should be prevented. Any new development inside the ANZ with $L_{DN} \geq 65$ dBA is prohibited, the existent residential and/or administrative areas must be protected if possible, if not – replaced out of the ANZ.

In Europe the recent study of noise exposure level and noise mitigation strategies at six quite different airports (Frankfurt, Heathrow, Zurich, Madrid, Barcelona, and Malaga) during the decade 2003-2013 has been shown by (G.Alonso, A.Benito, L.Boto, 2017). The study provided an overview of the current noise regulations and of noise measures applied by the different airports which main goal to enforce a more stringent noise level limit to ensure that the latest noise reduction technology is incorporated into the aircraft design. According to this study, the average daily noise reduction was possible mainly due to the development of new aircraft technologies focusing on noise reduction at source and consequently on the fleet renewal performed by airlines in the last decades. However, there is still a long way to go as the resident complains have not stopped since the noise pollution is still bothering people mainly at night time.

Aircraft noise exposure calculations need to be highly accurate due to their impact on land-use planning (Meister J., Schalcher S., Wunderli J.-M., Jäger D., Zellmann C., Schäffer B., 2021). Calculation uncertainties strongly depend on the modelling approach, model sophistication, traffic input data, available sound source data and airport peculiarities such as specific aircraft fleet or different flight procedures. In the past, model validations were conducted for different models such as ANCON in the United Kingdom (Rhodes D., Ollerhead J., 2001), and FLULA2 (Buetikofer, R.; Thomann G., 2001) and sonAIR (Jäger D. , Zellmann C., Schlatter F., Wunderli J.-M., 2020) in Switzerland. Studies which compare different noise models together and against measurements are not available. Both, FLULA2 and AEDT, are best practice programs, primarily developed to calculate complex scenarios such as yearly air traffic operations, which include various aircraft types and large numbers of flights. All of them are still not consider as dominant, at least in some locations of the airport, another noise sources except aircraft in flight.

In line with the European Directive 2002/49/EC the Turkish Regulation on Assessment and Management of Environmental Noise (RAMEN) implemented the maximum allowable limit for noise is L_{den} = 63 dB (A) (Akdeniz H., Sogut Z., Turan O. 2021). Due to RAMEN aircraft-induced noise should be evaluated under four main headings including the noise generated during maintenance of the aircraft on the ground. But still the Noise Exposure Mapping at the airport (International Eskisehir Hasan Polatkan Airport, LTBY, was assessed as an example) is realized for flight traffic only – without the contribution of all other dominant noise sources in airport.

In Ukraine the similar system was introduced as it was shown in (Konovalova O., Zaporozhets O., 2021): the rules (SSR-173, 1996) define the ANZ around the airports (aerodromes), the aviation rules (SAAU AR-381, 2019) require to use the DENL (European analogue of the DNL) for ANZ boundaries calculations and proving them by noise measurements in accordance with methodology of

(SAAU Order 585, 2020). The rules (SSR-173, 1996) still consider equivalent sound levels L_{Aeq} and maximum sound levels L_{Amax} as the criteria for noise zoning also (Konovalova O., Zaporozhets O., 2021), which may even confuse the decision-makers, responsible for noise zoning both in airport authority and in urban administration.

ICAO also proposed Balanced Approach to AN management in airports (ICAO Doc 9829, 2004), consisting of 4 main elements – ANZ and compatible land usage is among them. It is of the same strategic importance as a reduction of noise at source by designing the aircraft quieter in accordance with ICAO Standards requirements (ICAO Annex 16, 2019). The evident success during last decades in designing and implementation quieter aircraft provides new circumstances for ANZ and compatible land usage around the airports.

Communities commonly construe aircraft noise regulatory policy as intended to protect airport operations from limitations imposed to reduce community impacts, while airport managements tend to believe that airport noise policy favours consideration of community more than airport interests. AN compatibility of the airport may be considered as broken if the ANZ are defined by calculation of flight AN exposure only. A long-term balance between satisfying public demand for air transportation services on the one hand, and for habitable residential neighborhoods near airports on the other, has proved difficult to achieve. In many cases in EU and around the world in general, intense controversies over increases in AN exposure have delayed or prevented the construction of desired additional airport capacity.

2. Calculation of Aircraft Noise at Kyiv/Zhulyany Airport

Aircraft noise has been an issue in Ukraine at almost every airport over the last four decades. Technology has improved aircraft performance capabilities and reduced its noise. Continued progress in achieving AN and land use compatibility is now focused at the airport specific level.

AN calculations are doing for every airport in Ukraine in accordance with certification rules for the aerodromes, currently these rules are defined by Aviation Rules (SAAU AR-381, 2019), previously by predecessor methods (Zaporozhets O., Tokarev V., 1998, DSTU-N B V.1.1-31, 2013). For example, for the airport Kyiv/Zhulyany first calculations in accordance with guideline (ICAO Doc 9911, 2018) were provided at the beginning of 1990s, when the fleet consisted of USSR aircraft designs completely, mostly certified with Chapter 2 requirements of the ICAO Annex 16 (Fig. 1a). The same flight traffic scenario in the 1990s, but all airplanes in a fleet complying Chapter 2 (ICAO Annex 16, 2019) requirements, have been replaced by airplanes complying with Chapter 3, produce AN exposure as shown on a map in Fig. 1b. The AN contour 65 dBA was reduced 2.5 times by this replacement, which is similar to ICAO decision to phase out the Chapter 2 aircraft in 1997-2002 from international operation.

During the decade 2001-2010 the air traffic was reduced dramatically in Ukraine for a number of reasons, a fleet consisted of Chapter 3 aircraft dominantly – these conditions provided the reduction of AN exposure up to 10 times (Fig. 1c) in comparison with real scenario 1990s (Fig. 1a). At least, last calculations were made at the end of 2011-2020 decade, traffic increased twice during the decade, so as the AN exposure (Fig. 1d). The calculated areas of the AN contours for all the analysed air traffic scenarios are shown in Tab. 1.

The prohibited for new residential and administrative developments ANZ 65 DNL for all the scenarios are compared between themselves in a Fig. 2. It must be concluded that the accuracy and adequacy of the calculation methodology for AN assessment was changing during this period, mostly in a way of AN contour reduction. For example, the calculated contours for the 1990s scenario includes very specific and very wide segments connected with noise exposure produced at starting points of the aircraft run-offs along the runways, which quickly become narrower along the run-off. This effect of noise radiation assessment in backward direction to aircraft run-off was improved in the SAE Standard AIR 1845 (SAE AIR1845A, 2012) and in the guideline (ICAO Doc 9911, 2018) at the end of 1990s and appropriate AN exposure was reduced essentially. For a number of airports with specific aerodrome layout the improvement of calculation methodology and implementation of quieter aircraft in operation provided the conditions, where and when the flight stages are not responsible for the overall AN exposure around the airports – aircraft taxing, aircraft engine run-ups, other aircraft operation and maintenance on ground surface began to contribute to AN exposure in specific directions and provided higher impact on residential areas than the aircraft in flights.

A similar situation is observed at some airports of Ukraine. For example, at the Kyiv/Zhulyany airport (Fig. 3) the apron with aircraft stands near the both terminals is located at a distance of more than 1 km from the runway axis and the contribution of noise from of aircraft taxiing and services at the stands to the total noise load on residential areas in Kyiv, especially in the North of the airport (on Povitroflotska Street, the nearest building to the aircraft stand on the apron is 400 m away, to the runway - 1500 m). In such and similar

cases, projects to assess the sound levels of airport noise should include contribution from the ground stages of the aircraft movement – taxiing and operation/services on stands (in Fig. 3a passenger aircraft stands are close to passenger terminal, business aviation stands and aircraft engine run-ups at MRO). Noise contour for L_{Aeq}=65 dBA in 1990s traffic scenario (Fig. 1a) was ~10 times larger than the same in 2010-2020 decade (Fig. 1d) and covered the area with aircraft stands and taxi ways, so it was not necessary to assess the contribution from these noise sources previously.

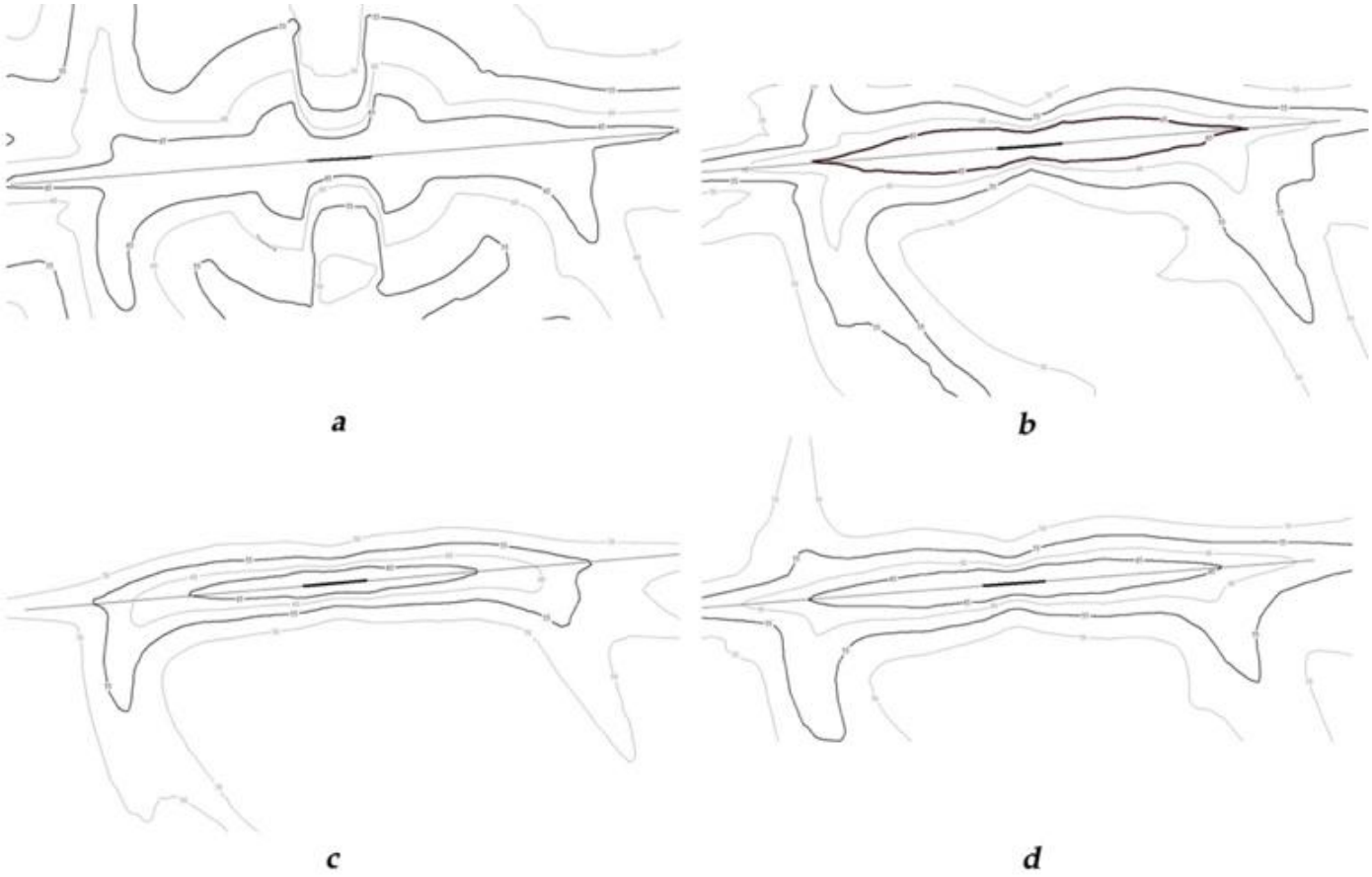

Fig. 1: AN contours for equivalent sound levels LAeq day (internal contour 65 dBA; outer contour 55 dBA) for air traffic scenarios at the airport Kyiv/Zhulyany during the daytime: a) operational scenario for 1990s; b) the same air traffic as in the 1990s, but all airplanes complying with Chapter 2 requirements have been replaced by airplanes complying with Chapter 3; c) air traffic scenario for 2001-2010 decade -- Chapter 2 aircraft are absent in the fleet; d) air traffic scenario for 2011-2020 decade - all airplanes are complying with Chapter 3 and 4 requirements (Annex 16 of ICAO, Volume 1)

Table 1 AN contour areas for equivalent sound levels $L_{Aeq\ day}$, dBA for air traffic scenarios at the airport Kyiv/Zhulyany during the daytime

$L_{Aeq\ day}$, dBA	**Contour area, m²**			
	1990s air traffic scenario, Chapter 2 aircraft	**1990s air traffic scenario, Chapter 3 aircraft**	**2001-2010 air traffic scenario**	**2011-2020 air traffic scenario**
50	4.8583E8	1.5477E8	5.2877E7	1.2138E8
55	2.2554E8	5.5186E7	2.0198E7	3.9045E7
60	7.3368E7	2.2976E7	9.6089E6	1.7348E7
65	2.5911E7	1.0265E7	3.7231E6	7.9646E6

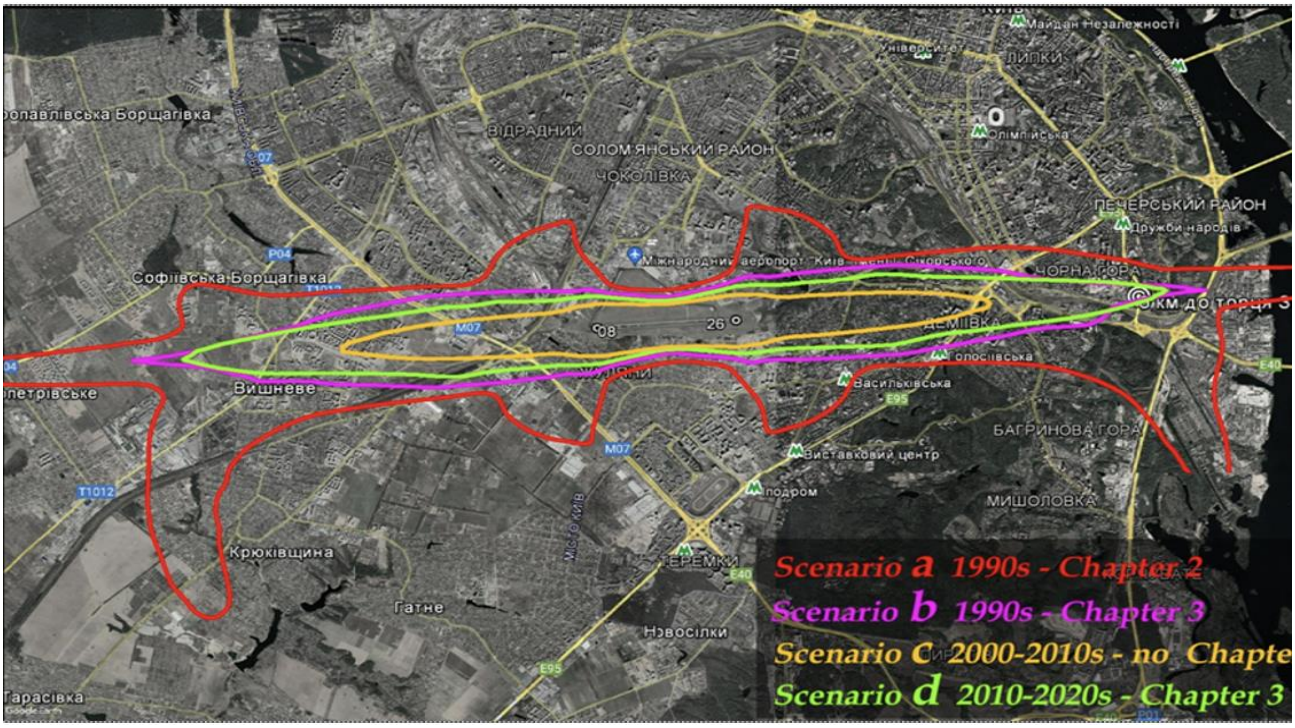

Fig. 2: Comparison of AN contours for equivalent sound levels $L_{Aeq\ day}$ = 65 dBA for the air traffic scenarios, shown in Fig. 1 between themselves

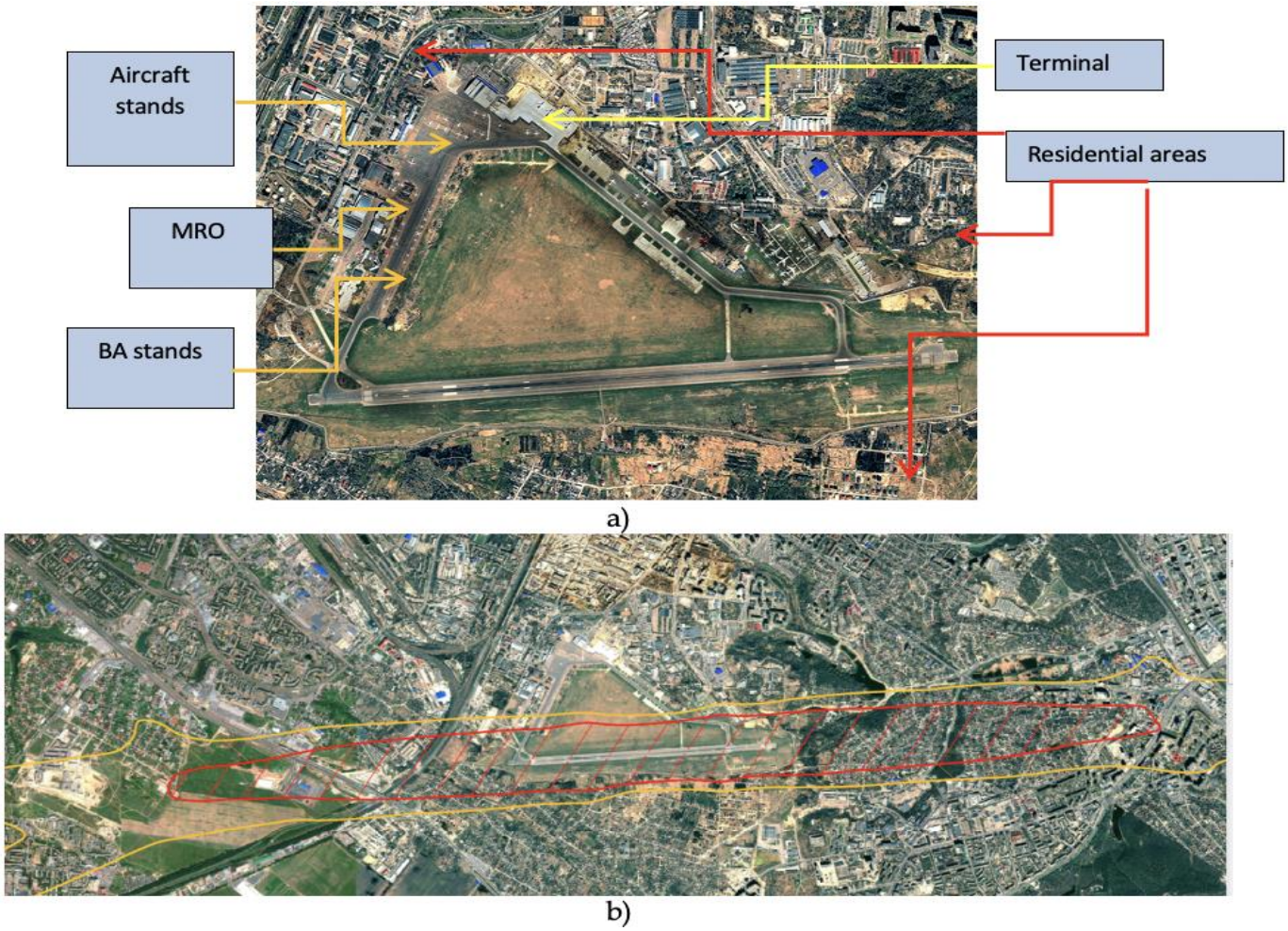

Fig. 3: Airport Kyiv/Zhulyany: a) the apron with aircraft stands near the terminal is located at a distance of more than 1 km from the runway axis; b) noise zones for 2010-2020 air traffic scenario – red contour is for Leq day=65 dBA

3. ICAO Standard Requirements to Aircraft Noise and Management of Noise Exposure Around the Airports

Today's civilian aircraft are quieter than at any time in the history of jet-powered flight. The new ICAO AN standard requirements (Annex 16 of ICAO, 2019) do not force manufactures to develop new technology. However, as new noise reduction technologies emerge, they do ensure that new aircraft continue to meet increasingly quieter standards within the bounds of what is technologically feasible and economically reasonable. As a result, for many years there was a steady decline in the number of people exposed to significant noise in communities located near airports. In recent years, however, as aviation industry growth has led to an increase in operations in many areas, the number of people and the size of the areas experiencing significant aircraft noise has started to show a gradual expansion.

The single most influential factor in that decline was the phased transition to quieter aircraft, which effectively reduced the size of the areas around airports experiencing significant noise levels. A more significant impact on AN assessment should be expected from a further reduction in noise levels at the source, when the sound levels at the control (certification) points and for the noise contours with the normative value of the sound level (eg 75 dBA $L_{Amax\ night}$) will not be displayed on the airport noise map. As can be seen from **Fig. 4** the AN contour for take-off/climbing of the aeroplane with Chapter 14 noise performances (ICAO Annex 16, 2019) is already within the runway size. The character aircraft type for each ICAO Chapter group is shown in **Tab. 2**. For the shown spectral classes the class 101 includes dominance of jet noise in low frequency bands if to compare with classes 103 and 104. Therefore, further expected more stringent requirements for AN levels at three points of noise control (take-off, climbing and descending before landing) will create conditions where the noise contours for single departure and arrival events will be indeterminate for exposure assessments with essential noise levels (correspondent to environmental noise limits) and decision-making in the airport noise control program.

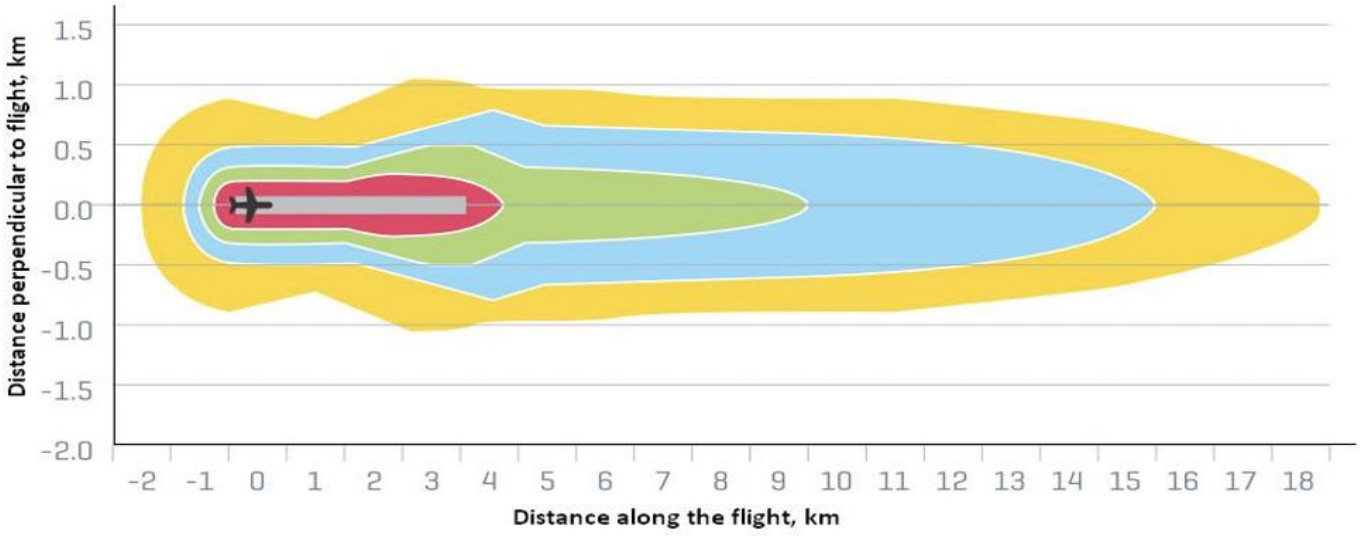

Fig. 4: An footprint (single aircraft departure contour for SEL=80dBA) reduction during last 50 years from ICAO Annex 16 Chapter 2 till Chapter 14 certification norms: in yellow – Chapter 2; in blue – Chapter 3, aircraft Hush Kit; green – Chapter 4; red - current Chapter 14 (European Aviation Environmental Report, 2019)

Table 2 AN contour areas for equivalent sound levels $L_{Aeq\ day}$, dBA for air traffic scenarios at the airport Kyiv/Zhulyany during the daytime

	Chapter 2	Chapter 3	Chapter 4	Chapter 14
Correspondent Stage of the US FAR 36	Stage 2	Stage 3	Stage 4	Stage 5
Character aircraft type	B737–200	B737–200 Hush Kit	B737–800, A320	B737MAX, A320neo
Spectral class in ANP database	101	102	104	103

For investigations of noise footprints corresponding to a single flight path, the coordinates of the boundaries and areas of noise contours are defined simply by the intersection of cylinder surfaces with predefined sound exposure level around the axially-symmetric noise source – an aircraft in flight, with the earth's surface of AN calculation (Zaporozhets O., Tokarev V., 1998; Zaporozhets O, Tokarev V, Attenborough K, 2011). In other words, the central axis of these cylinders is coincident with the flight path axis and the radius of a particular cylinder surface is defined as *the noise radius* R_n for a given noise level. The aircraft maybe represented as a moving point noise with constant velocity v. At the point of interest under the flight path:

$$L_A(t) = \underline{L_{Amax}} + 10 \lg [R_n^2 / (R_n^2 + v^2t^2)], \quad (1)$$

where L_{Amax} is the maximum value of $L_A(t)$ for a given noise event. For the simplified case, if noise source is considered without any directivity of sound radiation and sound absorption maybe neglected, it occurs when the aircraft is directly above the point of interest

$$LAmax = LAmax - 20 \lg Rn,$$

where $\underline{L_{Amax}}$ is defined by the flight mode (engine mode, flight velocity and aerodynamic configuration). If the further simplification of zero sound absorption is made, a formula (1) can be written for sound exposure level SEL in the following form:

$$SEL = LAmax + CR - 10 \lg (Rnv) \quad (2)$$

where C_R is the function of sound absorption along the distance between the trajectory and the point of interest and of the reference time duration T_0 (for SEL it is equal to 1 s).

In general case the whole flight path may be divided into separate sections, in each of which the flight parameters remain approximately constant, calculations are performed in each section k and the results are summed. If presume the overall flight path under consideration with flight parameters (engine thrust T, flight velocity v, and flight path angle γ) being quasi-constant and for the particular case of zero rotations of each segment of the path, it transforms to the equation for an ellipse (**Fig. 5**):

$$z2\sin2\gamma + x2 = Rn2. \quad (3)$$

If to assume that flight performances are the same between the ICAO Chapter 2 and Chapter 14 aircraft (or between Stage 2 and 5 for the US FAR 36, thus only noise characteristics were changed with time) – the flight path angle γ and thrust T maybe considered equal between them – the reduction of noise radius and area of the simplified noise footprint (ellipse) during the AN certification era is looking like at **Fig. 6**. Reached reduction for current NEO (MAX) aircraft on around 80% of the AN footprint and on 60 % the noise radius is looking similar with more strict calculations of the footprints shown at Fig. 4.

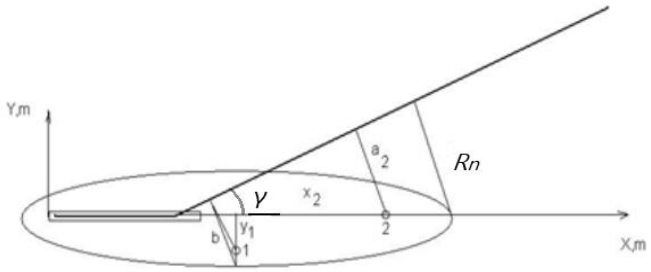

Fig. 5: A simplified form of noise footprint having the shape of an ellipse under the take-off flight path

The difference between the certified noise level at climbing flyover point (L_2) and the level corresponding to the final point on the contour L along the departure flight (or arrival noise contour in dependence to noise level at ICAO standard point No 3) axis may be written (Powell CA, 2003; Zaporozhets O, Tokarev V, Attenborough K, 2011):

$$L_2 - L = C\lg(R_n/a_2), \quad (4)$$

where the constant C defines the attenuation rate, for cylinder spreading its value is near to 10 (formula (2)) and for spherical spreading - near to 20 (formula (1)), a_2 is the minimum distance from the taking off path to the certification point № 2 (for departure).

Similar view is possible on the difference between the certified noise level at take-off (L_1) and the level corresponding to the final point on the contour L aside the flight – ICAO noise control point No 1 in **Fig. 5**. The area S of noise contour at aircraft take-off and climbing is proportional with quite high correlation to the product of L_2 and L_1:

$$\lg(S) = (L_2 + L_1) / C + D, \quad (5)$$

where constants C and D are different for various types of the sound levels L, L_1 L_2, and for different groups/types of the aeroplanes (Zaporozhets O, Tokarev V, 1998; Powell CA, 2003; Zaporozhets O, Tokarev V, Attenborough K, 2011). Better correlation between the footprint area and the levels was found for sound exposure levels like SEL and EPNL. For implementing the approach for strategic analysis of any air traffic and AN load scenario the correlations between the exposure SEL and maximum L_{Amax} sound levels may be used like:

$$SEL = A + B\, L_{Amax}. \quad (6)$$

Attention should be taken in mind in using such correlations like formula (6) (if the higher accuracy of the assessment should be considered), because the constants A,B are different not only for the types (groups) of the aircraft due to their different ANP

spectral class (explained in ANP database), but they are different for approach and departure flight stages, and even are dependent from the distance to flight axis (**Fig. 7**) also. It means that constants *C* and *D* in (2) may vary with the value of *L*, which is dependent to distance of noise source from the point of noise control. By-the-way, the difference between the sound exposure levels like *SEL* and *EPNL* is not so big and evident, *EPNL* is usually higher on 2-3 dB over the *SEL* (**Fig. 8**). Strictly talking not only the engine operation mode (thrust) at taking-off/climbing may influence the form of resulting contour for departure flight.

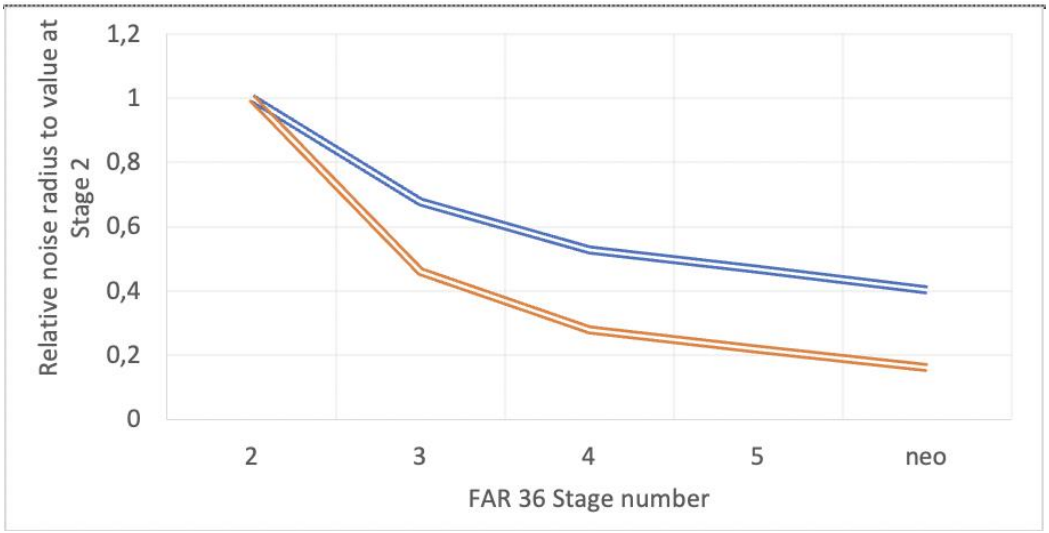

Fig. 6: Noise radius reduction with improvement of noise performances (due to FAR 36 standard stringency) relatively to FAR Stage 2 requirements: blue – relative noise radius; red – relative footprint (ellipse) area

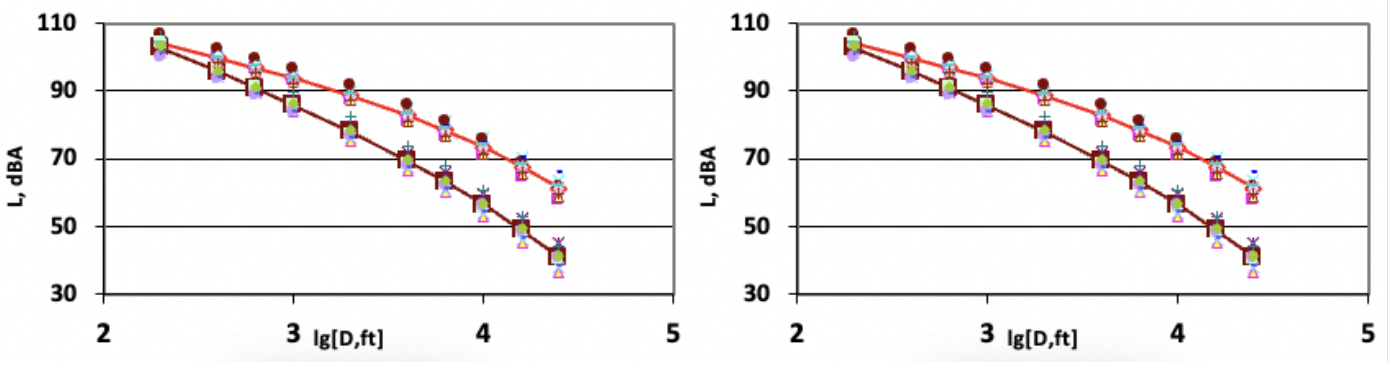

Fig. 7: Dependence (a) between SEL (red rhombuses) and LAmax (brown squares) and the difference (b) between them for the distance to flight axis for the aeroplane group A-320 and B-737

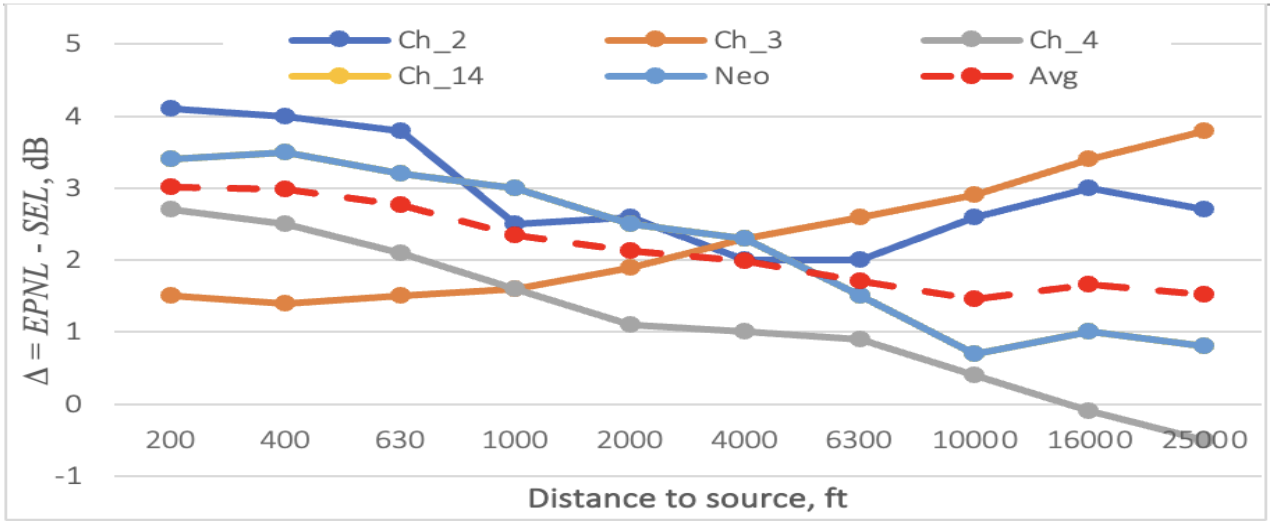

Fig. 8: Difference Δ between *EPNL* and *SEL* with distance for the aeroplane group A-320 and B-737 and different

AN stringency requirements

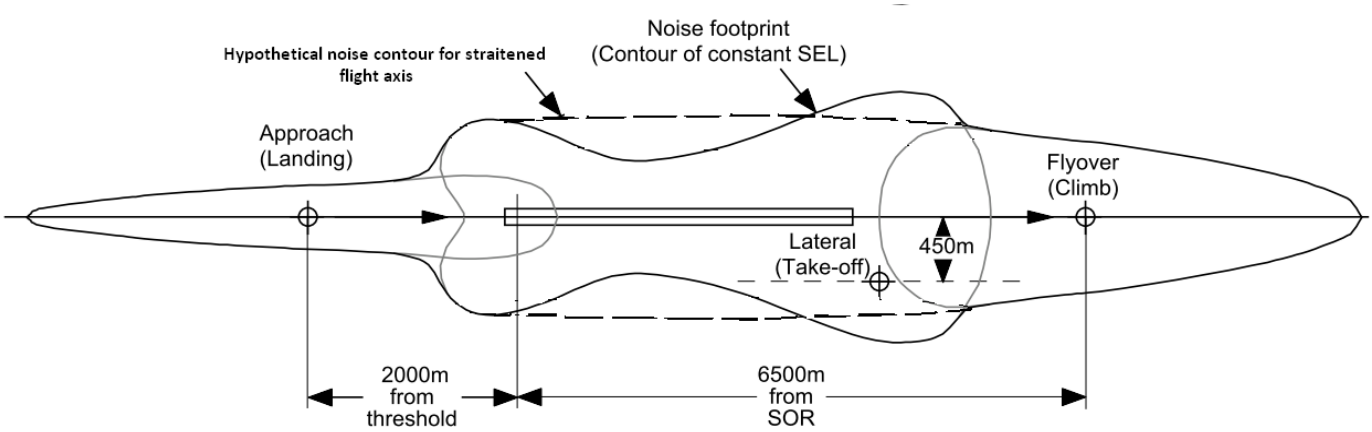

Fig. 9: Hypothetical noise contour for straitened flight during departure and excluded ground effect for sound propagation close to runway

Close to runway the flight altitudes are small and distances to contour line are quite big, so lateral effect is changing the line sufficiently, mostly for the flight path segments along taking-off (**Fig.** 9). If to use the concept of hypothetical contour, defined by equal noise exposure cylinder intersection with surface plane discussed above (**Fig. 5**) and the exposure level on cylinder surface is defined by character noise level for climbing flight stage (dashed line in F**ig. 9**) the changes in contour line and area are covered between themselves and the values are very close one to another for various models – simplified and in accordance with ICAO (ICAO 9911, 2018) requirements (**Fig. 10).**

The dependence for relative area $S=S_{StageK}/S_{Stage2}$ of noise contour at take-off and climbing (S_{TO+CL} in **Fig. 10**) from the acoustics performances (defined by FAR-36 requirements from the Stage 1 till Stage 5) is quite similar with contour area change in **Fig. 1** and **Tab. 1**, as it is shown in **Fig. 11,** and very similar with noise radius and simple footprint area reduction due to improvement of noise performances in **Fig. 6** (shown as FAR 36 standard stringency).

Particularly for the airplanes with noise performances in accordance to requirements of FAR 36 Stages 3-5, which are currently in operation, – the dimensions/areas of the simplified contours for departure flight are within 10% of the accuracy of INM contour data.

Bigger differences between the dimensions and areas of the simplified and INM contours for airplanes of Stage 1 and 2 performances may be described by a number of reasons – main of them that the method of assessment during AN certification procedures for these stages was different from existing ones and their data are normalized/harmonized with current method requirements not correctly always, even in ANP database (the same with INM database, which is very similar with ANP database). The results for FAR Stage 5 (equal to ICAO Chapter 14) performances are so small that the character contour for L_{Amax} night may lie closely to the runway, somewhere inside the territory of the aerodrome as shown in **Fig. 4**.

This ~60% reduction of the noise radius and ~80% reduction of the footprint area provides the similar shortening of the distance from runway to ANZ boarder with AN limit 65 DNL (residential development is prohibited). Once again returning to equivalent sound levels L_{Aeq} and/or noise indices L_{DN}, first of all because of their much higher correlation with noise impact assessment, one should consider the difference between them and single flight event value like *SEL* is as follows:

$$LAeq = SEL - 10 \lg T + 10 \lg n, \quad (7)$$

where T is a temporal interval of L_{Aeq} definition to be assessed, n – number of single events with sound exposure *SEL*. Here in formula (7) the value of *SEL* is defined for determining type of the aircraft in scenario under consideration, as it was discussed before.

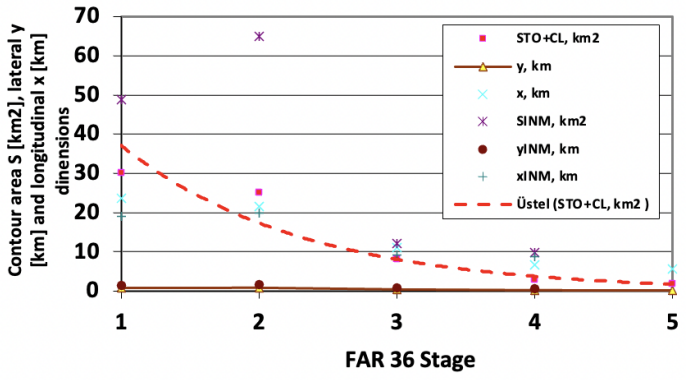

Fig. 10: Comparison between the dimensions and area for noise contour 75 dBA LAmax defined by simplified model and INM for Boeing-737 at departure with noise performances in accordance with FAR-36 requirements (from B737-100 for Stage 1 till Boeing-737MAX for Stage 5)

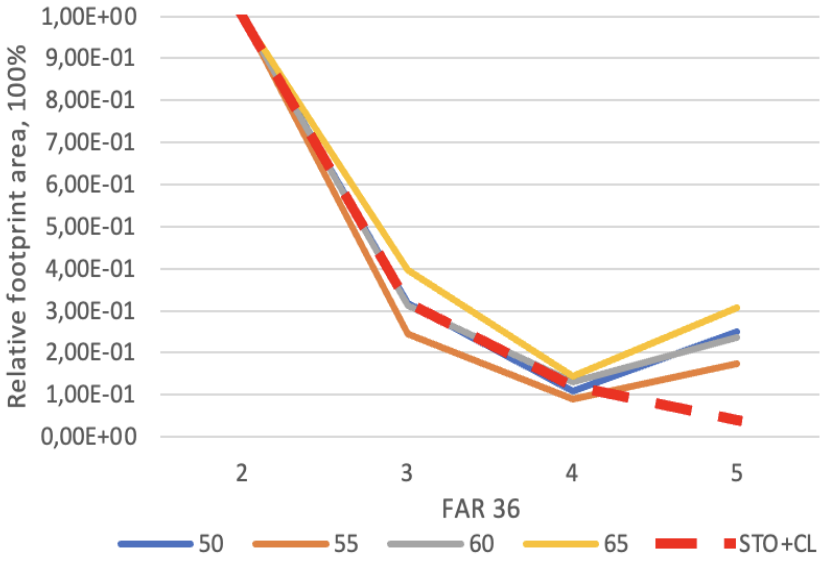

Fig. 11: Comparison between the relative areas for noise contour 75 dBA LAmax defined by simplified model and INM for Boeing-737 at departure (from Fig. 8, red dashed line) with noise contour areas LAeq day for Kyiv/Zhulyany airport in Tab. 1): 65 dBA – yellow line; 60 dBA – gray line; 55 dBA – light braun line; 50 dBA – blue line

This simplified formula (7) allows defining that the contour for night-time limit L_{Aeq} = 55 dBA (as defined by the Ukrainian rules for noise zoning (Konovalova O, Zaporozhets O, 2021)) the number of aircraft flight events n similar to determining type in the scenario should be ~10 if it is equal to ICAO Chapter 2 noise performances, rising till ~30 if the noise performances will be equal to ICAO Chapter 14 requirements. For daytime noise limit L_{Aeq} = 65 dBA the same assessment is showing the change in a number of events n between ~140 for ICAO Chapter 2 and >500 flybys for ICAO Chapter 14 aircraft flybys.

So, with quieter determining aircraft in a fleet of the scenario under consideration the dominance of the single noise exposure contour may not be diminished by noise equivalent contour. It may be a new principle condition for aircraft noise zoning determination in the future AN scenarios. Second principle result of last decade – human annoyance to AN became stricter, if the Shultz Curve has defined ~30% of annoyed population at L_{DN} = 65 dBA few decades ago, now the studies in EU and US airports define the same amount at 50-55 dBA. One of the reasons may be explained with big shortening of the distance for residential development close to airport. AN loading on the population of the air traffic is the same, but the visual impression of the departing and approaching aircraft may be bigger, so the current Annoyance Curve for aircraft noise is much closer to the Annoyance Curve for wind farm noise (which is most annoying at the moment among the environmental noise sources).

Aircraft produced today are 75% quieter than the first civilian jets that appeared in operation 50 years ago (**Fig. 4**). The newly manufactured aircraft typically produce around half the noise of the aircraft they are replacing, so with this advance the air traffic movements can double without increasing the total noise exposure output (ICAO Document 10127, 2019). During the 50 years of aircraft noise standardization from ICAO (1st Edition of Annex 16 – Aircraft Noise was published in 1969) and continuous strengthening of the requirements from ICAO Chapter 2 till current 14 (ICAO Annex 16, 2019) the cumulative reduction was gained up to ~35 dB, close to this value is necessary to be reached till the ACARE noise goal at 2050 (Flightpath 2050, 2011). The next strengthening of noise requirements for the aircraft may provide the conditions of disappearing the single event contours (footprints) with sufficient for analysis and management levels (L_{Amax} 75 dBA for the night and 85 dBA for the day), as they are used in Fig. 4, 6 and 8, from consideration in population exposure tasks.

3.1. Ground AN assessment

Tremendous reduction of the flight AN contours in airports during last decade provided new situation in AN assessment for the airports – contribution from the ground aircraft movements in AN exposure must be included in NEM and at further steps - in ANCP to manage the AN exposure and its impact on population. Previous AN exposure, defined by flight events, covered the contributions from ground events, as anybody may look from the **Fig. 2**, - AN contour for 1990s scenario cover completely the taxiways and apron with stands, which were not changes during last decades.

Enhanced modelling of aircraft taxiway noise, as it is discussed in (Page, J., et al., 2009; Page, J., Hobbs, C. and Gliebe, P., 2013), is a subject of inclusion in current

methodology of AN assessment (SAE AIR1845A, 2012; ICAO Doc 9911, 2018). The same approach is explained in (Zaporozhets O., Levchenko L., 2018) for AN from aircraft taxing, and for aircraft engine run-up noise (Zaporozhets O., Karpenko S., Levchenko L., 2021). Current NEM for airports should include these AN sources for effective realization of the ANCP also.

4. Measurement of Aircraft Noise at Kyiv/Zhulyany Airport

Quieter aircraft and more accurate calculation models produce conditions that residential areas are much closer today to airport territory then 4 decades ago (AN contours used for defining the ANZ boarder are much smaller). Accuracy of calculation methods currently are higher, it is quite similar with accuracy of the noise measurements.

It is necessary to mention that the new Ukrainian legislation allows airports to provide a systemic program to measure noise exposure in their vicinity (SAAU Order 585, 2020), taking into account both European and world best practice (Konovalova O., Zaporozhets O., 2021). First of all, there is very important because most of Ukrainian airport can be considered as city airports – they are surrounded by residential areas in all directions from runways. Second point of attention, there is a need to check the calculated quite short distances from the runways to the boundaries of the ANZ with prohibited human activities due to over-limit noise exposure. The airport on its own cannot minimise noise impacts – the AN exposure only, current circumstances provide new more strict requirements on AN exposure assessment. They are essential in order for the airport to maintain current operations and enable potential sustainable growth.

4.1. Measurements of aircraft taxing noise

Instrumental studies of air pollution and noise within the aerodrome "MA Kyiv/Zhulyany" are performed since 2018 (Synylo K., Ulianova K., Zaporozhets O., 2021). The location of the monitoring station for air pollution and noise was determined for research during the landing of the aircraft, the run along the runway, taxiing to the parking lot, taking into account the direction of the wind. In particular, the location of the measuring station was oriented to the prevailing (South Western, 190-210º) wind direction in the airport area. The monitoring station was located at a distance of 15 m from the edge of TaxiWay 2: 50.24.278 '030.27.739' (Fig. 10).

The results of the measurements allow us to validate noise and pollution models in the vicinity of the airport IsoBella (analogue INM, FAA, USA) and PolEmiCa (analogue of Emission Dispersion Modelling System EMDS, FAA, USA). The comparison of measured and modelled noise levels and concentrations of pollutants has shown that correlation coefficients are rather high (0.9…0.99) (**Fig. 11**).

The results of the measurements allowed us to gain the next targets: clarification of the emission factors of engines and aircraft noise levels in operational conditions; description of the noise and emission interdependencies during real flight operation, particularly for taking-off and landing modes. Measured data allow us to assess noise and emission interdependencies during taxing and takeoff run stages and confirm the linear dependence between noise levels, operational modes and emission indexes and possibility of the applying of Linear Interpolation to the ICAO Engine Emission Data.

Measurement results are important to prove the results of calculation, which are used for ANZ and for environmental capacity assessment of the airport, predefined by AN and LAQ calculations and limits. If the environmental capacity of the airport is smaller than operational – the optimization task is recommended to solved (Tokarev V., Kazhan K., 2014).

AN compatibility of the airport may be considered as broken if the ANZ are defined by calculation only, and the measurement results for AN are definitely higher at their borders. If the ANZ distances from the runway axis are smaller due to quieter aircraft implemented in operation such situation is looking obvious, so the calculations of AN contours, which are used for ANZ border defining, should be confirmed by AN measurements. Accuracy of AN measurements and calculations must be equalized if it is possible in reality (Zaporozhets, O. and Levchenko, L., 2021).

4.2. Comparison of flight noise measurement results with calculated and certification noise levels

The results of noise measurement in the vicinity of Kyiv/Zhulyany and Kyiv/Gostomel aerodromes were analysed from several points of view:

- comparison with normative values of environmental noise in accordance with the requirements of national norms and rules;
- comparison with the results of noise certification of types of aircraft operated at the aerodrome;
- comparison with the results of the calculation of the sound levels of the AN, performed to justify the boundaries of the zones of residential building restriction from noise conditions.

The results for the sound levels in Fig. 12, 13 (departure) and 14, 15 (arrival) indicate a wide range of deviations of the measured values from the averages, which

necessitates the analysis of samples for each type of the aircraft and the flight stage separately. Sound levels, in particular maximum sound levels, at a distance of 6-8 km along the take-off axis from the starting point on the runway dominate essentially over regulatory values of the rules (SSR-173, 1996) as for night ($L_{A\,max}$=75 dBA) so as for day ($L_{A\,max}$=85 dBA) time periods.

Fig. 10: Location of the noise and air pollution monitoring station during taxiing along the main Taxiway, turn on the Taxiway №2, take-off along the runway in Western direction

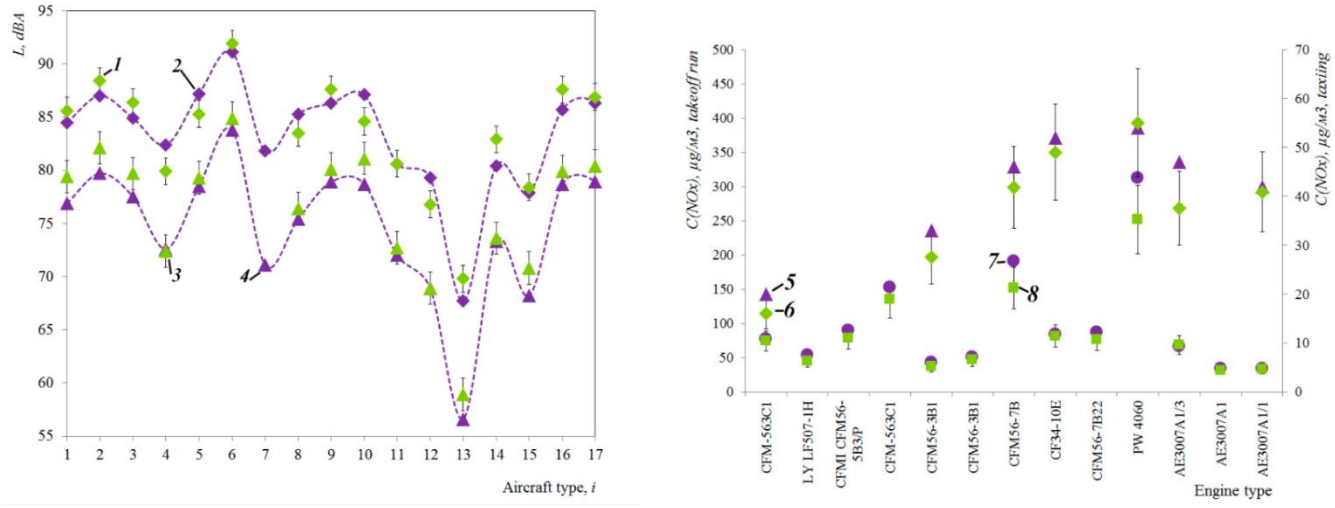

(a) **(b)**

Fig. 11: Comparison of measured and modelled noise levels (a) and concentrations (b) of the pollutants: 1 – calculated SEL, dBA; 2 – measured SEL, dBA; 3 – calculated LAmax, dBA; 4 – measured LAmax, dBA; 5 – calculated NOx concentration during taxiing C(NOx), μg/m3; 6 – measured NOx concentration during taxiing, μg/m3; 7 – calculated NOx concentration during take-off run C(NOx), μg/m3; 8 – measured NOx concentration during take-off run C(NOx), μg/m3

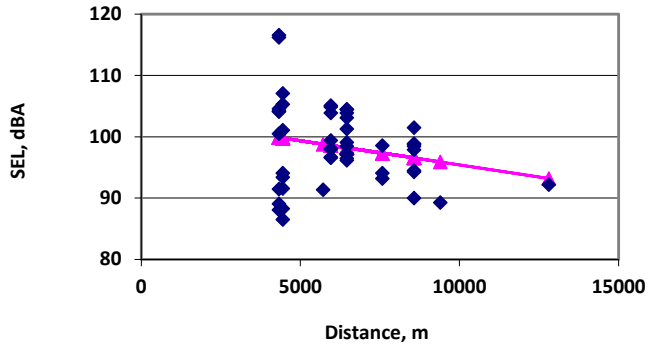

Fig. 12. Dependence of sound exposure levels L_{AE} from the distance to the point of aircraft start on runway during the aircraft departure (blue rhombus - measured values, pink triangle - linear approximation for the set)

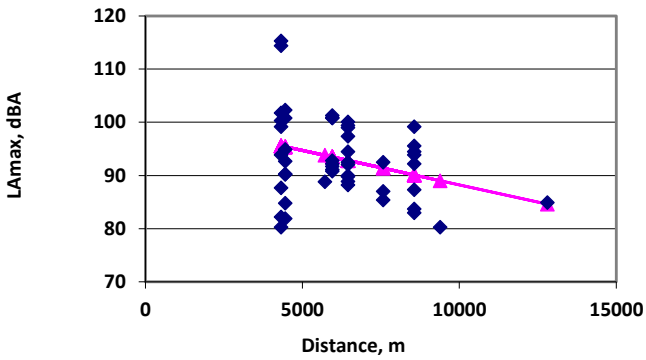

Fig. 13. Dependence of the maximum sound levels LA max from the distance to the point of aircraft start on runway during the aircraft departure

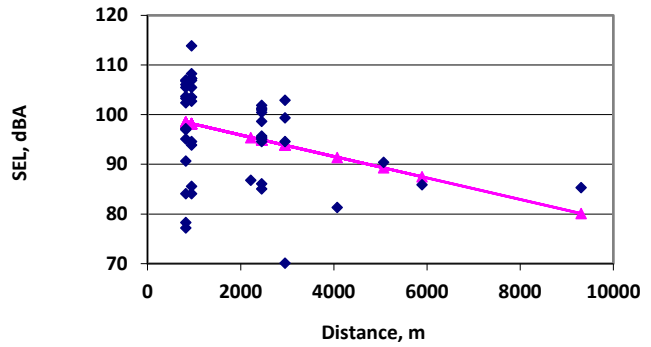

Fig. 14. Dependence of sound exposure levels L_{AE} from the distance to the runway end during the aircraft arrival

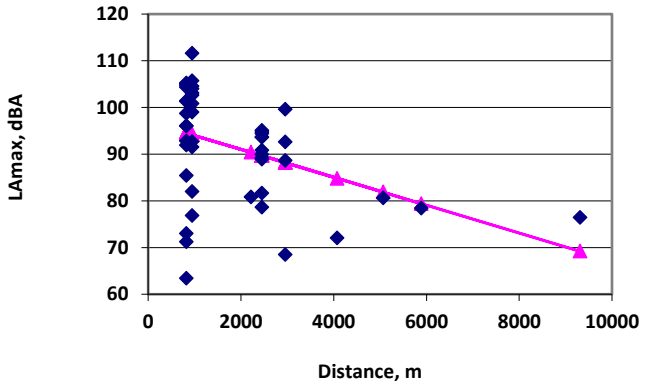

Fig. 15. Dependence of the maximum sound levels $L_{A\,max}$ from the distance to the runway end during the aircraft arrival

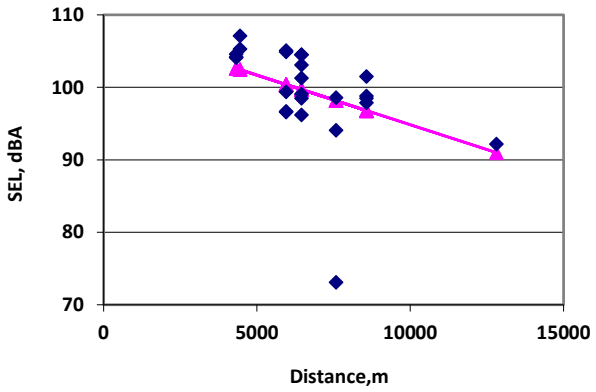

(a)

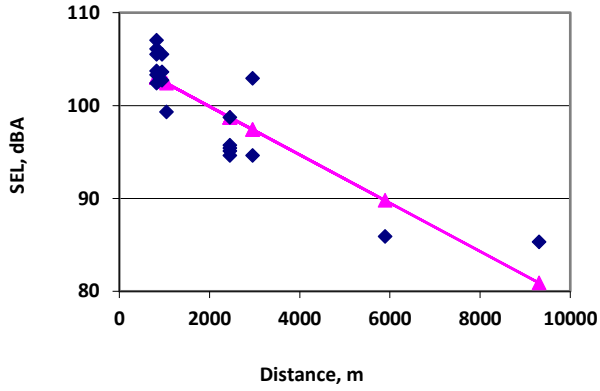

(b)

Fig. 16. Dependence of sound exposure levels LAE for An-124 departure from the distance to the point of aircraft start on runway: a) full set data; b) a set with excluded highly deviated data; blue rhombus - measured data, pink triangle - linear approximation for the set

The largest data set at Kyiv/Gostomel studies was obtained for AN events for the An-124 aircraft (sound levels for the departure in Fig. 16 and for the arrival in Fig. 17). The approximation for a complete data set indicates unsatisfactory statistical values (for arrivals the correlation coefficient = -0.330 and coefficients of linear approximation B0 = 99.4, B1 = -0.00155, etc.), so in each of the sets, in particular for arrivals (Fig. 17), the

measured data with significant deviations from the approximation line (marked in red rhombus in the corresponding figures) were excluded from further statistical analysis. The results for observation sets with the removed deviated data are much more correlated between themselves (standard deviations for a limited sample are 2-3 times smaller than the deviations for the full data set, correlation coefficient = -0.873 and coefficients of linear approximation B0 = 105.1, B1= -0.0026, etc). These highly deviated data were excluded from comparison with the noise certification data for the aircraft also. Comparison of the results of sound level measurements with calculations (Fig. 12-17) indicate minor differences (1-2 dBA) between them, especially with excluded highly deviated data, the assessment of which leads to the conclusion of sufficient accuracy of the calculations, in particular for aircraft An-124 (Fig. 16, 17), which determines the main noise load on the environment in airport Kyiv/Gostomel.

5. Conclusions

Aircraft activities and their AN exposure evaluation by measurement studies and modelling techniques may provide more accurate representation of its contribution to total noise exposure inside airport area and the improvement for: estimation of aircraft noise performances for actual operation conditions and precise exposure calculation from the aircraft at any stage of their operation; initial information for control of sanitary-hygienic requirements to aircraft noise of the airport; scientific grounding for ANZ around the airport; practical recommendations for instrumental monitoring of aircraft noise; improving of aircraft noise modelling system; estimation of aircraft contribution during different ground and flight stages to noise inside and outside the airport.

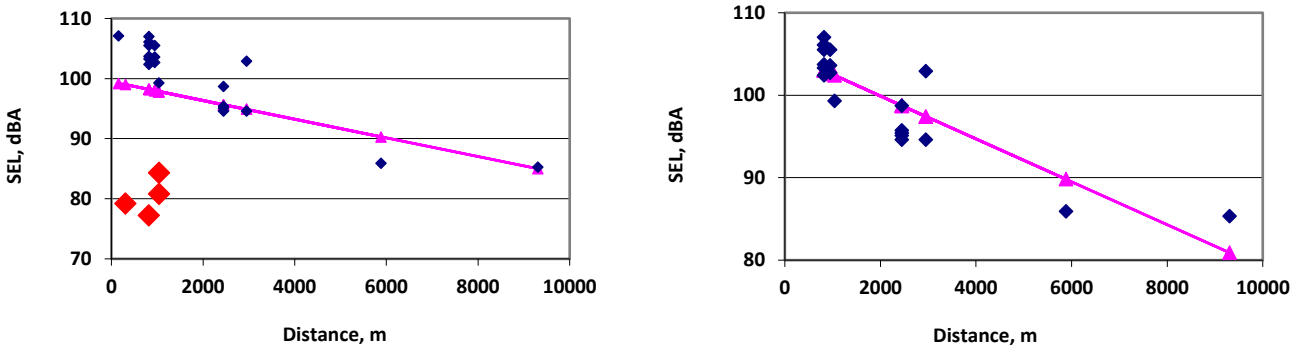

Fig.17. Dependence of sound exposure levels LAE for An-124 arrival from the distance to the runway end: a) full set data; b) a set with excluded highly deviated data; blue rhombus - measured data, pink triangle - linear approximation for the set; red rhombus - data with significant deviations from the approximation.

A significant reduction in noise emissions at the source and the creation of relatively quiet aircraft have led to the approach of noise contours with levels equal to the established limits for public health protection to the borders of the airport territory. In turn, this allows to bring the activities of the population, including their residence, closer to the airport. But the requirements for determining noise contours and corresponding zones remain unchanged, computational methods are still decisive for them.

AN compatibility of the airport may be considered as broken if the ANZ are defined by calculation of flight AN exposure only, and the measurement results for AN are definitely higher at their borders. If the ANZ distances from the runway axis are smaller due to quieter aircraft implemented in operation such situation is looking obvious, so the calculations of AN contours, which are used for ANZ border defining, should be confirmed by AN level measurements. Accuracy of AN measurements and calculations must be equalized if it is possible in reality because of their simultaneous importance. Current NEM for airports should include the contribution from ground surface AN sources for effective ANCP also, their absence in compatibility planning may provide the conditions for its inefficiency.

References

Akdeniz H., Sogut Z., Turan O., 2021. Assessment of Aircraft Noise Emissions at International Eskisehir Hasan Polatkan Airport with Multiple Approach Model. Jour. Aerosp. Technol. Manag., São José dos Campos, v13, e2621, 2021 Vol. 13 (2021) https://doi.org/10.1590/jatm.v13.1204

Alonso G. , Benito A. , Boto L. 2017. The efficiency of noise mitigation measures at European airports. Transportation Research Procedia, Volume 25, 2017, Pages 103-135

Buetikofer, R.; Thomann, G. Validation of FLULA, a time-step model for aircraft noise calculations. In INTER-NOISE and NOISE-CON Congress and Conference Proceedings; Institute of Noise Control Engineering: West Lafayette, IN, USA, 2001.

DSTU-N B V.1.1-31, 2013. Protection of territories, buildings and structures from noise. (National Standard of Ukraine ДСТУ-Н Б В.1.1-31:2013, in Ukrainian), 2014.

ECAC Doc 29, 2016. Report on Standard Method of Computing Noise Contours around Civil Airports. ECAC.CEAC Doc 29. Volumes 1, 2, 3. 4th Edition (2016).

European Aviation Environmental Report (2019) European Aviation Safety Agency (EASA), European Environment Agency (EEA), EUROCONTROL. https://doi: 10.2822/309946

Flightpath 2050 (2011) Europe's Vision for Aviation Report of the High Level Group. EU Directorate-General for Research and Innovation, Directorate General for Mobility and Transport on Aviation Research:32. https://op.europa.eu/en/publication-detail/-/publication/296a9bd7-fef9-4ae8-82c4-a21ff48be673

H.R.3547c, 1979. Aviation Safety and Noise Abatement Act of 1979 https://www.congress.gov/bill/96th-congress/house-bill/3547

Jäger D., Zellmann C., Schlatter F., Wunderli J.M., 2020. Validation of the sonAIR aircraft noise simulation model. Noise Mapp., vol. 8, 2020, p. 95–107.

ICAO Annex 16, 2019. ICAO Annex 16 to the Convention on International Civil Aviation — Environmental Protection: Volume I — Aircraft Noise, ICAO, Montreal, 2019.

ICAO Doc 9829, 2004. Guidance on the Balanced Approach to Aircraft Noise Management. ICAO Doc 9829, 1st Edition, ICAO (2004).

ICAO Doc 9911, 2018. Recommended Method for Computing Noise Contours Around Airports. ICAO Doc 9911, 2nd Edi-tion, ICAO (2018).

ICAO Document 10127 (2019) Final Report of the Independent Expert Integrated Technology Goals Assessment and Review for Engines and Aircraft: 225. https://store.icao.int/en/independent-expert-integrated-technology-goals-assessment-and-review-for-engines-and-aircraft-english-printed

Konovalova O., Zaporozhets O., 2021. Noise protection zones around Ukrainian airports as an element of balanced approach to noise control. International Journal of Sustainable Aviation, 7(3), pp 187–202 (https://doi.org/10.1504/IJSA.2021.119175).

Meister J., Schalcher S., Wunderli J.-M., Jäger D., Zellmann C., Schäffer B., 2021. Comparison of the Aircraft Noise Calculation Programs sonAIR, FLULA2 and AEDT with Noise Measurements of Single Flights. Aerospace 2021, 8, 388. https://doi.org/10.3390/aerospace8120388

Page, J., Bassarab, K., Hobbs, C., Robinson, D., Schultz, T., Sharp, B., Usdrowski, S., & Lucic, P., 2009. Enhanced Modeling of Aircraft Taxiway Noise, Volume 1: Scoping (No. ACRP Project 02-27).

Page, J., Hobbs, C. and Gliebe, P., 2013. Enhanced Modeling of Aircraft Taxiway Noise, Volume 2: Aircraft Taxi Noise Database and Development Process (No. ACRP Project 02-27).

Powell C.A. (2003) Noise Levels at Certification Points, NASA/TM-2003-212649:38. https://ntrs.nasa.gov/citations/20030107607

Rhodes D., Ollerhead J., 2011. Aircraft noise model validation. In Proceedings of the INTER-NOISE and NOISE-CON Congress and Conference Proceedings, The Hague, The Netherlands, 27–30 August 2001.

SAE AIR1845A, 2012. Procedure for the Calculation of Airplane Noise in the Vicinity of Airports, Aug 2012. https://www.sae.org/standards/content/air1845a

SAAU AR-381, 2019. Requirements for operators related to noise zoning of the airport vicinity. Ukrainian Aviation Rules, State Aviation Service of Ukraine (SAAU), dated 26.03.2019. https://zakon.rada.gov.ua/laws/show/z0461-19?lang=en/

SAAU Order 585, 2020. Methodical instructions on airport vicinity zoning according to noise conditions. State Aviation Service of Ukraine, dated 23.04.2020. https://avia.gov.ua/wp-content/uploads/2019/10/Nakaz-585-Pro-zatverdzhennya-metodichnih-rekomendatsij-2.pdf

SSR-173, 1996. State Sanitary Rules for planning of inhabited localities. Order of Ministry of Health No 173, dated 19.06.1996. https://zakon.rada.gov.ua/laws/show/z0379-96#Text

Synylo K., Ulianova K., Zaporozhets O., 2021. Air Quality Studies at Ukrainian Airports. International Journal

of Aviation Science and Technology, Volume 2, Issue 1, (2021), 4-14

Tokarev V., Kazhan K., 2014. Entropy approach for mitigation of environmental aviation impact and airport capacity increase. International Journal of Sustainable Aviation, 1(2), 2014. – Pp. 119-138.

US FAA Part 150, 1984. Airport Noise Compatibility Planning, Docket No. 18691, 49 FR 49269, Dec. 18, 1984. https://www.ecfr.gov/current/title-14/chapter-I/subchapter-I/part-150

Zaporozhets O., Karpenko S., Levchenko L., 2021. Calculation tool *NoBel* for sound propagation assessment of noise from gas turbines on the ground. *Proceedings of Inter-Noise 2021*, Washington, USA, (2021).

Zaporozhets O., Levchenko L., 2021. Detailed flight operation data for accurate aircraft noise assessment. *Proceedings of World Aviation Congress 2018*, NAU, Kyiv, Ukraine, (2018).

Zaporozhets, O. and Levchenko, L., 2021. Accuracy of Noise-Power-Distance Definition on Results of Single Aircraft Noise Event Calculation. Aerospace. 2021, 8(5), p 121.

Zaporozhets O., Tokarev V., 1998. Aircraft noise modelling for environmental assessment around air-ports. Applied Acoustics, 55(2) 99-127 (1998).

Zaporozhets O, Tokarev V, Attenborough K, 2011. Aircraft noise: assessment, prediction and control. Glyph International, Taylor & Francis

International Journal of Aviation Science and Technology

Research Article

Improving the Efficiency of Angular Velocity Sensors on Aircraft

Trung Vuong Anh[1], Hong Son Tran[2], Dinh-dung Nguyen[3]*, Truong-thanh Nguyen[4], Omar Alharasees[5], Utku Kale[6]

[1] *Faculty of Aviation Technical, Air defense-Air Force Academy, 100000 Hanoi, Vietnam*
vuonganhtrung@gmail.com - 0000-0002-4602-3975

[2] *Faculty of Control Engineering, Le Quy Don Technical University, 100000 Hanoi, Vietnam,*
tranhongson@lqdtu.edu.vn - 0000-0002-7956-2377

[3] *Department of Aircraft System Design, Faculty of Aerospace Engineering, Le Quy Don Technical University, 100000 Hanoi, Vietnam,*
dungnd@lqdtu.edu.vn - 0000-0002-8966-051X

[4] *Department of Military Science, Air Force Officer's College, 650000 Khanh Hoa, Vietnam,*
truongthanhna74@gmail.com - 0000-0001-7992-2291

[5] *Department of Aeronautics and Naval Architecture, Budapest University of Technology and Economics, Pest, Hungary,*
oalharasees@edu.bme.hu - 0000-0002-6899-6057

[6] *Department of Aeronautics, Budapest University of Technology and Economics, Pest, Hungary,*
kale.utku@kjk.bme.hu - 0000-0001-9178-5138

Abstract

With the development of science and technology, intelligent systems on aircraft help users know the device's operating status in real time. Using smart devices shortens the time for maintenance, repair, and operation of ground equipment and aircraft equipment. Therefore, building devices capable of self-diagnosis and warning failure are essential in aeronautical engineering. In many published studies, the authors often use the foundation of classic algorithms such as genetics, neural networks, and AI to solve the problem of identification and troubleshoot some simple devices. In Vietnam, there are currently not many published studies on failure diagnosis in aviation engineering, so the author's research has built the foundation for developing studies on fault diagnosis crash in the future. The primary purpose of the research is to create a complete automatic fault diagnosis and repair system for a specific class of inductance (angular speed sensor). The algorithms proposed in the paper are simulated on Matlab Simulink software, which will prove the feasibility of the proposed algorithm. In future studies, the author will apply new algorithms to build more complex fault diagnosis systems for other objects on the flying device.

Keywords

Angular velocity sensor
Fault detection
Fault diagnosis
Aircraft

Time Scale of Article

Received 19 May 2022
Revised until 11 September 2022
Accepted 21 December 2022
Online date 29 December 2022

1. Introduction

Given the expected growth in passenger levels and the continued expansion of the world's aviation network with more aviation connectivity, sustainable air transportation will be a critical global concern. To manufacture gradually more efficient and ecologically friendly airplanes, new technical alternatives are becoming increasingly necessary (Arockiam, Jawaid and Saba, 2018), (Iemma, Pisi Vitagliano and Centracchio, 2018), (Vieira and Bravo, 2016). Early and reliable

*: Corresponding Author Dinh-dung Nguyen, ddnguyen@vrht.bme.hu
DOI: 10.23890/IJAST.vm03is02.0205

automated and self-diagnosis of faults (Wang, Zarader, and Argentieri, 2012) (Chen et al., 2009) that may affect structural loads contribute to overall aircraft design optimization(CHU et al., 2022) and, as a result, weight reduction for improved overall performance (Cardei and Du, 2005) in terms of sustainable aviation systems, optimal fuel, noise, range, and environmental footprint.

Sensors play a very important role in aerial vehicles (AV); the quality of sensor operations determines the stability and safety of the AV operation (Khamis, 2021; Yang, 2021). As a result of the reduced flying duration, the least overall maintenance cost is offered. The standard operating procedure in this industry is to maintain an aircraft at optimal maintenance time and cost (Orhan, Kapanoğlu, and Karakoç, 2011). Many authors have researched the sensors on AVs and have come up with methods to fix the sensor damaged during the AV operation. For example, Hajiyev and Caliskan (2005), proposed a method for detecting and isolating aircraft sensor and control surface/actuator faults that impact the Kalman filter innovation sequence mean (Hajiyev and Caliskan, 2005). This approach was created to estimate the nonlinear flight dynamics of an F-16 fighter and the impacts of sensors and controlling surface/actuator failures, and it's particularly beneficial for isolating sensors and controlling surface/actuator failures. However, further research (Hajiyev and Caliskan, 2000) highlighted the failures impacting the covariance of the innovation sequence, which are not explored in this study.

On the other hand, the sensors on AVs operate in individual systems (Brooks and Roy, 2021), so their role also varies depending on the importance of the system to which it provides the signal. Therefore, in some studies, researchers also focused on studying a number of different sensors such as air data parameter sensors (P Lu et al., 2015), engine parameter sensors (Xue, Guo and Zhang, 2007) or other sensors on helicopter UAV (Hajiyev and Soken, 2013). In addition, several methods, including Kalman filters (Xue, Guo and Zhang, 2007; P Lu et al., 2015; He et al., 2020), self-diagnostic (Sullivan, 1988; Tuan, Firsov and Pishchukhina, 2012), adaptive models (Peng Lu et al., 2015), fuzzy tuning (Kim, Choi and Kim, 2008), and machine learning (Baskaya, Bronz and Delahaye, 2017) have been applied to identify faults of sensor operations on AVs.

In Vietnam, there have not yet been many studies on sensors on AVs, while several studies have been focused on mining using existing equipment and fixing errors using good block substitution methods available. Therefore, this study presents an approach focusing on building a self-diagnostic, fault-resolving sensor system using the output parameters of the sensors, which can be applied to research and development of intelligent sensor systems on AVs. In a previous study (Tran et al., 2021), an algorithm to diagnose the fault location of the sensor was give in the following Fig. 1.

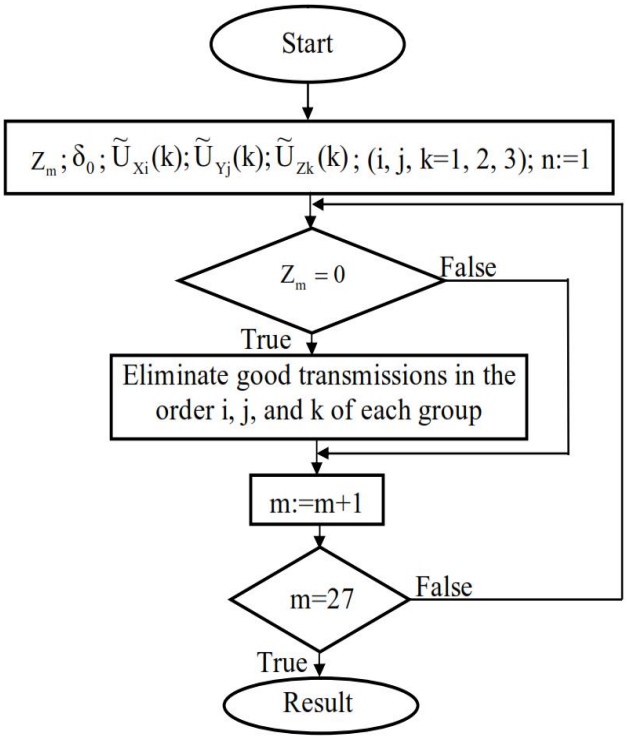

Fig. 1. Algorithm flowchart representing fault diagnostic algorithm

A next problem needs to be solved that is to find the cause of the fault and fix it (if possible). To solve this problem, it is necessary to consider the typical fault modes of angular velocity sensor (Isermann, 2005) such as drifting signal, changing gain, and broken wire. The graph representing the signal form of the failed angular velocity sensor is shown in Fig. 2.

Where:

1- The standard characteristic curve of the sensor.

2- Positive drift signal characteristic curve of sensor.

3- Negative drift signal characteristic curve of the sensor.

4- Up amplification coefficient characteristic curve of the sensor.

5- Down amplification coefficient characteristic curve of the sensor.

6- Broken negative wire characteristic curve of the sensor

7- Broken positive wire characteristic curve of the sensor.

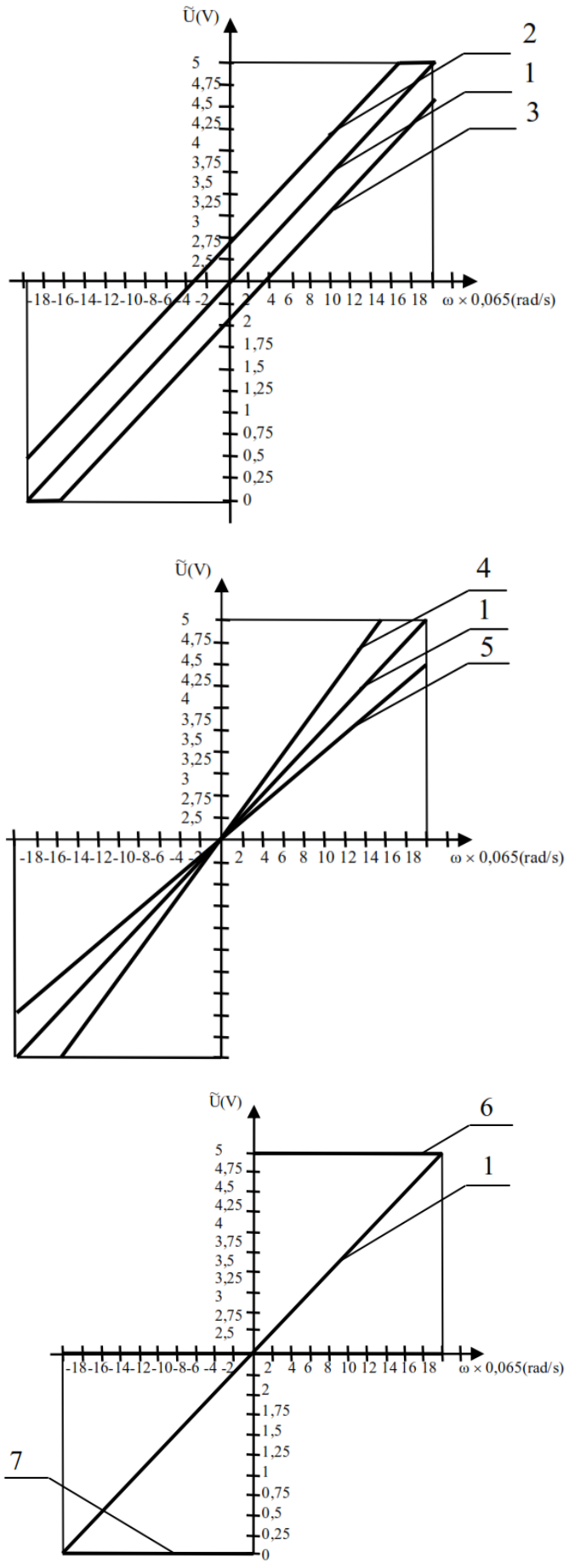

Fig.2. The graph shows the signal form of the fault sensor

When a fault occurs, for each type of fault, the mathematical model of angular velocity sensor has different forms and is specifically shown as follows:

- For the drift signal type

$$\widetilde{U}_{Dx}(k) = k_{Dx}\omega_X(k) + \Delta U_0(k); \Delta U_0(k) \neq const \quad (1)$$

- For the amplification coefficient changes type

$$\widetilde{U}_{Dx}(k) = \tilde{k}_{Dx}\omega_X(k) + M_1(k);\ M_1(k) = \frac{\tilde{k}_{Dx}}{k_{Dx}} = const \neq 1 \quad (2)$$

- For the broken wire

$$\widetilde{U}_{D_X}(k) = \underbrace{\widetilde{U}_{D_X}(k)}_{Max} = const\ ;\ \widetilde{U}_{D_X}(k) = \underbrace{\widetilde{U}_{D_X}(k)}_{Min} = const \quad (3)$$

Thus, for the above three types of fault, we find that the fault due to drift signal or by changing the gain can be overcome if we determine the values $\Delta U_0(k)$ and $M_1(k)$, and for damage caused by broken wire, it cannot be fixed.

2. Methods

Firstly, we build an algorithm to identify fault of the sensors in the improved sensor block. To simplify the calculation, we divide it into two types of faults: wire break and zero drift or gain change. The fault parameter calculation to lead to the fault identification is determined by the following expression:

$$Z_1 = \{|\widetilde{U}_D(k)| > U_{D\_max}\} = \begin{cases} 0 - \text{fault for signal drift or amplification coefficient changes} \\ 1 - \text{fault for broken wire} \end{cases} \quad (4)$$

Where: $\widetilde{U}_D(k)$: the value output of sensor.

U_{D_max} : the maximum value output of sensor.

From expression (4), we build an algorithm to determine the fault type in the general case as follows:

The value N depend on the accuracy of the algorithm. Thus, using the algorithm in Figure 3, we have diagnosed the general form of the problem. After that, we build an algorithm to diagnose specific types of problems.

For the fault type due to wire break. The expression to calculate the parameter to determine the broken wire is as follows:

$$Z_2 = \{|\widetilde{U}_D(k)| < U_{D\_min}\} = \begin{cases} 0 - \text{fault for broken positive wire} \\ 1 - \text{fault for broken negative wire} \end{cases} \quad (5)$$

Where: U_{D_min}: the minimum value output of sensor.

From the above expression, it is possible to build a diagnostic algorithm to determine the fault caused by the wire break as follows:

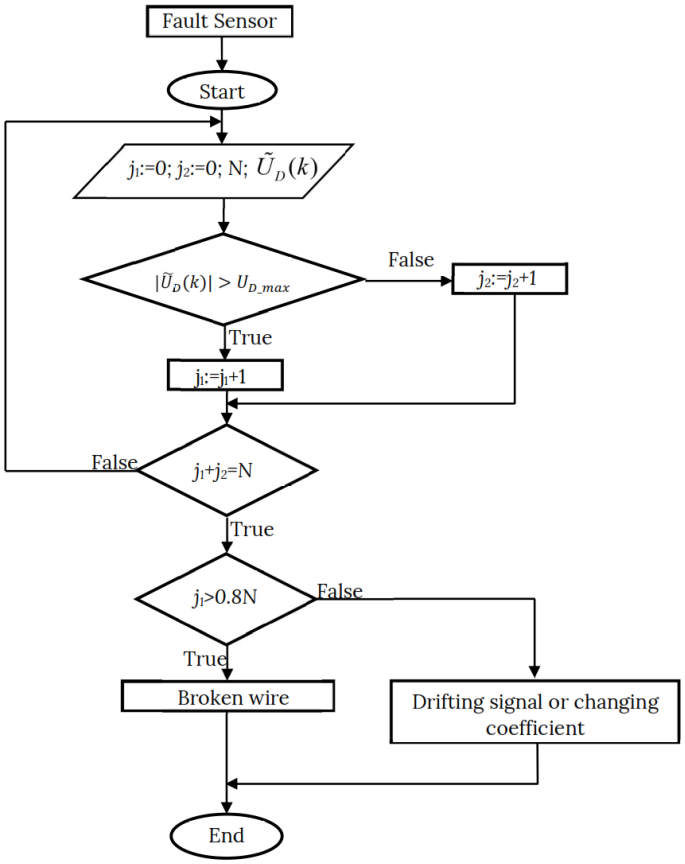

Fig.3. Algorithm flowchart representing fault identification in general case

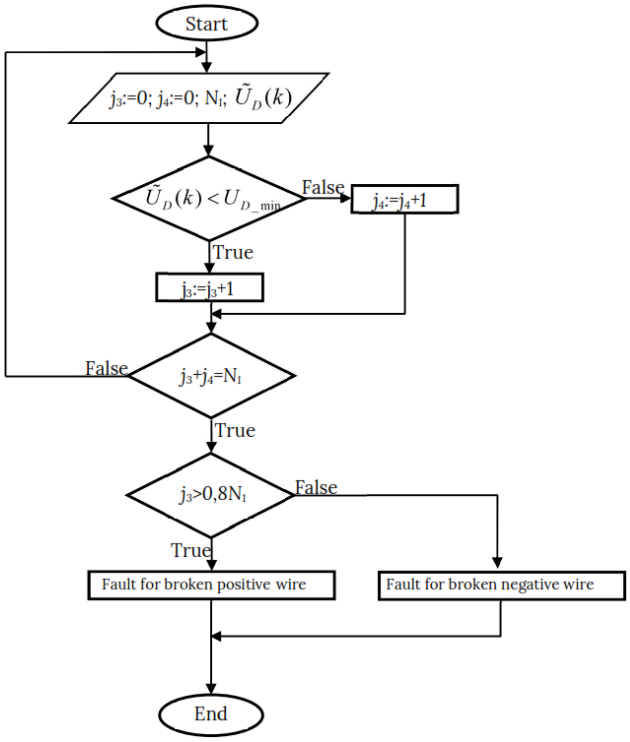

Fig.4. Algorithm flowchart representing fault identification in broken wire case

The value N_1 depend on the accuracy of the algorithm. For the fault type drift or gain change, the parameter calculation expression to build the fault type diagnostic algorithm is as follows:

$$Z_3 = \{\Delta U_0(k) = \tilde{U}_D(k) - \hat{U}_D(k) = const\} = \begin{cases} 0 - & \text{fault for signal driff} \\ 1 - & \text{fault for amplification coefficient changes} \end{cases} \quad (5)$$

Where: $\hat{U}_D(k)$: the calculated value output of sensor.

But first, we need to build an algorithm to determine the value of U_{0TB} to serve as a basis for building a problem diagnosis algorithm.

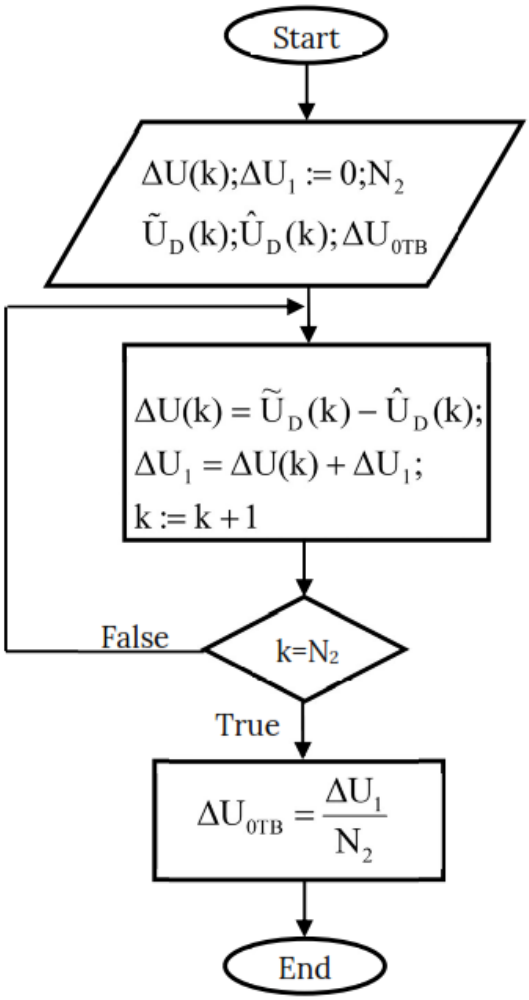

Fig.5. Algorithm flowchart representing determined value U_{0TB}.

The value N_2 depend on the accuracy of the algorithm. After determining value U_{0TB}, we can buid fault identification algorithm in **Fig.3.**

From formula (5), we build an algorithm to diagnose the fault type of the inductor in case the fault is caused by drift or change in gain as follows:

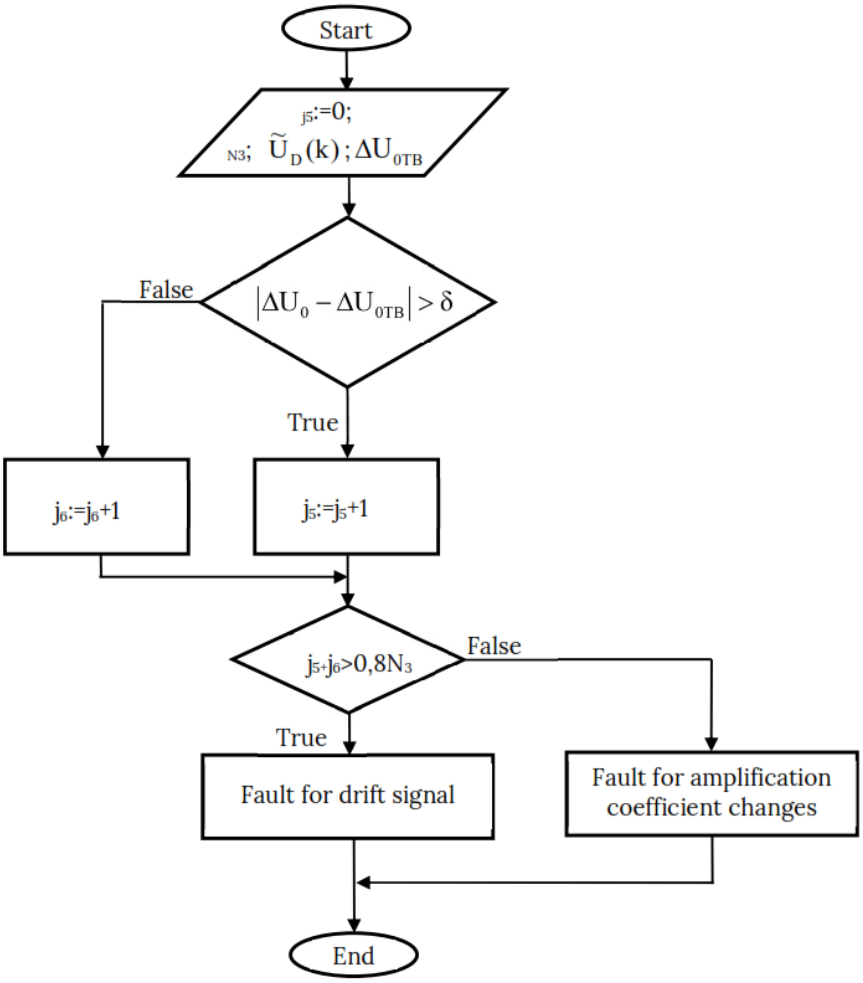

Fig.6. Algorithm flowchart representing determining the identify of drift or change in the transmission gain

Similar to the previous algorithm, the value N_3 depend on the accuracy of the algorithm. Thus, we have perfected the method of identifying fault modes of angular velocity sensor. Inductor block troubleshooting is conducted for transmitters that have been identified as having a remedial problem during the identification process mentioned above. In which sensors have a remedial fault including fault due to drift signal or fault due to gain change.

- For the fault due to drift signal. The physical nature of drift signal is that the actual output value of the sensor deviates from the standard output value by a constant amount over time. The drift value is described by the following expression:

$$\Delta U_o(k) = \tilde{U}_D(k) - \hat{U}_D(k) \quad (6)$$

Where: $\Delta U_o(k)$- Deviation between the actual output value of the sensor and the standard output value;

Thus, after determining the value of $\Delta U_o(k)$ allows us to fixed the output signal from the sensor to see if there is a drift problem. The corrected value is described by the following expression:

$$\tilde{U}_{D.FIXED\_1}(k) = \tilde{U}_D(k) - \Delta U_o(k) \quad (7)$$

Where: $\tilde{U}_{D.FIXED\_1}(k)$- The output value of the sensor has been drift signal corrected.

- For problems due to gain change. The physical nature of the fault due to a change in gain is that the output value of the inductor is always proportional to the reference input value by a constant value and other than 1. If the gain value changes, the gain is described by the following expression:

$$M_1(k) = \frac{\tilde{U}_D(k)}{\hat{U}_D(k)} = const \neq 1 \quad (8)$$

Or we can express through the gain factor as follows:

$$M_1(k) = \frac{\tilde{k}_D(k)}{\hat{k}_D(k)} = const \neq 1 \quad (9)$$

Where: $\tilde{k}_D(k)$- Actual gain of sensor.

$\hat{k}_D(k)$- Standard gain of sensor.

$M_1(k)$- Ratio gain.

In the ideal case, the value of the scaling factor is 1 and we denote it as $M_0(k)$. Thus, the difference between the scaling factor in the case of error due to the gain change and the ideal case is expressed by the following expression:

$$\Delta M(k) = M_1(k) - M_o(k) \quad (10)$$

From expressions (8), (9), (10) we see that when determining the scaling factor $M_1(k)$ allows us to correct the output signal from the inductor with the error of the gain change. The correction value is described by the following expression:

$$\tilde{U}_{D.FIXED\_2}(k) = \frac{\tilde{U}_D(k)}{M_1(k)} (M_1(k) \neq 0) \quad (11)$$

Where: $\tilde{U}_{D.FIXED\_2}(k)$- The output value of the sensor has been corrected for gain change error.

The algorithm to determine the value of $M_1(k)$ is as follows:

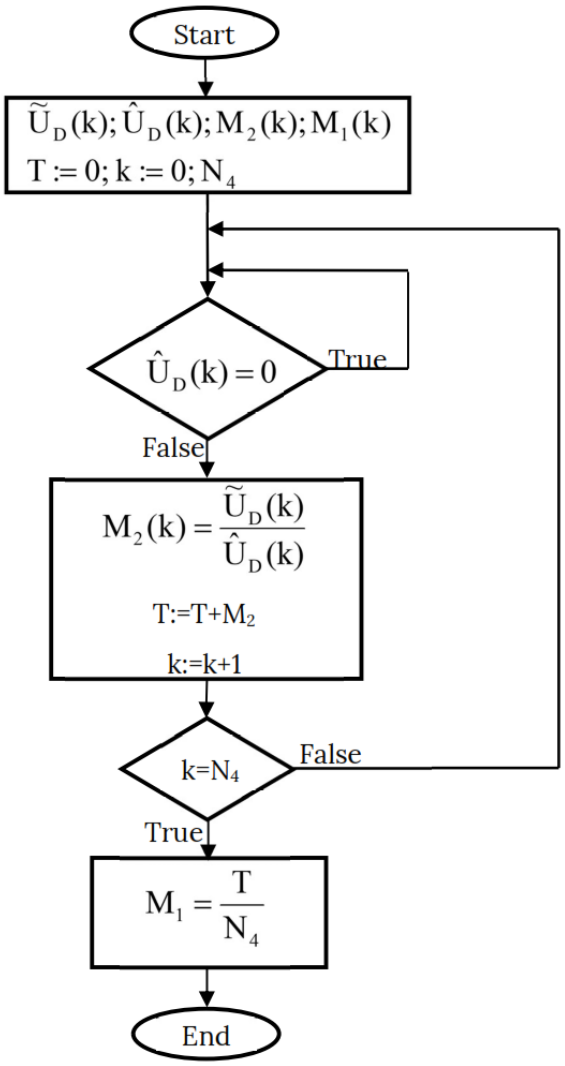

Fig.7. Algorithm flowchart representing determined the amount of gain change

The value N_4 depend on the accuracy of the algorithm. The general algorithm for fixed the sensors block is defined as follows

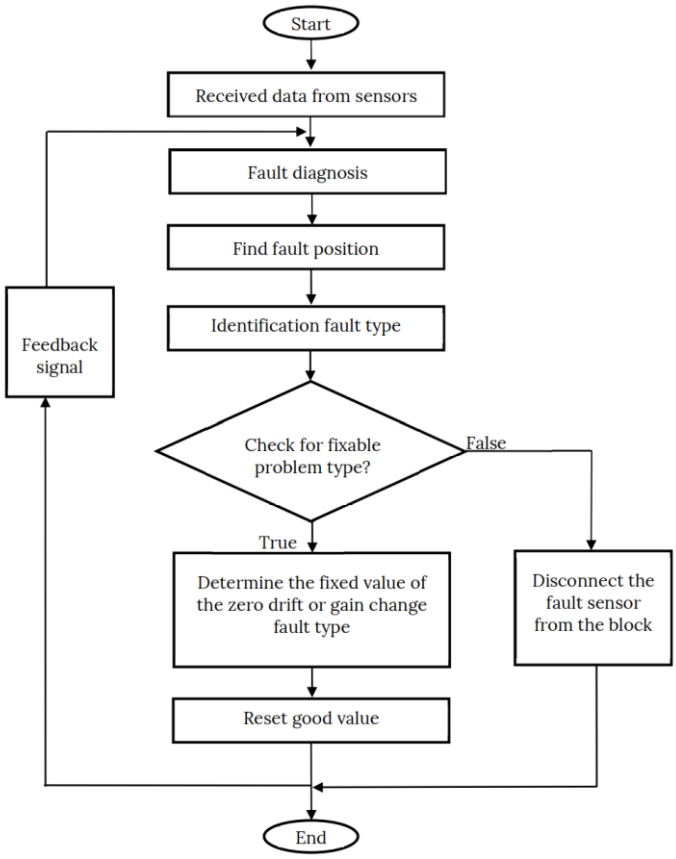

Fig.8. General algorithm flowchart representing fixed fault of sensors

Build detailed algorithm diagram for the system

- For the type of fault due to drift signal. The diagnostic algorithm for fault for sensor with drift problems is not implemented on the basis of expressions 1 to 11 and the mentioned algorithms are as follows:

Where: Block [1] - Algorithm to diagnose a problem on the sensor in the general case;

Block 3 – Algorithm for identification a type of fault in general case.

Block 5 - Algorithm to calculate the value U_0TB.

Block 6 - Algorithm for specific identify of problems caused by drift or change in gain.

- For the fault form due to the change of gain factor. Troubleshooting diagnostic algorithm for faulty sensor due to gain change is performed on the basis of expressions 1 to 11 and the algorithms in [1] are as follows:

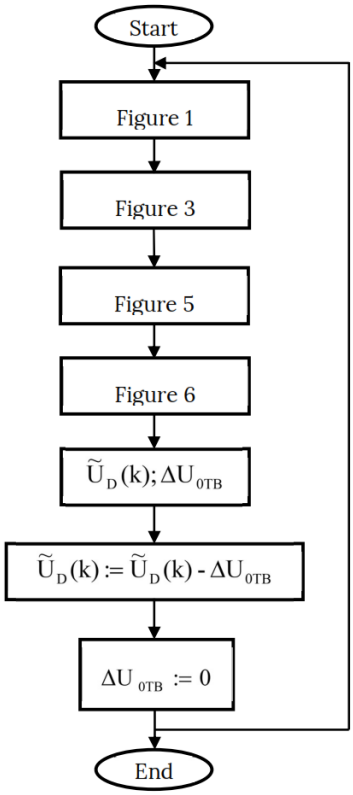

Fig.9. Algorithm flowchart representing fixed fault in driff signal case

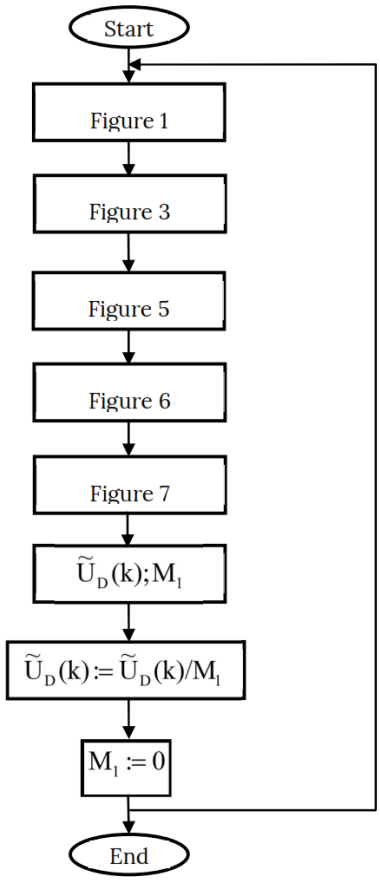

Fig 10. Algorithm flowchart representing fixed fault in amplification coefficient changes case.

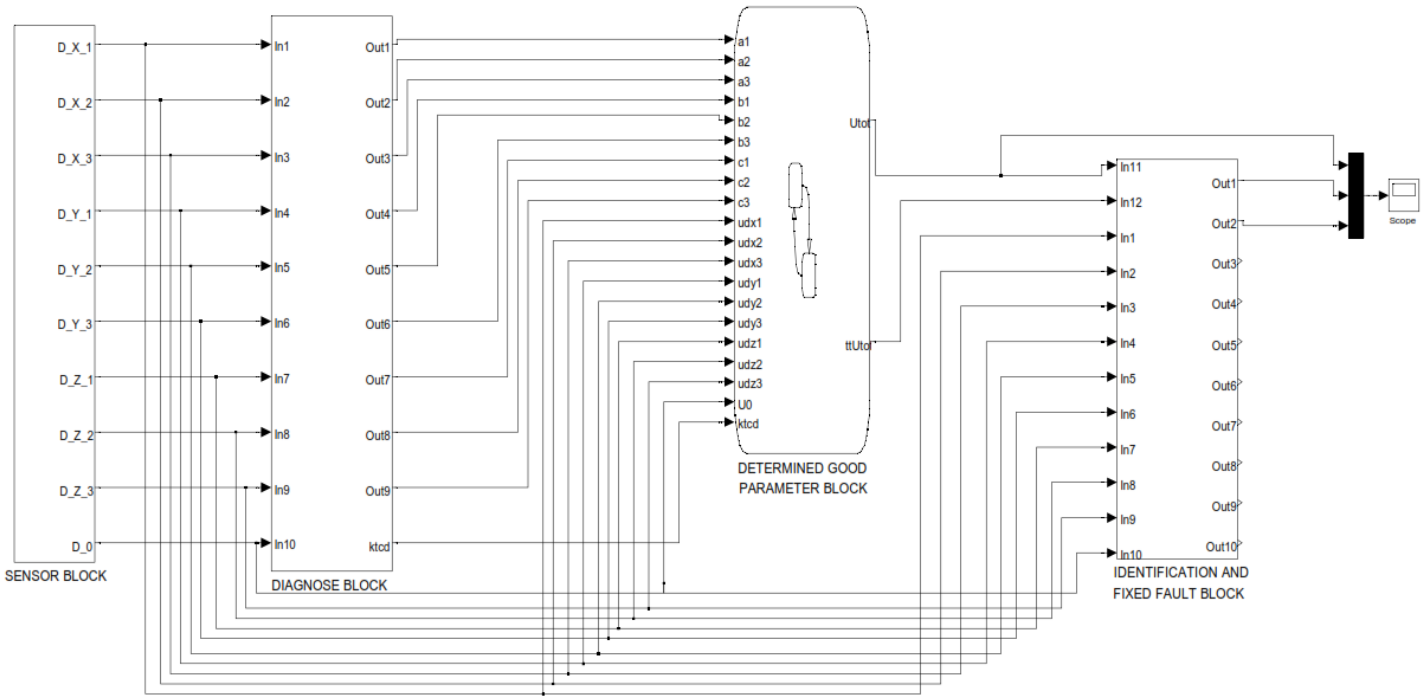

Fig 11. General simulation diagram for diagnosing, identifying and fixed fault of angular velocity sensors

Where:

Block 1 - Algorithm to diagnose a problem on the sensor in the general case

Block 3 – Algorithm to identificate a type of fault in general case.

Block 5 - Algorithm to calculate the value . U_{0TB}

Block 6 - Algorithm for specific identify of problems caused by drift or change in gain.

Block 7 - Algorithm for determined the amount of gain change

3. Results

On the basis of diagnostic results for the automatic identification and fixed fault algorithm on MATLAB Simulink simulation done by the current authors. The parameters are assumed that:

$$U_{D\_max} = 550$$

$$U_{D\_min} = -550$$

$$N = N_1 = N_2 = N_3 = N_4 = 100 \quad (9)$$

$$\delta = 0.5$$

On the basis of diagnostic results, continuing to simulate the automatic error identification algorithm. Based on the flowchart, the algorithm determines the type of the drift problem or the change in the gain of the sensor (Figure 6). Suppose we have determined that fault sensor is SENSOR_X1, which is good SENSOR_X2 sensor. The schematic diagram of fault identification is shown in Figure 12.

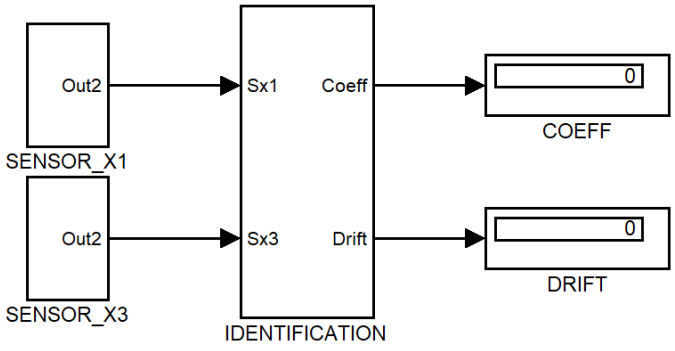

Fig 12. Fault identification simulation diagram

The automatic fault identification process is divided into 2 stages: Stage 1 calculates the parameters for the identification process using formulas 1 to 6 and algorithm 5 and algorithm 6. Diagram The simulation is shown in Figure 13.

Where algorithm 5 is represented in block CAL_U0TB and algorithm 6 is represented in block IDENTIFICATION. Simulation is performed in the two cases of sensor SENSOR_X1 with signal drift fault by changing the drift coefficient and the signal gain of the inductor, respectively. Running the simulation program gives us the results shown in Figure 14.

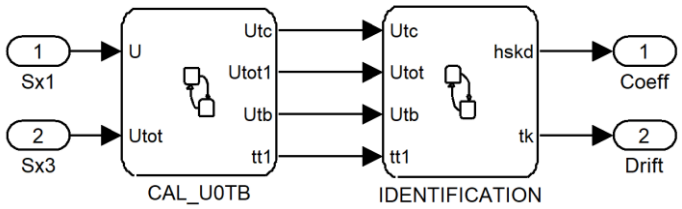

Fig 13. Block diagram of the fault identification block

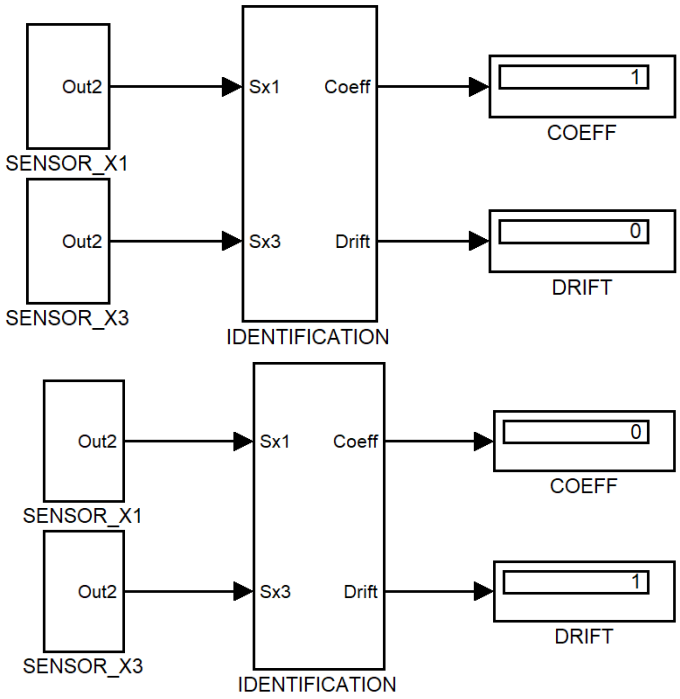

Fig 14. Fault identification simulation results

From the fault identification results in case of drifting sensor, we see that the output signal of the gain is zero - there is no error due to the gain change, the output signal of drift not equal to 1- is there a problem due to drift error. This proves that the drift fault detection system does not work well and can meet the requirements when there is no signal drift fault or gain change. Next, we simulate the process of automatically repairing the fault of the inductor, the simulation diagram is shown in Figure 15.

In which the troubleshooting block consists of 7 input signals and 2 output signals. Hskd-Fault signal due to gain change, tt2-end signal of fault identification due to gain change, Utc-signal from inductor fault , Utot- signal from inductor is working well, tk- signal is there any drifting problem, Utb-Average error value of inductor signal has problem and good sensor, tt3-signal of process end drift fault identification. 2 output signals are 2 signals that have been fixed.

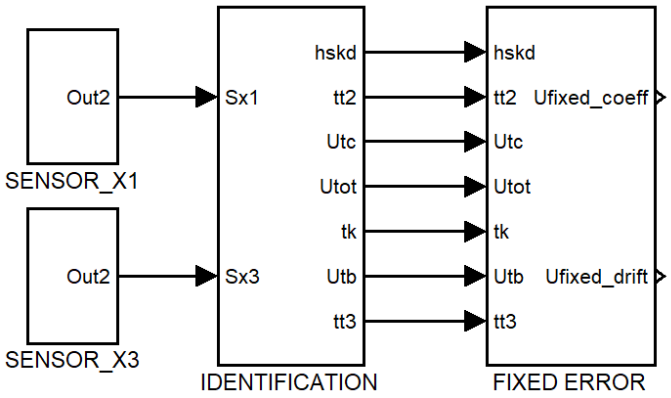

Fig 15. Diagram to simulate the process of automatically identifying and fixing fault

To simulate the process of automatic troubleshooting, we simulate in two cases: sensor has a problem due to a change in gain; Is there a problem with the transmission due to drift? For the case of sensor, there is a problem due to the change in gain. We assume that the SENSOR_X1 inductor has problems due to gain changes or has problems due to no-signal drift, the SENSOR_X3 inductors are good inductors. The simulation diagram and simulation results are shown in Figures 17, 18, 19. The output value of the sensor has been multiplied by the factor k in Figure 19.

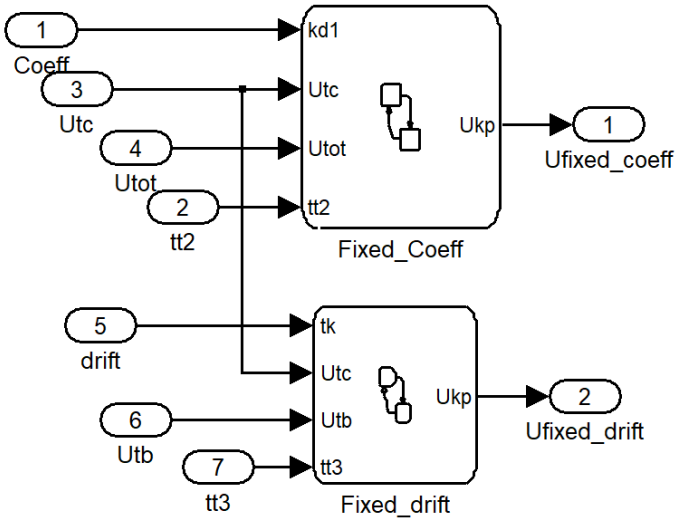

Fig 16. Automatic fixed fault signal block diagram

Where: 1-Fixed fault sensor signal; 2-Good sensor signal; 3-Fault sensor signal. Based on the simulation results, we can see that initially the troubleshooting signal coincides with the signal of the faulty transmitter due to the delay time to calculate the fault identification and fixed fault. After this delay, the rectified signal has the same form as that of the well-functioning sensor. This proves that the algorithm to fix the problem caused by changing the gain coefficient shown in Figure 10 is completely correct.

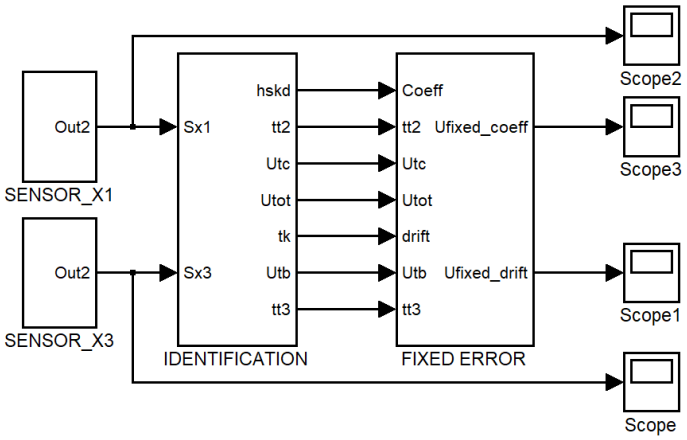

Fig 17. Diagram to simulate the automatic fixed fault signal process

4. Conclusions

From an industry standpoint, any sophisticated model-based solution for aviation systems should be clearly shown in terms of added value. Any modifications to an established and well-proven scheme must include a feasible technological solution that improves performance while maintaining resilience. New methods and technologies are risky, and they must be thoroughly validated and verified before being implemented in real-world systems. Hundreds of aircraft have been mass-produced in the civil aircraft industry for several decades. Some improvements can be planned throughout the aircraft building process, such as expanded range, increased maximum take-off weight, and passenger capacity.

vOne critical need in this context is that the new design be adaptable to different aircraft types and systems. For the adaptability of a novel solution in the context of mass production, easy-to-tune high-level input parameters are required. A small number of tuning parameters is preferable to reduce the validation and verification operations necessary for certification. Identify and isolate aircraft faults while maintaining aircraft performance operations and safety as a minimum requirement for today's technology. This fault diagnosis system should not be a black box; condition monitoring and comprehensive diagnosis results should be made available to engineering consulting services. It should be able to assist engineers in accumulating knowledge for reconfiguration activities (including diagnosis regulations) and improving the creation of innovative aircraft.

In the context of this research, the faults identification and repair algorithm is entirely accurate. After recognizing the fault pattern, the algorithm automatically compensates for the signal that coincides with the original signal form of the inductor working well. Based on the proposed method, it is possible to

build an automatic fault identification device and repair some faults on the aircraft to ensure the system's safety in all working conditions. The proposed algorithm is only suitable for some typical fault types, not considering random factors, noise, calculation speed, and other sensor faults. However, the algorithm needs improvement to speed up the computation to meet the shortest and most efficient time. The actual implementation of the algorithm can use the FPGA platform. The author will overcome the study's limitations in future investigations. Further studies will extend to other sensors in aircraft and use a more intelligent identification method.

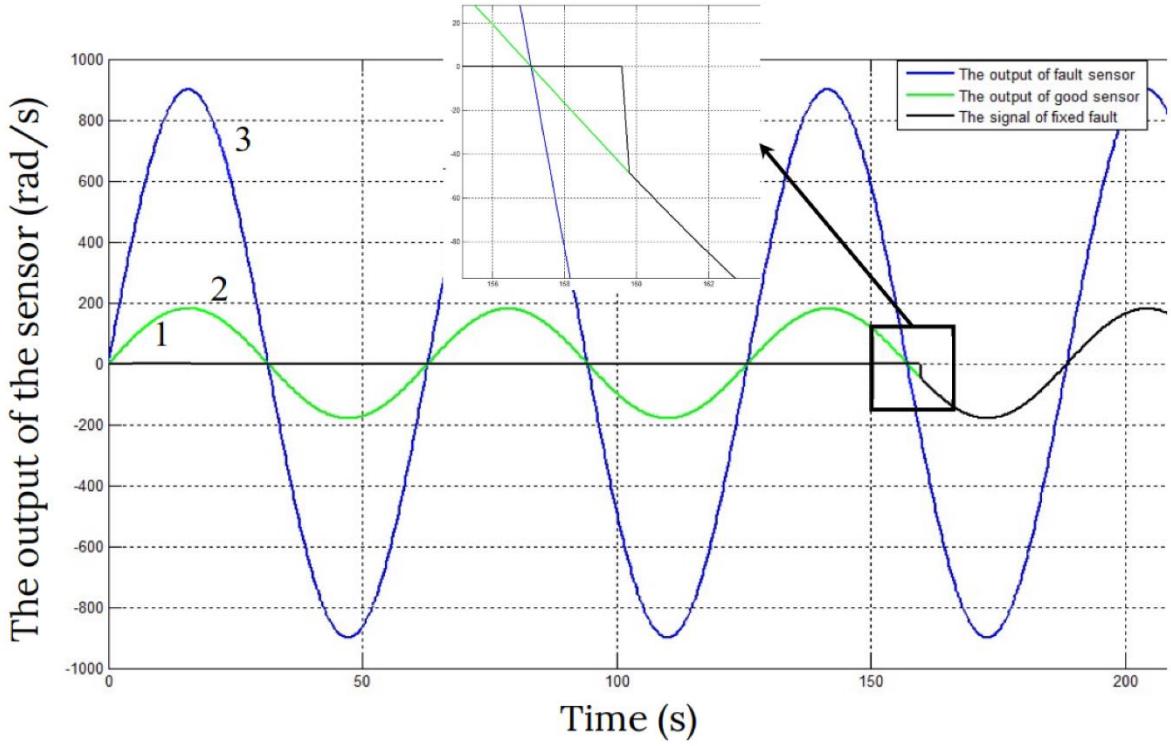

Fig 18. Simulation results of automatic repair of fault s for damage caused by signal gain changes

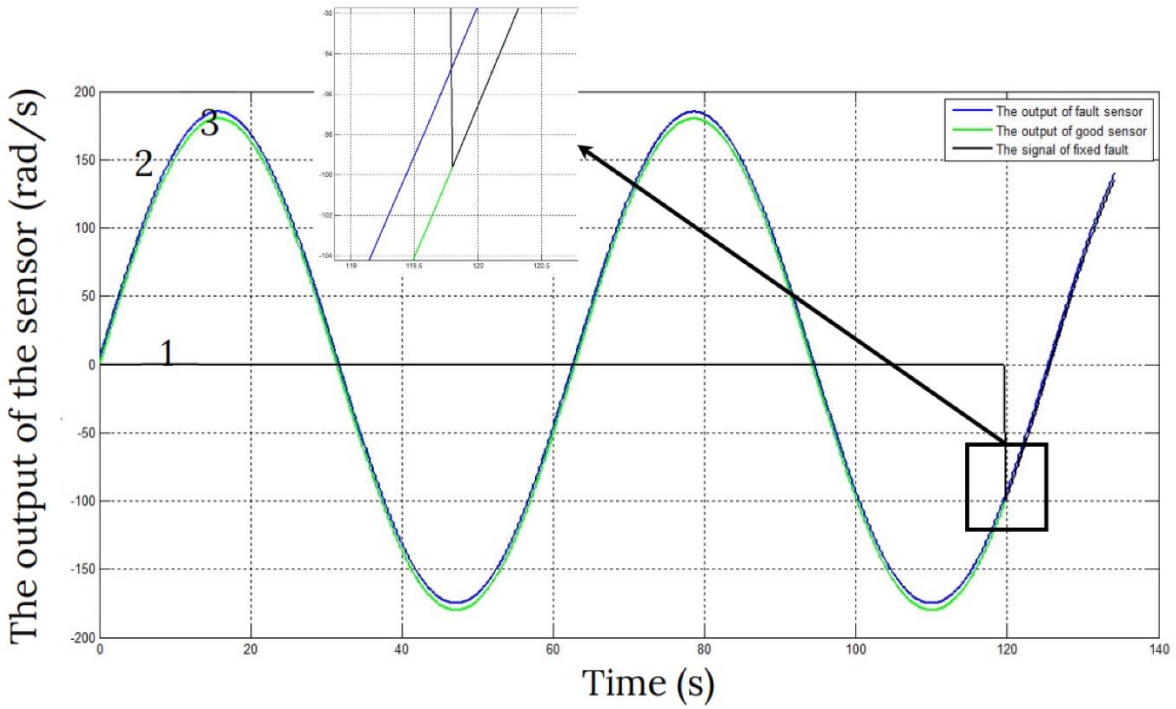

Fig 19. Simulation results of automatic repair of fault s for drift fault

Abbreviations

AV : Aerial Vehicles
UAV : Unmanned Aerial Vehicle
FDD : Fault Detection and Diagnosis

References

Arockiam, N.J., Jawaid, M. and Saba, N. (2018) 'Sustainable bio composites for aircraft components', in Jawaid, M. and Thariq, M.B.T.-S.C. for AA (eds) *Woodhead Publishing Series in Composites Science and Engineering*. Woodhead Publishing, pp. 109–123. doi:10.1016/B978-0-08-102131-6.00006-2.

Baskaya, E., Bronz, M. and Delahaye, D. (2017) 'Fault detection & diagnosis for small UAVs via machine learning', *AIAA/IEEE Digital Avionics Systems Conference - Proceedings*, 2017-Septe. doi:10.1109/DASC.2017.8102037.

Brooks, S. and Roy, R. (2021) 'An overview of self-engineering systems', *https://doi.org/10.1080/09544828.2021.1914323*, 32(8), pp. 397–447. doi:10.1080/09544828.2021.1914323.

Cardei, M. and Du, D.Z. (2005) 'Improving Wireless Sensor Network Lifetime through Power Aware Organization', *Wireless Networks 2005 11:3*, 11(3), pp. 333–340. doi:10.1007/S11276-005-6615-6.

Chen, W. Bin *et al.* (2009) 'Knowledge base design for fault diagnosis expert system based on production rule', *Proceedings - 2009 Asia-Pacific Conference on Information Processing, APCIP 2009*, 1, pp. 117–119. doi:10.1109/APCIP.2009.38.

CHU, L. *et al.* (2022) 'Design, modeling, and control of morphing aircraft: A review', *Chinese Journal of Aeronautics*, 35(5), pp. 220–246. doi:10.1016/J.CJA.2021.09.013.

Hajiyev, C. and Caliskan, F. (2000) 'Sensor/actuator fault diagnosis based on statistical analysis of innovation sequence and Robust Kalman Filtering', *Aerospace Science and Technology*, 4(6), pp. 415–422. doi:10.1016/S1270-9638(00)00143-7.

Hajiyev, C. and Caliskan, F. (2005) 'Sensor and control surface/actuator failure detection and isolation applied to F-16 flight dynamic', *Aircraft Engineering and Aerospace Technology*, 77(2), pp. 152–160. doi:10.1108/00022660510585992/FULL/PDF.

Hajiyev, C. and Soken, HE (2013) 'Robust Adaptive Kalman Filter for estimation of UAV dynamics in the presence of sensor/actuator faults', *Aerospace Science and Technology*, 28(1), pp. 376–383. doi:10.1016/j.ast.2012.12.003.

He, Q. *et al.* (2020) 'Performance comparison of representative model-based fault reconstruction algorithms for aircraft sensor fault detection and diagnosis', *Aerospace Science and Technology*, 98, p. 105649. doi:10.1016/j.ast.2019.105649.

Iemma, U., Pisi Vitagliano, F. and Centracchio, F. (2018) 'A multi-objective design optimisation of eco-friendly aircraft: the impact of noise fees on airplanes sustainable development', *International Journal of Sustainable Engineering*, 11(2), pp. 122–134. doi:10.1080/19397038.2017.1420109.

Isermann, R. (2005) *Fault-diagnosis systems: an introduction from fault detection to fault tolerance*. Springer Science & Business Media.

Khamis, A. (2021) 'Smart Mobility', *Smart Mobility* [Preprint]. doi:10.1007/978-1-4842-7101-8.

Kim, S., Choi, J. and Kim, Y. (2008) 'Fault detection and diagnosis of aircraft actuators using fuzzy-tuning IMM filter', *IEEE Transactions on Aerospace and Electronic Systems*, 44(3), pp. 940–952. doi:10.1109/TAES.2008.4655354.

Lu, P *et al.* (2015) 'Adaptive Three-Step Kalman Filter for Air Data Sensor Fault Detection and Diagnosis', *Journal of Guidance, Control, and Dynamics*, 39(3), pp. 590–604. doi:10.2514/1.G001313.

Lu, Peng *et al.* (2015) 'Double-model adaptive fault detection and diagnosis applied to real flight data', *Control Engineering Practice*, 36, pp. 39–57. doi:10.1016/j.conengprac.2014.12.007.

rhan, İ., Kapanoğlu, M. and Karakoç, T. (2011) 'Concurrent aircraft routing and maintenance scheduling ', *JOURNAL OF AERONAUTICS AND SPACE TECHNOLOGIES*, 5(1), pp. 73–79.

Sullivan, G.F. (1988) 'A O(t3+ |E|) Fault Identification Algorithm for Diagnosable Systems', *IEEE Transactions on Computers*, 37(4), pp. 388–397. doi:10.1109/12.2182.

Tran, H.S. *et al.* (2021) 'Developing An Approach For Fault Detection And Diagnosis Of Angular Velocity Sensors', *International Journal of Aviation Science and Technology*, 2(1), pp. 15–21. doi:10.23890/IJAST.vm02is01.0102.

Tuan, Q.D., Firsov, S.N. and Pishchukhina, O.. (2012) 'Design a fault diagnose block of angular velocity sensors for control systems of a multipurpose aircraft', *Science and Technology of the Air Force of Ukraine*, 2(11), pp. 84–88.

Vieira, D.R. and Bravo, A. (2016) 'Life cycle carbon emissions assessment using an eco-demonstrator

aircraft: the case of an ecological wing design', *Journal of Cleaner Production*, 124, pp. 246–257. doi:10.1016/j.jclepro.2016.02.089.

Wang, Z., Zarader, J.. and Argentieri, S. (2012) 'Aircraft fault diagnosis and decision system based on improved artificial neural networks', in *IEEE/ASME International Conference on Advanced Intelligent Mechatronics* (AIM). IEEE, pp. 1123–1128.

Xue, W., Guo, Y.Q. and Zhang, X.D. (2007) 'A bank of kalman filters and a Robust Kalman filter applied in fault diagnosis of aircraft engine sensor/actuator', *Second International Conference on Innovative Computing, Information and Control, ICICIC* 2007 [Preprint]. doi:10.1109/ICICIC.2007.3.

Yang, T. (2021) 'Aviation Sensors and Their Calibration', *Telemetry Theory and Methods in Flight Test*, pp. 81–149. doi:10.1007/978-981-33-4737-3_3.